学位請求論文

Tunneling phenomena and their terahertz dynamics in semiconductor superlattices

半導体超格子中のトンネリング現象とその
テラヘルツダイナミクスに関する研究

March 25, 2005

Yozo Shimada

Preface

This thesis presents a part of the research carried out at the Institute of Industrial Science (IIS), the University of Tokyo. Professor Kazuhiko Hirakawa has supervised this research while the author was a technical assistant of IIS from February 1993 through March 2002.

In this thesis, a study on the tunneling phenomena and their terahertz photocurrent dynamics in semiconductor superlattices was described.

September 2004

Yozo Shimada

Acknowledgement

Table of Contents

Chapter I

Introduction

1.1 Semiconductor superlattices

Semiconductor superlattices (SLs) consist of a periodic sequence of alternately grown thin layers of two different semiconductor materials. As such, they belong to the conceptually simplest artificial semiconductor structures made possible through the progress in epitaxial crystal growth techniques over the past three decades. Despite their simplicity when compared with other multilayer structures, they represent a microscopic solid state physics laboratory, offering a wealth of fundamental phenomena to be investigated. Since the periodicity (or another quantity) of the SL can be intentionally varied over a wide range while leaving the other parameters unchanged, a systematic exploration of electrons in a periodic potential becomes possible. For instance, the miniband width along the growth direction can be adjusted between an exponentially small value (<< 1 meV) and a few hundred meV, thus spanning the range of an effectively two-dimensional system to a strongly or weakly anisotropic three-dimensional medium. Since this comprises the energy scale of thermal or magnetic energies, some unique properties of band electrons can be studied which are not easily accessible in natural crystals. Therefore, semiconductor SLs can serve as a model system for quantum mechanics and solid state physics.

Semiconductor SLs were first proposed by Esaki and Tsu in 1970 [1], who predicted negative differential conductivity due to acceleration of the electrons into the negative-mass region of a SL miniband. The potential of SLs for the study of fundamental physics as well as for applications in novel devices was soon recognized. The first experimental realization of SLs followed shortly along with a number of optical [2] and transport [3,4] experiments. During the following decade only a relatively small number of investigations on SLs were

reported, but starting in the mid 1980s, apparently as a consequence of significantly improved material quality, larger and larger numbers of publications have appeared. Coherent miniband transport perpendicular to the layers has been demonstrated by various methods [5-8]. Among the most striking phenomena experimentally discovered recently are the Wannier-Stark ladder (WSL) [9,10] and Bloch oscillations (BO) [11-13], which had both been a controversial subject among solid state physicists. Very recently, a unipolar laser based on intersubband transitions has been fabricated [14].

1.2 Transport and optical properties of superlattices

1.2.1 Band structure of semiconductor superlattices

By the alternating growth of thin semiconductor layers with smaller and larger band gap, it is possible to design new forms of one-dimensional crystals with properties which are wealth of fundamental phenomena to be investigated by suitable adjustment of the period and the band gap difference; the band width of the artificially created band in the growth direction (the so-called miniband) can in principle be adjusted between zero and a few hundred meV. Figure 1.1 scheme shows a schematic picture of a semiconductor superlattice with the electron minibands. Note that we display here the special case of a type I superlattice, where the bands of the material with smaller band gap are located (in energy) between the bands of the material with larger band gap.

The electronic states in semiconductor SLs are usually calculated using the envelope function approach. The width of the minibands in semiconductor superlattices can be controlled over a large energy range by choosing appropriate materials systems and layer thickness. The large majority of experiments in superlattices have used the $GaAs/Al_xGa_{1-x}As$ heterosystem due to the superior quality of the samples. If the material is kept direct in the barrier (i.e. the aluminum content of the barriers is kept below about $x = 0.4$),
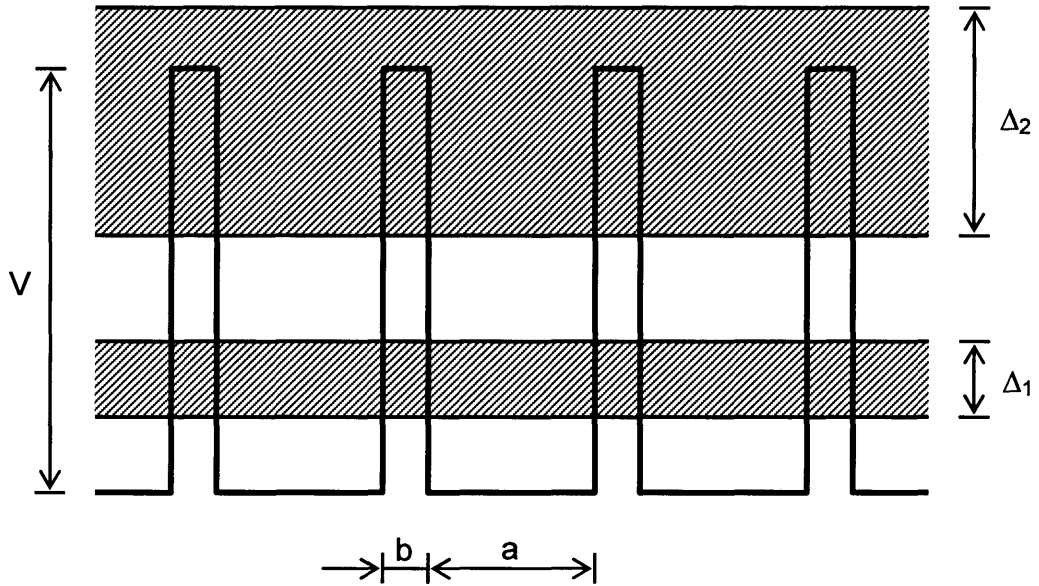
Fig. 1.1   Miniband structure of a superlattice in real space. Δ_n is the width of the nth miniband ($n \geq 1$).   The widths of quantum wells and barriers are a and b, respectively.

the available total band offset is about 0.5 eV. Assuming a 2/3 to 1/3 ratio of the band offsets for the conduction and the valence band, the maximum offset of the conduction band and thus the maximum width of the electron miniband is about 300 meV in this system.

1.2.2 Transport properties

If an electric field is applied to a superlattice along the perpendicular to the growth direction, the minibands are split into a set of discrete, equidistant energy levels, which are localized around one period of the superlattice. This is the Wannier-Stark ladder, whose energy separation is given by eFd. Here F is the electric field and d is the period of the superlattice. The influence of an electric field along the superlattice axis can also be treated semiclassically by solving the classical equation of motion for an electron in the miniband. The electron performs an oscillatory movement in velocity and also in real space with the angular frequency $eFd/\hbar = \omega_B$, the Bloch frequency. These are the famous Bloch oscillations, whose existence has also been questioned for a long time. However, very recently they have been evidenced by measuring directly the THz radiation emitted by the oscillating charge at the Bloch frequency [13].

In fact, both phenomena, the Wannier-Stark ladder and Bloch oscillations, are merely different aspects of the same phenomenon, namely the electric field-induced localization of electrons in a periodic potential. As is obvious from the above formulae, the Bloch frequency corresponds exactly to the energy separation of Wannier-Stark states. Which of the two descriptions is more adequate depends on the parameter regime and the specific kind of experiment to be analyzed. A consequence of this localization is the negative differential velocity (or conductivity) of a superlattice, which was predicted in the original Esaki-Tsu paper as well as in more sophisticated numerical calculations and has been unambiguously observed recently.

As for the transport properties of weakly coupled superlattices (MQWs: multiple quantum wells), strikingly regular periodic negative differential resistance has been observed

4
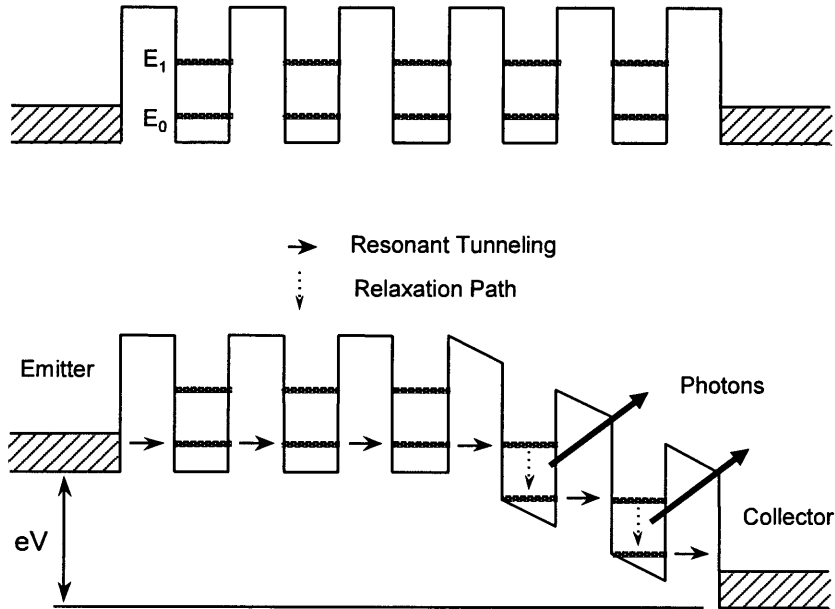
Fig. 1.2 Schematic illustration of band diagram of the multiple quantum well diode; (a) Zero bias, and (b) Sequential resonant tunneling occurs through E_0 in the low-field region and through the first excited state E_1 in the high-field region.
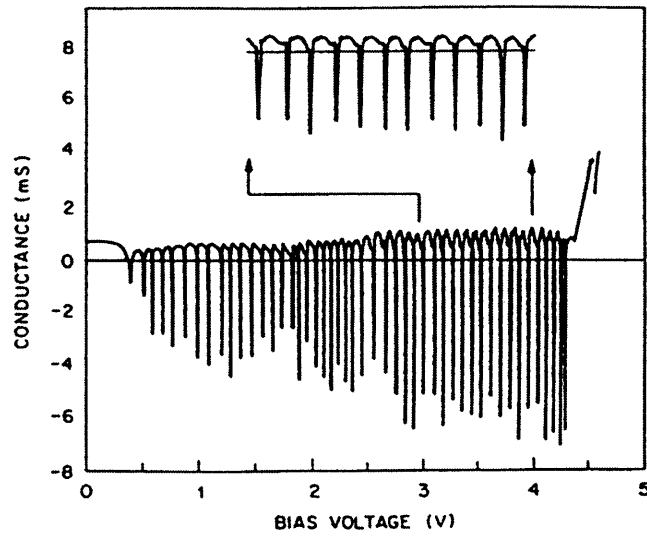
Fig. 1.3   Conductance vs applied voltage for a 49-period superlattice. The inset is a blowup of the 3-4 V range, showing a regular periodicity of the negative conductance peaks [15].
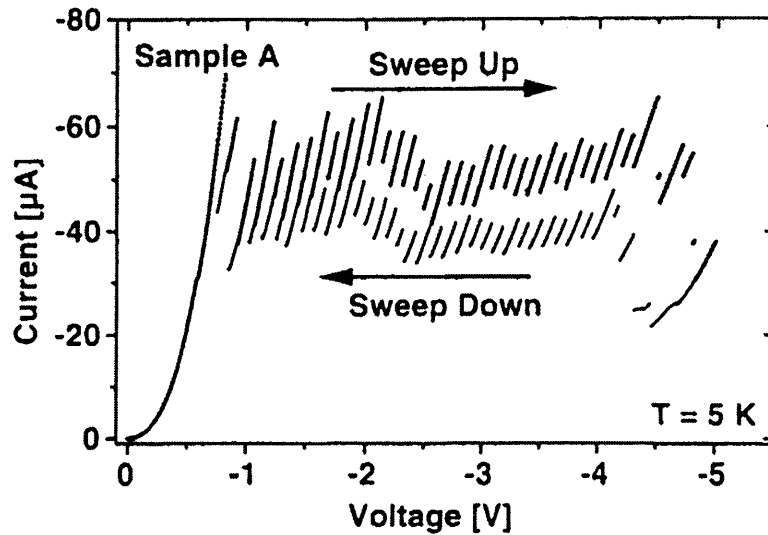
Fig. 1.4   Typical current-voltage characteristic at 5 K of a doped multiple quantum well structure that shows domain formation [16].

in n-doped GaAs/AlGaAs MQWs [15]. The quantum wells in the structures were designed in such a way that only two confined states. For a bias per well larger than the ground-state bandwidth, tunneling through the ground states is no longer possible and the structure breaks up into a low field region and a high field region where the electrons flow via sequential resonant tunneling from the localized ground state E_0 of one well into the localized excited state E_1 of the neighboring well (Fig. 1.2). They relax back to E_0 and tunnel into the next well. As the bias voltage is further increased the high field domain expands by one well at a time, thereby producing periodic negative resistance peaks with a period of ΔE nearly equal to $E_1 - E_0$ shown in Fig. 1.3.

The boundaries between different electric field domains are necessary connected with a 2D charge accumulation field. Due to the periodic modulation of the conduction band this charge layer can not move continuously through the superlattice as the bias voltage is increased. Instead, the layer resides in one well over a certain voltage range until, with increasing external bias, it spontaneously moves to the next well. This leads to sharp discontinuities and a hysteresis in the I-V characteristic, which is connected with a multistability of the current (Fig. 1.4) [16].

In a doped SL with an externally applied bias voltage, the effects of self-organization can result in the formation of electric-field domains. Under this condition, the applied electric field breaks up into two distinct domains separated by a space-charge layer, the domain boundary. Very recently, it was found that electric field domains in SLs can be unstable with an oscillating domain boundary, which moves over several periods. The motion of the domain boundary results in spontaneous self-oscillations of the current with frequency ranging from kHz to GHz. Therefore, semiconductor superlattices with an oscillating domain boundary may have important potential applications for microwave devices. [17-20].

1.2.3 Optical properties

The problem of generating and amplifying infrared light in the semiconductor SLs was theoretically addressed by Kazarinov and Suris [21]. There they suggested that photon-assisted tunneling could lead to gain or infrared emission.

The absorption and emission of semiconductor SLs with and without electric bias field have been studied in detail. A comprehensive review has recently been given by Helm [22]. A number of experiments have been performed in the regime where the bias fields are zero or low enough that the miniband is preserved (i.e. the field localization length is larger than the coherence length). The absorption experiments have shown both the characteristic features of inter-miniband and intra-miniband absorption.

Emission studies from biased superlattices have recently brought exciting result [13,14]. The first experiment which has shown spontaneous emission due to intraband emission was reported by Helm et al [23]. The intensity of this radiation was quite low. Very recently, far-infrared experiments which address the intra-miniband properties when the WSL is present have been performed.

A field which has been recently investigated in detail is the influence of THz radiation (in the far-infrared (FIR)) on the transport in superlattice. It was shown that *I-V* curve of the SLs is strongly changed when FIR is focused onto the sample. The observed effects were explained by a theoretical model based on nonlinear transport in SL. The main parameter which can be deduced from the observed effects is the scattering time of the electrons. This time is in principle identical to what is measured as intersubband dephasing in the optical experiments. It is an interesting future task to check the similarities and differences in the damping behavior of the far-infrared and interband optical experiments.

Recently, the inverse Bloch oscillator was observed. In this experiment, the current through the superlattice showed resonance when the frequency of the radiation was tuned through multiples of the BO frequency [13]. THz emission due to Bloch oscillations have been also observed at room temperature [24].

1.3 Device applications

In recent years, SLs have found many applications in optoelectronic devices such as quantum cascade lasers, Bloch oscillators, quantum well infrared photodetectors, and so on.

1.3.1 Quantum cascade laser

Since an invention by Faist et al. in 1994, quantum cascade lasers have been constantly innovated as coherent sources in the THz range of the electro-magnetic waves [14]. The quantum cascade lasers are unipolar semiconductor structures in which electrons are fed sequentially from an injector region into the active region such as coupled quantum wells or superlattices.

The quantum cascade laser scheme (Fig. 1.5A) makes use of the discrete electronic states arising from quantum confinement, normal to the layers, in nano scale semiconductor heterostructures. Parallel to the layers, these states have plane wave-like energy dispersion. The corresponding energy subbands are nearly parallel because of the small nonparabolicities for wave numbers k not too far from the bottom and for transition energies that are not too large (Fig. 1.5B). As a result, electrons making radiative transitions to a lower subband will all emit photons of essentially the same frequency ν with energy $\hbar\nu = E_3 - E_2$ (Fig. 1.5B), where $\hbar$ is Planck's constant. If a population inversion is then created between these excited states, the gain spectrum will be correspondingly narrow (Fig. 1.6).

Research in this field is continuously expanding: new material systems are being explored, ultrahigh-speed operation and mode locking have been demonstrated, and new spectral ranges are under investigation. The demonstration of a semiconductor injection laser at very long wavelengths would be of great importance due to the present lack of convenient and compact THz sources [25-27].

9
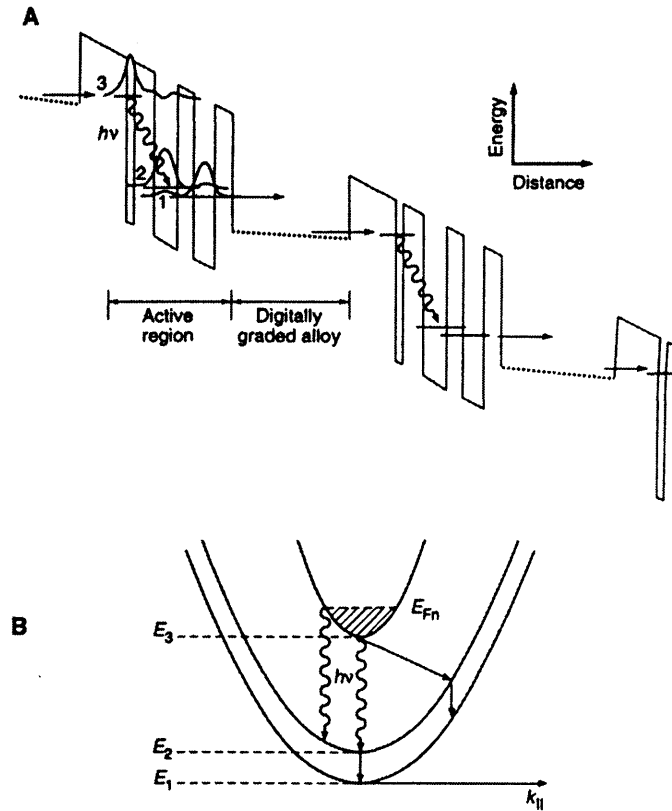
Fig. 1.5 (A) Conduction band energy diagram of a portion of the 25-period section of the quantum cascade laser. The dashed lines are the effective conduction band edges of the digitally graded electron-injecting regions. The wavy arrow indicates the laser transition. (B) Schematic representation of the dispersion of the $n = 1, 2$, and 3 states parallel to the layers; $k_{\parallel}$ is the corresponding wave number. The wavy arrows indicate that all radiative transitions originating from the electron population (shown as shaded) in the $n = 3$ state have essentially the same wavelength [25].
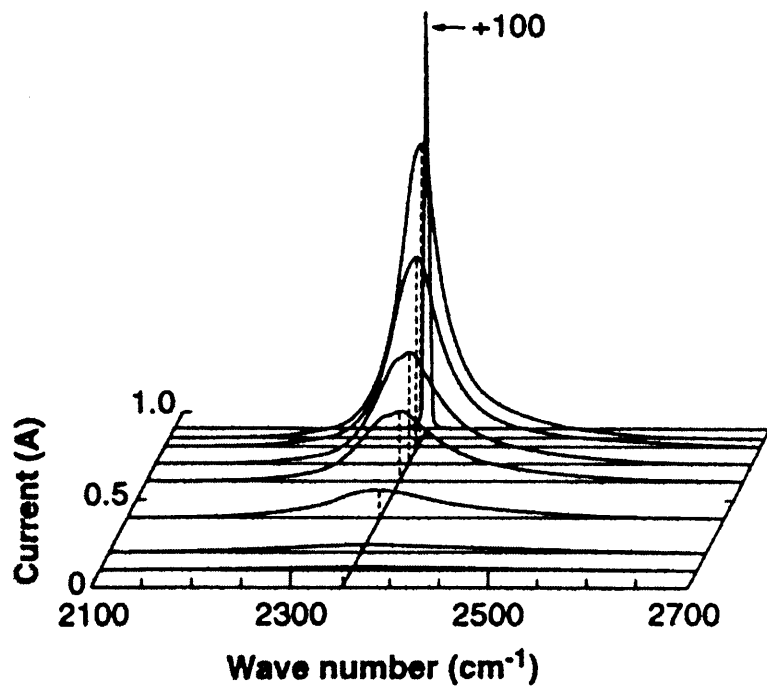
Fig. 1.6 Emission spectrum of the laser at various drive current. The strong line narrowing and large increase of the optical power demonstrates laser action. The spontaneous emission and the laser radiation are polarized normal to the layers [25].

1.3.2 Bloch oscillators

Miniband electron transport in semiconductor superlattices is an important subject of experimental and theoretical investigations, which was initiated by the pioneering paper of Esaki and Tsu [1]. If a static electron field E_s is applied along the superlattice axis, electrons begin to move in accordance with the semiclassical Newton's law (neglecting scattering). If the energy gap $\Delta\Gamma_g$ between first and the second miniband is large enough, and the scattering rate is small, then electrons oscillate inside the first miniband at so-called Bloch frequency. The quasiparticle energy and the quasiparticle group velocity along the superlattice axes are periodic function of time.

Since in semiconductor superlattices the Bloch frequency can be varied by the electric field up to $1 - 10$ THz, it is a great challenge to make a tunable Bloch oscillator in the THz frequency range [1,28,29]. Even after three decades from the proposal, however, THz devices using Bloch oscillations have not been achieved yet. It is, therefore, of prime importance to establish an understanding of the dynamical electron motion in the THz regime. In recent years, a new technique that measures the THz electromagnetic wave emitted by ultrafast transient electron motions has been established (time-resolved THz emission spectroscopy). This new technique makes it possible to observe ultrafast motion of electrons in superlattices and discuss Bloch oscillations in superlattices. In recent study, the inverse Bloch oscillation was observed (Fig. 1.7). Furthermore, a strong experimental support for THz gain up to a few THz due to Bloch oscillating electrons was presented experimentally [30].

1.3.3 Quantum well infrared photodetectors

Detections of long-wavelength infrared radiation $1 \sim 10$ μm require a small band gap $E_g \sim 0.1$ eV. Such small-band-gap materials are known to be more difficult to grow, process, and fabricate into devices than are wider-band gap semiconductor. These difficulties thus
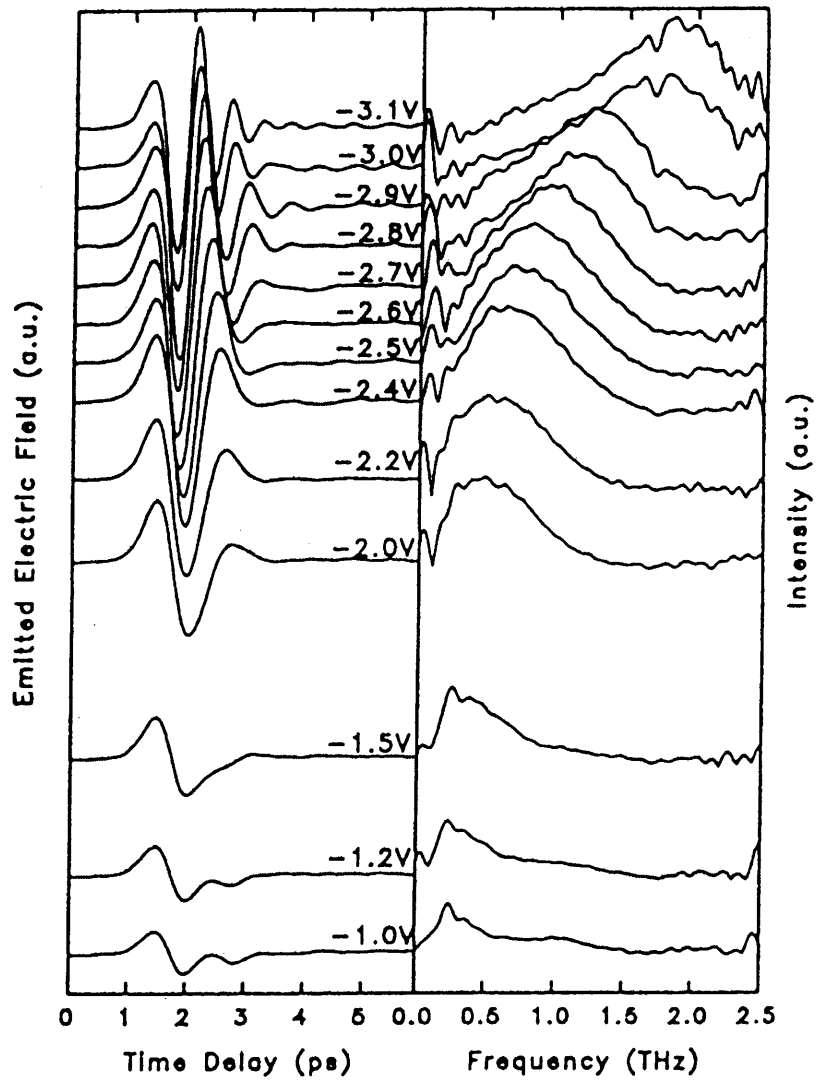
Fig. 1.7 Left side: Measured coherent electromagnetic radiation emitted from a superlattice for different reverse-bias voltages. Right side: Fourier transforms of the time-domain data. The peak of the Fourier spectra show the THz emission due to Bloch oscillations [13].

motivated the study of novel artificial small effective band-gap (E_g < 1 eV) semiconductors. In order to employ these desirable large gap materials for long-wavelength optical devices, it is advantageous to use intersubband absorption involving transitions within the same band, rather than the usual interband absorption mechanism (involving transitions between the conduction and valence bands). In order to create these states within the conduction or valence band, quantum wells are used. It is important to note, however, that unlike the usual interband transition, these quantum wells must be doped since $hv < E_g$ and thus the photon energy is not sufficient to create photocarriers. The infrared-absorption mechanism is, therefore, an excitation of an electron from the doped quantum well ground state in the conduction band to an unoccupied excited state in the same band. In the quantum well infrared photodetectors (QWIPs), the quantum well structure is designed so that this excited carrier can escape from the well and be collected as photocurrent.

The first QWIP was demonstrated by Levine et al. [31], and fabricated by using quantum wells containing two bound states. The infrared absorption due to the intersubband transition from the ground state to the excited state is followed by the photoexcited electrons tunneling out of the well, as shown in Fig. 1.8. These photocarriers, which escape from the well, drift by the electric field in the continuum above the barriers for an excited-state life time, τ_L, during which they travel a distance L and thereby produce a photo current [32].

1.4 Objectives

For device applications of superlattices, it is essential to establish a good understanding of the mechanism of transport and optical dynamics in such structures. In addition to this, the field-induced tunneling dynamics of carriers also needs to be evaluated accurately. The aim of this study is to understand 'carrier dynamics of tunneling properties' of superlattice and multiple quantum wells, and to show how THz emission spectroscopy can reveal some of the unique properties of the miniband structure and their aspects of the coherent electron
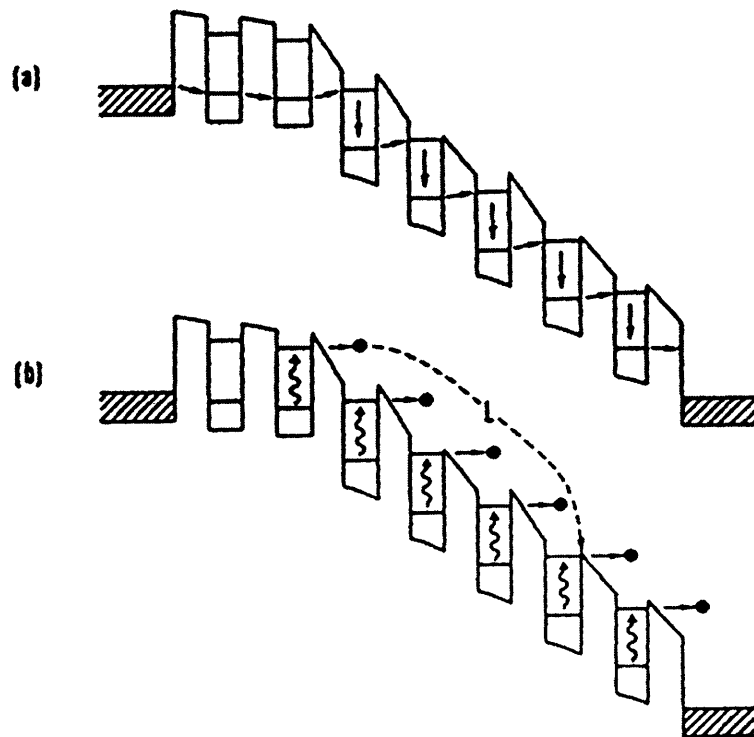
Fig. 1.8 Sequential resonant tunneling in high-field domain (right-hand side); tunneling through ground state (left-hand side). (b) Photo-conductivity produced by absorption of intersubband radiation followed by tunneling out of well [32].

motion.

In order to clarify tunneling phenomena and formation of quantized states in multiple quantum wells, we fabricated $GaAs/Al_{0.3}Ga_{0.7}As$ semiconductor multiple quantum well structures and investigate electron transport properties. Periodic negative differential resistances due to sequential resonant tunneling and a formation of high field domains are studied in detail. Furthermore, a sequential resonant magneto-tunneling through Landau levels are shown by a characterization of tunneling current under high magnetic fields. Dynamics of a high field domain formation are also discussed by analyzing temporal transport properties in multiple quantum wells using step and sweep bias fields.

Furthermore, it is of prime importance to understand a dynamical electron motion in the THz regime in order to realize ultra-fast devices based on superlattices. For this purpose, a time-resolved THz emission spectroscopy is established to investigate a dynamical electron motion in superlattices. We fabricate (metal)-(intrinsic)-(n-type) $GaAs/Al_{0.3}Ga_{0.7}As$ superlattice structures suited for THz emission measurements. Photo absorption properties are investigated by photocurrent spectra using a Fourier transform spectroscopy, verifying a formation of minibands and Wannier-Stark ladders. THz emission from the superlattices reflects a dynamical electron transport in minibands, involving the Bloch oscillations. The THz emission due to Bloch oscillations are observed even at room temperature. Furthermore, we show a strong experimental support for the THz gain due to Bloch oscillating electrons in wide miniband $GaAs/Al_{0.3}Ga_{0.7}As$ SLs. Quasi-periodic structures observed in the emitted THz intensity-vs-bias field curve are identified to be due to the resonant Zener tunneling between the Wannier-Stark (WS) ladders associated with the ground and the excited minibands.

Single quantum well infrared photodetector structures are particularly interesting since their simple band structures allow accurate calculation of the bias voltage dependence of the potential profiles of each of two barriers, photo-induced band bending effects in the contacts, as well as charge accumulation in the quantum well. In order to investigate the

photoresponse of the single quantum well infrared photodetectors, we fabricated GaAs/Al$_{0.3}$Ga$_{0.7}$As single quantum well structures grown by molecular beam epitaxy. Steady state photoresponses of single quantum well infrared photodetectors are investigated by a Fourier transform infrared spectroscopy. Furthermore, band bending effect due to a charge accumulation is shown by analysis of a dynamics of photo-induced carriers in single quantum well infrared photodetectors using a free electron laser beam, which has a wide tunability of the lasing wavelength and a short optical pulse. Numerical consideration of the SQWIP strongly supported the band bending effect due to photo-induced carriers and the involved large photosensitivity.

1.5 Synopses of chapters

This thesis is organized as follows. Chapter II discusses a tunneling transport in weakly coupled superlattices. Sequential resonant tunneling with high-field domain formation leading to a hysteresis in the *I-V* characteristics (section 2.2) and supply function dependent current-voltage characteristics (section 2.3) will be discussed. Sequential resonant magnetotunneling through Landau levels under high magnetic fields is presented in section 2.4. Section 2.5 deals with the dynamics of high-field domain formation in the mulitple quantum wells.

Chapter III is devoted to a discussion of terahertz emission due to miniband transport in superlattices investigated by using time-resolved terahertz emission spectroscopy. After an introduction of Bloch oscillation in semiconductor superlattices (section 3.2) and an experimental setup for time-resolved THz emission spectroscopy (section 3.3), THz emission due to miniband transport investigated by using the THz spectroscopy at room temperature is described in section 3.4. Next, THz conductivity and possible Bloch gain (section 3.5) and inter-miniband resonant Zener tunneling (section 3.6) are shown.

Chapter IV deals with single quantum well infrared photodetector structures for steady

state characteristics (section 4.2). A carrier dynamics of single quantum well infrared photodetector structures investigated by using a free electron laser is presented in both experimental (section 4.3) and theoretical analysis (section 4.4).

Finally, we briefly conclude this thesis in chapter V.

Bibliography

[1]   L. Esaki and R. Tsu, IBM J. Res. Dev. **14**, 61 (1970).

[2]   R. Dingle, A. C. Gossard and W. Wiegmann, Phys. Rev. Lett. **34**, 1327 (1975).

[3]   R. Tsu, L. L. Chang, G. A. Sai-Halasz, and L. Esaki, Phys. Rev. Lett. **34**, 1509 (1975).

[4]   L. Esaki and L. L. Chang, Phys. Rev. Lett. **33**, 495 (1974).

[5]   J. F. Palmier, C. Minot, J. L. Lievin, F. Alexandre, J. C. Harmand, J. Dangla, C. Durbon-Chevallier, and D. Ankri, Appl. Phys. Lett. **49**, 1260 (1986).

[6]   C. Minot, H. LePerson, F. Alexandre, and J. F. Palmier, Appl. Phys. Lett. **51**, 1626 (1987).

[7]   B. Deveaud, J. Shah, T. C. Damen, B. Lambert, and A. Regreny, Phys. Rev. Lett. **58**, 2582 (1987).

[8]   P. England, J. R. Hayes, and M. Helm, Phys. Rev. Lett. **63**, 1708 (1989).

[9]   E. E. Mendez, F. Agullo-Rueda, and J. M. Hong. Phys. Rev. Lett. **60**, 2426 (1988).

[10] P. Voisin, J. Bleuse, C. Bouche, S. Gaillard, C. Alibert, and A. Regreny, Phys. Rev. Lett. **61**, 1639 (1988).

[11] K. Leo, P. Haring Boliver, F. Brüggemann, S. Schwedler, and K. Köhler, Solid State Commun. **84**, 943 (1992).

[12] J. Feldmann et al., Phys. Rev. B **46**, 7252 (1992).

[13] C. Waschke, H. G. Roskos, R. Schwedler, L. Leo, H. Kurz, and K. Köhler, Phys. Rev. Lett. **70**, 3319 (1993).

[14] J. Faist, F. Capasso, D. J. Sivco, C. Sirtori, A. L. Hutchinson, and A. Y. Cho, Science **264**, 553 (1994).

[15] K. K. Choi, B. F. Levine, R. J. Malik, J. Walker, and C. G. Bethea, Phys. Rev. B **35**, 4172 (1987).

[16] J. Kastrup, H. T. Grhan, K. Ploog, F. Prengel, A. Wacker, and E. Schöll, Appl. Phys. Lett. **65**, 1808 (1994).

[17] H. T. Grahn, J. Kastrup, K. Ploog, L. L. Bonilla, J.Galán, M. Kindelan, and M. Moscoso,

Jpn. J. Appl. Phys. **34**, 4526 (1995).

[18] J. Kastrup, R. Klann, H. T. Grhan, K. Ploog, L. L. Bonilla, J. Galán, M. Kindelan, M. Moscoso, and R. Merlin, Phys. Rev. B **52**, 13761 (1995).

[19] A. Wacker, F. Prengel, and E. Schöll, in Proceedings of the 22nd International Conference on the Physics of Semiconductors, (1995).

[20] Y. Zhang, R. Klann, K. H. Ploog, and H. T. Grahn, Appl. Phys. Lett. **69**, 1116 (1996).

[21] R. F. Kazarinov and R. A. Suris, "Possibility of amplification of electromagnetic waves in a semiconductor with a superlattice", Sov. Phys. Semicond. **5**, 707 (1971).

[22] M. Helm, Semicond. Sci. Technol. **10**, 557 (1995).

[23] M. Helm, P. England, E. Colas, F. DeRosa, and S. J. Allen, Jr., Phys. Rev. Lett. **63**, 74 (1989).

[24] Y. Shimada, K. Hirakawa and S.-W. Lee, Appl. Phys. Lett. **81**, 1642 (2002).

[25] J. Faist, F. Capasso, C. Sirtori, D. Sivco, A. L. Hutchinson, S.-N. G. Chu, and A. Y. Cho, Appl. Phys. Lett. **65**, 2901 (1994).

[26] B. S. Williams, H. Callebaut, S. Kumar, Q. Hu, and J. Reno, Appl. Phys. Lett. **82**, 1015 (2003).

[27] R. Köhler, A. Tredicucci, F. Beltram, H. E. Beere, E. H. Linfield, A. G. Davies, D. A. Ritchie, S. S. Dhillon, and C Sirtori, Phys. Rev. Lett. **82**, 1518 (2003).

[28] D. A. Ryndyk, N. V. Demarina, J. Keller, and E. Schomburg, Phys. Rev. B **67**, 033305 (2003).

[29] H. Willenberg, G. H. Döhler, and J. Faist, cond-mat, 0205359 (2002).

[30] Y. Shimada, K. Hirakawa, M. Odnoblioudov, and K. A. Chao, Phys. Rev. Lett. **90**, 046806 (2002).

[31] B. F. Levine, C. G. Bethea, G. Hasnain, J. Walker, and R. J. Malik, Appl. Phys. Lett. **53**, 296 (1988).

[32] B. F. Levine, J. Appl. Phys. **74**, R1 (1993).

Chapter II
Sequential tunneling transport in weakly coupled superlattices

2.1 Introduction

Semiconductor superlattices and their transport properties were first investigated by Esaki and Tsu in 1970 [1]. They predicted negative conductance associated with electron transfer into the negative mass regions of the miniband and Bloch oscillations. In 1971, Kazarinov and Suris theoretically studied the current-voltage (I-V) characteristics of multiple quantum well (MQW) structures with weak coupling between wells and predicted the existence of peaks corresponding to resonant tunneling (RT) between the ground and excited states of adjacent wells [2]. Calculations of RT through multiple barriers were also presented by Tsu and Esaki [3]. In 1974, Esaki and Chang observed periodic negative differential resistances (NDRs) along the superlattice axis in an AlAs/GaAs mulitilayer unipolar structure [4]. The voltage period of the NDRs was nearly equal to the energy separation between the first two conduction minibands. This effect was interpreted in terms of resonant tunneling between adjacent quantum wells occurring within an expanding high-field domain. The following year, Dohler and Tsu [5,6] predicted the existence of a new type of negative differential resistance (NDR) in a superlattice which occurs when the potential drop across the superlattice period exceeds the miniband width and the transport mechanism accordingly changes from miniband conduction to phonon-assisted tunneling. Preliminary experimental evidence of this effect was reported shortly after by Tsu *et al.* [7]. Tunneling injection of minority carriers into the resonance of a quantum well and a superlattice were subsequently observed by Rezek *et al.* [8] and by Vojak *et al.* [9], respectively.

In recent years, there has been a revival of interest in perpendicular quantum

transport in superlattices, in large part motivated by the impressive progress achieved in molecular beam epitaxy. Low interface states density can now be routinely achieved as demonstrated by high-quality modulation-doped hetero structures exhibiting high mobility. Due to improved growth and detection methods a number of features have only be resolved in recent years.

Many studies have established that the *I-V* characteristics of highly doped or optically excited samples consist of a sequence of branches whose number is approximately equal to the number of periods of the MQW. These branches may overlap, leading to multistability and hysteresis in the *I-V* characteristics. For weakly coupling MQWs, time-dependent features such as transient and persistent oscillations of the current have been observed.

In this chapter, we discuss our work in the area of perpendicular transport in MQW. In the second section, we discuss the sequential resonant tunneling with high-field domain formation leading to a hysteresis in the *I-V* characteristics, which is connected with a multistability of the current. In the third section, carrier density dependent sequential resonant tunneling effects are analyzed, along with a discussion of a supply function. Sequential resonant magnetotunneling through Landau levels under high magnetic fields is presented in the fourth section. The fifth Section deals with the dynamics of high-field domain formation in the mulitple quantum wells.

2.2 Sequential resonant tunneling in multiple quantum well structures

2.2.1 Resonant tunneling through quantum well structure

Resonant tunneling through a double barrier occurs when the energy of an incident electron in the emitter matches that of an unoccupied state in the quantum well corresponding to the same lateral momentum. NDR arises simply from momentum and energy conservation considerations and does not require the presence of a Fabry-Perot

effect.   This has been clarified by Luryi [10] and is illustrated Fig. 2.1.

Consider the Fermi sea of electrons in the degenerately doped emitter.   Assuming that the barriers are free of impurities and imhomogeneities, the lateral electron momentum (k_x, k_y) is conserved in tunneling.   This means that for $E_C < E_0 < E_F$ (where E_C is the bottom of the conduction band in the emitter and E_0 is the bottom of the subband in the QW), tunneling is possible only for electrons whose momenta lie in a disk corresponding to $k_z = k_0$ where $\hbar^2 k_0^2/2m^* = E_0 - E_C$.   Only those electrons have isoenergetic states in the QW with the same k_x and k_y.   This is a general feature of tunneling into a two-dimensional system of states.   As the emitter-base potential rises, the number of electrons can tunnel.   For $k_0 = 0$, the number of tunneling electrons per unit area equals $m^* E_F/\pi\hbar^2$.   When E_C rises above E_0, then at $T = 0$ temperature, there are no electrons in the emitter which can tunnel into the QW while conserving their lateral momentum. Therefore, one can expect an abrupt drop in the tunneling current.

2.2.2 Negative differential resistance due to scattering assisted tunneling

RT though a double barrier has been investigated experimentally by many researchers.   All of these investigations assumed that a Fabry-Perot type enhancement of the transmission was operational in such structures.   However, the observation of NDR does not imply a Fabry-Perot mechanism.   Other types of tests are necessary to show the presence of a resonant enhancement of transmission, such as the dependence of the peak current on the thickness of the exit barrier.

In principle, due to the two-dimensional (2D) nature of the electron gas in the well, resonant tunneling through multiple quantum wells is possible only when the energy levels in each well coincide, a condition generally not fulfilled in the presence of a field. However, Kazarinov and Suris [23] showed that in the presence of acoustic phonons and impurity scattering within each well, conservation of energy and momentum is relaxed and resonant tunneling is possible provide that $eV \ll \hbar/\tau_0$, where V is the potential difference
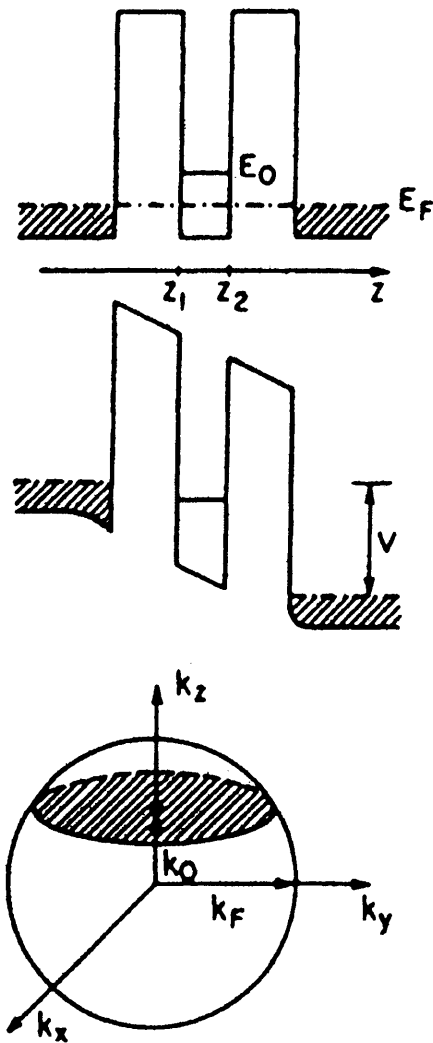
Fig. 2.1 Illustration of the operation of a double-barrier resonant tunneling diode. The top part shows the electron energy diagram in equilibrium. The middle displays the band diagram for an applied bias V when the energy of certain electrons in the emitter match unoccupied level of the lowest subband E_0 in the quantum well. The bottom illustrate the Fermi surface for a degenerately doped emitter.

between the adjacent wells and τ_0 is the ground-state scattering time. Therefore, at small bias, the electrons are able to conduct by ground-state resonant tunneling through the ground states of each well. A first negative-differential-resistance peak indicates the disruption of the resonant tunneling when $eV \ll \eta\, \hbar/\tau_0$, where η is a constant of order unity.

When the potential drop V across a period is larger than $\eta\, \hbar/\tau_0$, ground-state resonant tunneling is not possible and as a result negative differential resistance occurs. As each period breaks off from the resonant condition, the resistance across this period becomes much larger and a high-field domain forms. Any subsequent increase in the bias will appear across this domain until the ground level rises to $\eta\, \hbar/\tau_1$ of the first excited level (E_1) of the next well where upon the resonant tunneling condition is restored (Fig. 2.2(b)). Further increases in bias will cause another well to break off from the resonant condition and the I-V characteristics repeats. Due to the screening effect of the space-charge buildup at large bias, the domain formation is not a random process but occurs first at the anode and then extends one after the other towards the cathode. As a result, one would expect there to be p-1 negative conductance peaks for a device with p periods [13]. In this section, we shall apply the above criterion to sequential resonant tunneling through $Al_{0.3}Ga_{0.7}As/GaAs$ MQW diode structures.

2.2.3 Sample structure of multiple quantum well diodes

The multiple quantum well structures we have studied in this section are molecular beam epitaxy (MBE) grown heterostructures consisting of the following common features. The MQW diode #1 (#2) was grown on n^+-GaAs substrates and consist of 20 (40) periods of 25 (35) nm-wide GaAs quantum wells and 10 nm-thick $Al_{0.3}Ga_{0.7}As$ barriers. In the following, we will discuss the I-V characteristics mainly of the samples was uniformly doped with Si up to 5×10^{15} cm^{-3} in the whole active region The substrate temperature during MBE growth of the active regions of the samples was kept at 530 °C to suppress the
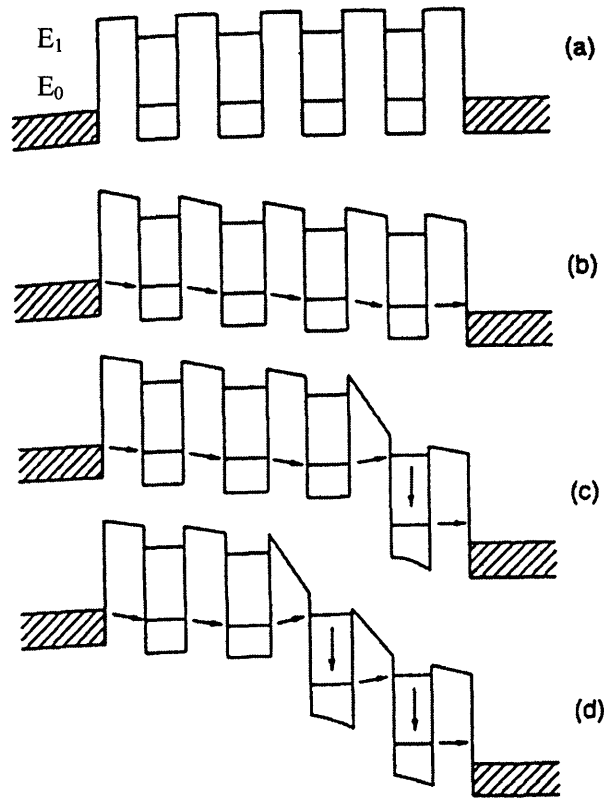
Fig. 2.2 Schematic band diagram of the superlattice for several values of the average potential drop per period Vp. (a) Zero bias. (b) Sequential resonant tunneling through the ground state E_0 for $V_p < 2\hbar/\tau_1$; arrows indicate electron transport. (c) Formation of first high-field domain for V_p slightly greater than $2\hbar/\tau_1$. Sequential resonant tunneling occurs through E_0 in the low-field region and through the first excited state E_1 in the high-field region. (d) Expansion of the high-field domain by one additional quantum well for a voltage increase of ΔV [13].

dopant segregation. The MQW active regions were sandwiched between 0.5 μm-thick n$^+$-GaAs capping and buffer layers. The samples were etched into mesa shapes defined by standard photolithography. The *I-V* experiments were performed at T = 4.2 K. Figure 2.3(a) shows a schematic illustration of band diagram the multiple quantum well and Fig 2.3(b) shows the sample structure of the MQWs. The quantized energy levels of the first five subbands calculated by using Kronig-Penny model are listed in Table 2.1, where the inside of brackets shows the miniband width.

2.2.4 2D-2D sequential resonant tunneling

Figure 2.4 shows the current-voltage (*I-V*) characteristics of the multiple quantum well diode #1 for a voltage up-sweep and down-sweep. As shown in Fig. 2.4, the MQW diode exhibits clear periodic NDRs, as expected from conventional picture [12-18], and the *I-V* curves show plateau-like steps which have rather constant peak and valley currents. Furthermore, a unique hysteresis between the *I-V* curves for the sweep-up and sweep-down is observed. This behavior has been well explained by a formation of high-field domains and sequential resonant tunneling. The observed voltage spacing between NDRs are well explained by the spacing of quantized energy levels in the quantum wells.

First, we discuss the voltage spacing between NDRs of the MQW diode. Figure 2.5 shows a schematic illustration of the energy band diagram of MQW structure and an electron transport process. Two dimensional (2D) electrons formed in each wells due to a confinement of a motion to z-direction. Parabolic curves in the wells are energy dispersion of 2D electrons in parallel with to the hetero surface plane. In principle, due to the 2D nature of electron gas in the well, resonant tunneling is possible only when the energy levels in each well coincide, a condition generally not fullfilled in the presence of a field. However, in the presence of acoustic phonon and impurity scattering within each well, conservation of energy and momentum is relaxed and resonant tunneling is possible provided that $eV \ll \hbar/\tau_0$, where V is the potential difference between the adjacent wells

$L_b = 10$ nm $L_w = 25/35$ nm   Periods ($\times 20/40$)

$E_4 = 216.8$ meV

$E_3 = 138.7$ meV

$E_2 = 78.0$ meV

$E_1 = 34.7$ meV

$E_0 = 8.7$ meV

250 meV

$Al_{0.3}Ga_{0.7}As$ GaAs

AuGe 0.2×0.2 mm^2 Si

Buffer 1×10^{18}cm^{-3}

MQW   Active Layer

Buffer 1×10^{18}cm^{-3}

n$^+$ GaAs Substrate

In
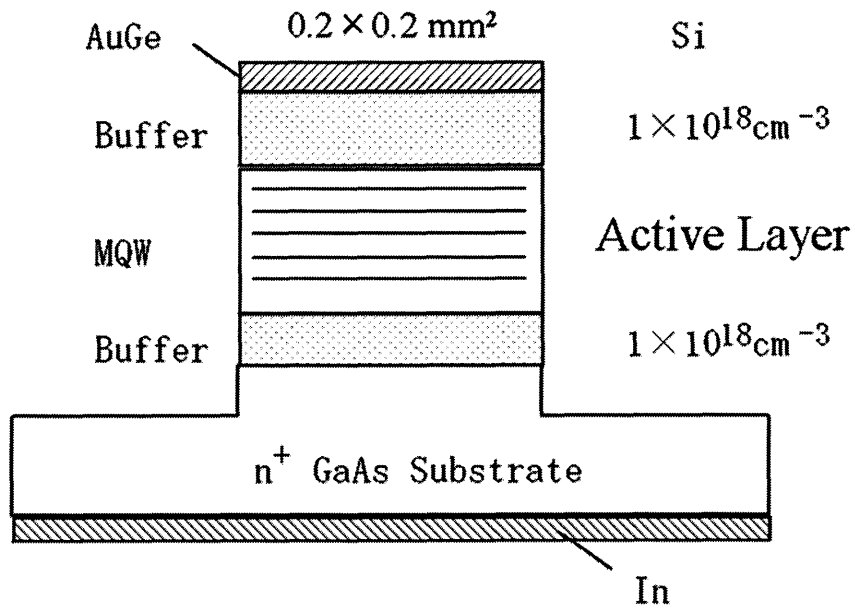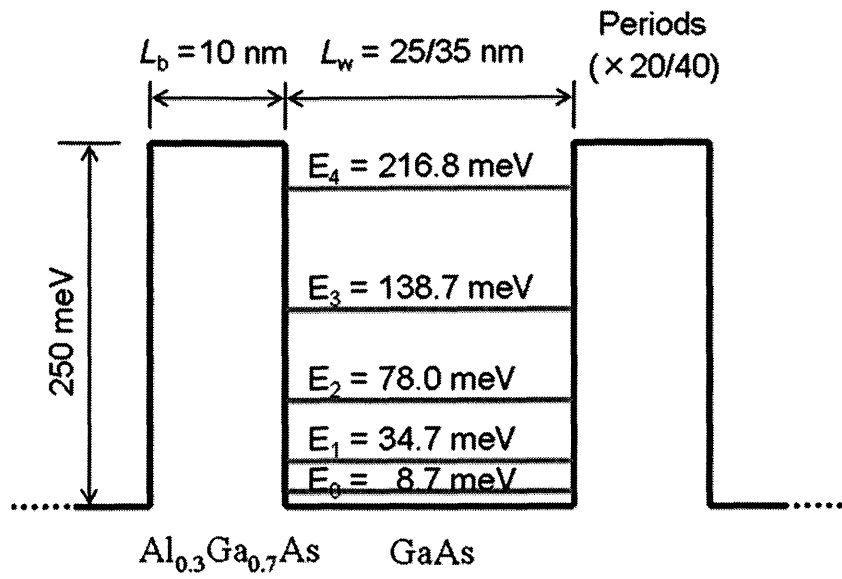
Fig. 2.3   (a) Schematic illustration of band diagram and (b) device structure of the multiple quantum well diode investigated in this study.

Quantized level	#1 (L_w = 25 nm)		#2 (L_w = 35 nm)	
E_0	8.7	(0.7)	4.5	(0.3)
E_1	34.7	(2.5)	17.9	(0.9)
E_2	78.0	(5.7)	40.2	(2.1)
E_3	138.7	(10.0)	71.5	(3.7)
E_4	216.8	(15.5)	111.6	(5.8)

Table 2.1   Quantized energy level of each state in the quantum wells calculated by Kronig-Penny model.
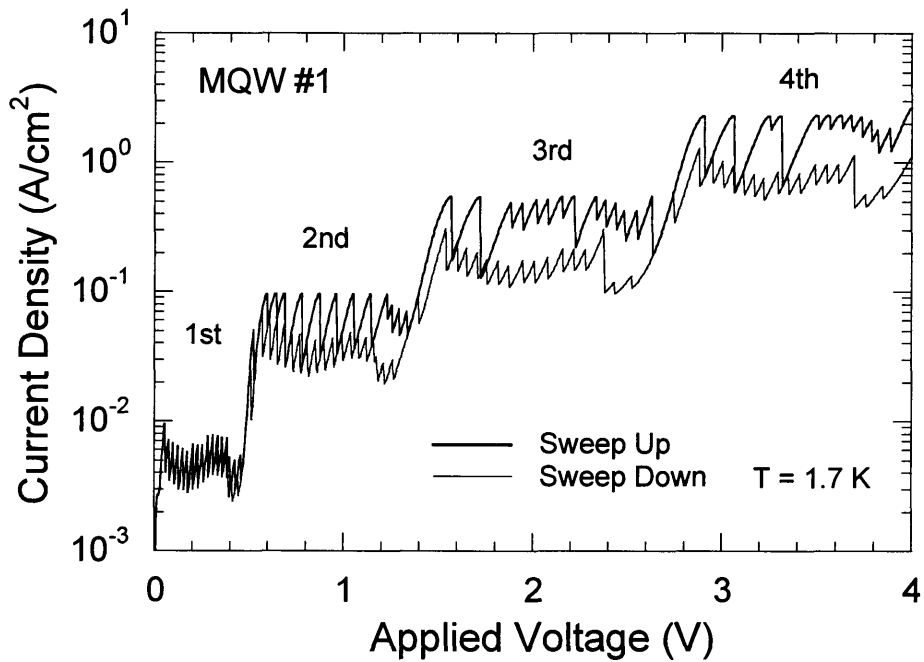
Fig. 2.4 I-V characteristic of the multiple quantum well diode #1 at T = 1.7 K.   The bold solid line shows the data for voltage up-sweep.   The thin solid line shows for down-sweep.

and τ_0 is the ground-state scattering time. Therefore, at small biases, electrons are able to tunnel resonantly through the ground states of each well (Fig. 2.5(a)).

When the potential drop eV across one period is larger than $\hbar/\tau_0$, the uniform field distribution along the MQW becomes unstable due to the negative differential resistance of the junction, and one tunnel junction is switched into a state with high-field domain. As a result, the I-V characteristic exhibits a series of branches as the number of tunnel junctions forming the high-field domain. The resistance across this period becomes much larger and high-field domain forms. Any subsequent increase in the bias will appear across this domain until the ground level rise to within $\hbar/\tau_1$ of the first excited level (E_1) of the next well where upon the resonant tunneling condition is restored (Fig. 2.5(b)). Further increases in bias will cause another well to break off from the resonant condition and the I-V characteristics repeat. Due to the screening effect of the space-charge buildup at large bias, the domain formation is not a random process but occurs first at the collector and then extends one after the other towards the emitter [18]. As a result, one would expect there to be p-1 negative conductance peaks for a device with p periods. From the above discussion, the voltage difference between the NDRs is nearly equal to the energy separation between the quantized energies. Table 2.2 shows a comparison between theoretical energy differences of quantized levels and measured ΔV's in each plateaus of the sample #1 and #2. The measured ΔV's are in good agreement with the theoretical energy differences between the quantized levels.

2.2.5 High-field domain formation

Next, we will discuss another feature that the high-field domain formation leads to hysteresis in the I-V characteristics of MQW diode. Fig. 2.6(a), (b), and (c) show blowups of the I-V characteristics in the 1st, 2nd, and 3rd plateaus, respectively. The number of current branches is roughly equal to the number of MQW. The large hystereses are observed in each plateau between the I-V characteristics for voltage
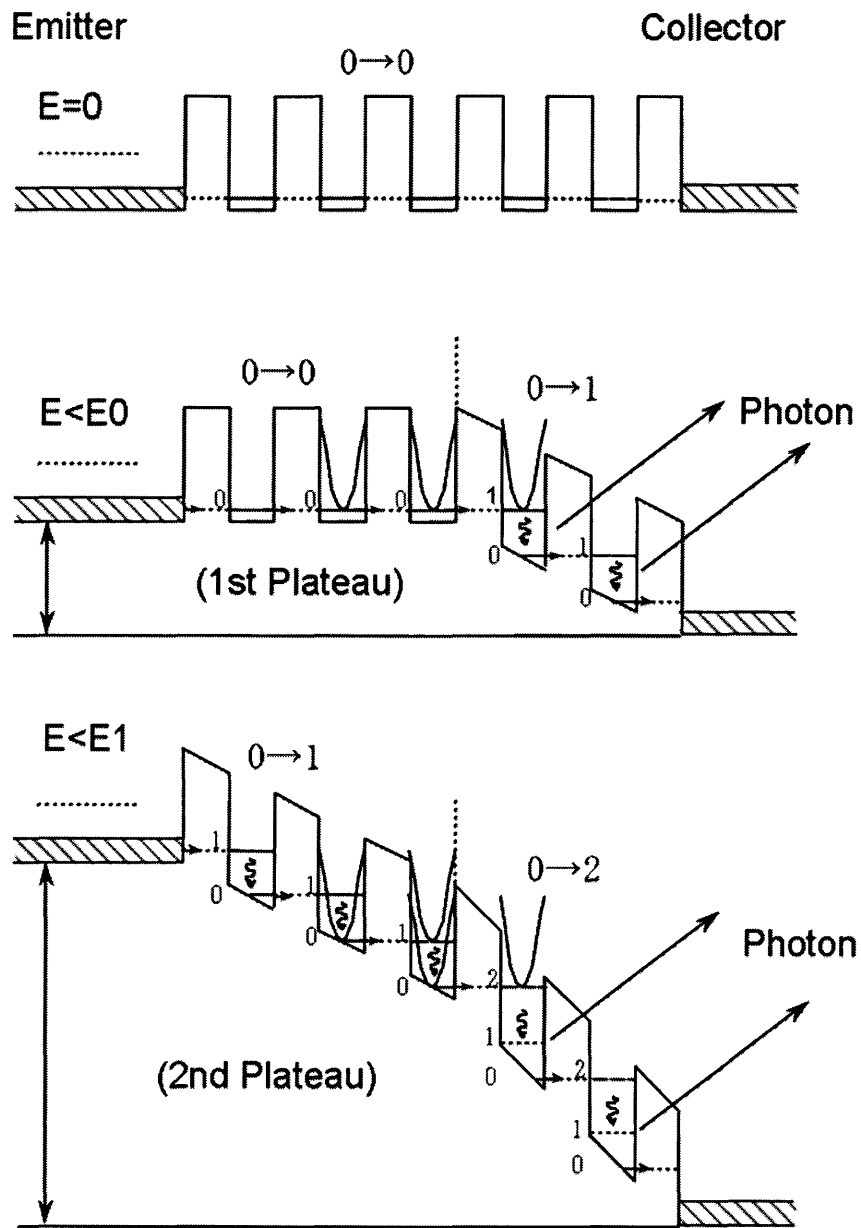
Fig. 2.5 Band diagram of MQW under applied electric fields such as flat band (upper panel), 1st plateau (middle panel), and 2nd plateau (lower panel).

#1 (L_w = 25 nm)

Plateau	$\overline{\Delta V}$ (mV)	Energy difference	Theory (meV)
1st	23.9	E_{01}	26.0
2nd	40.3	E_{12}	43.3
3rd	61.3	E_{23}	60.7
4th	63.3	E_{34}	78.1

#2 (L_w = 35 nm)

Plateau	$\overline{\Delta V}$ (mV)	Energy difference	Theory (meV)
1st	8.5	E_{01}	13.4
2nd	20.4	E_{12}	22.3
3rd	35.4	E_{23}	31.3
4th	44.0	E_{34}	40.1

Table 2.2　a comparison between theoretical energy differences of quantized levels and measured ΔV's in each plateaus of sample #1 and #2.

up-sweep and down-sweep. Furthermore, the hysteresis becomes larger as higher plateaus.

Goldmann predicted the existence of hysteresis by charge accumulation for double barrier resonant tunneling structure [19]. However, this is not able to explain the large hysteresis in the 2nd and 3rd plateau of the I-V characteristics. Kawamura has argued that the mechanism of the hysteresis is the formation of off-resonant region [20]. However, it is not clear why the off-resonant domain is formed. The mechanism of hysteresis is explained by the 2D-2D tunneling and its tunneling resistance as follows.

MQW sequential resonant tunneling structure is modeled by a series of N identical circuits consisting of a nonlinear resistor and a capacitor in parallel (Fig. 2.7) [21], where N is the number of tunnel junctions. The I-V characteristic of the resister is identical to that for a single tunnel junction separating two 2D electron gases. Therefore ideal I-V characteristic of series connection of the 2D-2D tunnel junctions is shown as Fig. 2.8(a). We added a small resistance Rs compared with the tunnel current to the ideal I-V characteristic shown in Fig. 2.8(a). In this case, the Rs means the load line in the tunnel junctions. If a bias voltage is applied to the sequential resonant tunneling structure with Rs, it is able to select only one stable current at the specific bias voltage where a discontinuity occur (Fig 2.8(a)). The expected I-V characteristics for a voltage up-sweep and down-sweep are indicated in Fig 2.8(a). When the Rs becomes lager (Fig. 2.8(b)), it is able to select two or more stable currents at a bias voltage. As a result, the expected I-V characteristic shows a large discontinuity with hysteresis shown in Fig 2.8(b). Imperfections and fluctuations of structural properties and doping in the growth direction of the MQW result in a sequence of longer and shorter branches in the I-V characteristics. The plateau-like steps are a result of the quantization of the electric charge of the stationary boundary of the high-field domain. When the current jumps from one branch to the next, the charge layer at the boundary between the domains moves from one well to the adjacent well. Because each branch reflects the charging or discharging of the well at the domain boundary, a hysteresis effect is expected. It is clear from the I-V characteristic shown in
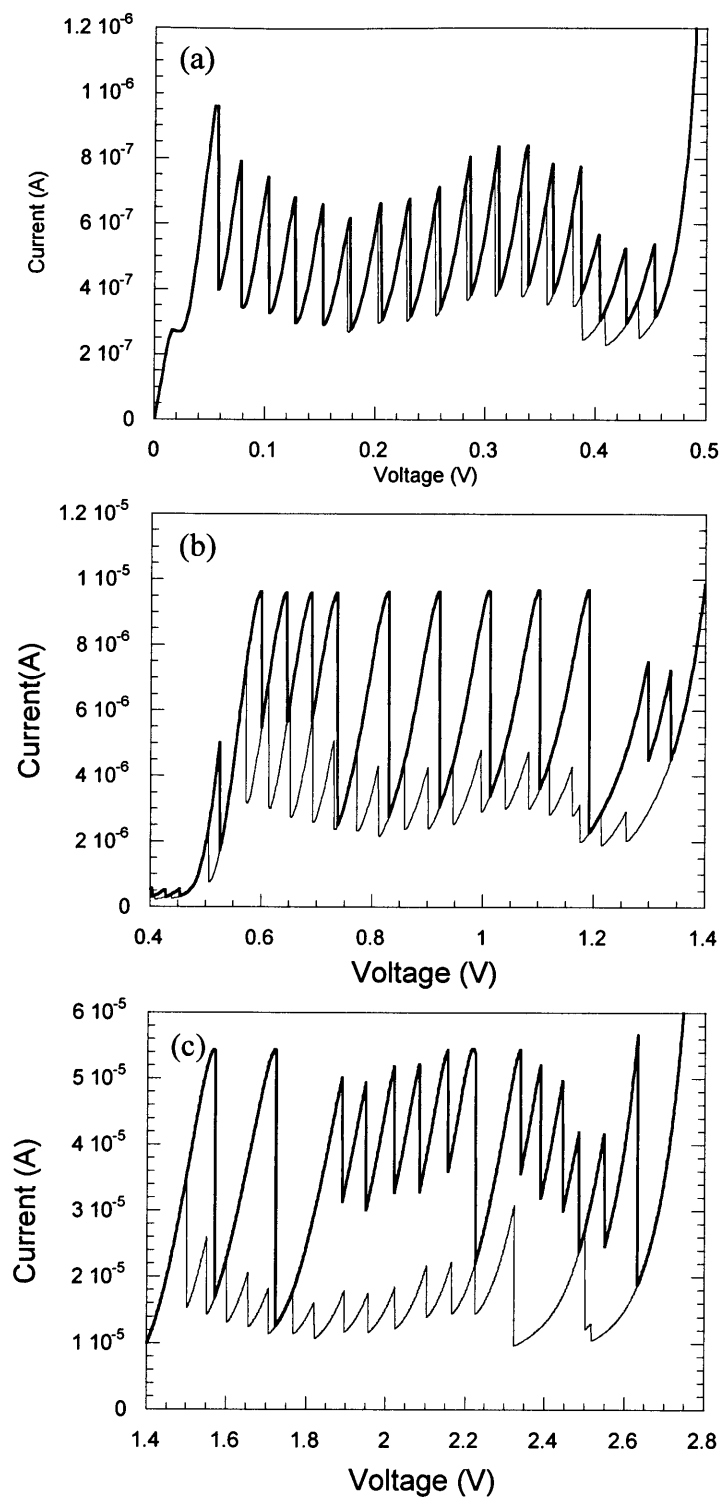
Fig. 2.6 Blowup of the current-voltage characteristics shown in Fig 2.4 for (a) 1st, (b) 2nd, and (c) 3rd plateau.
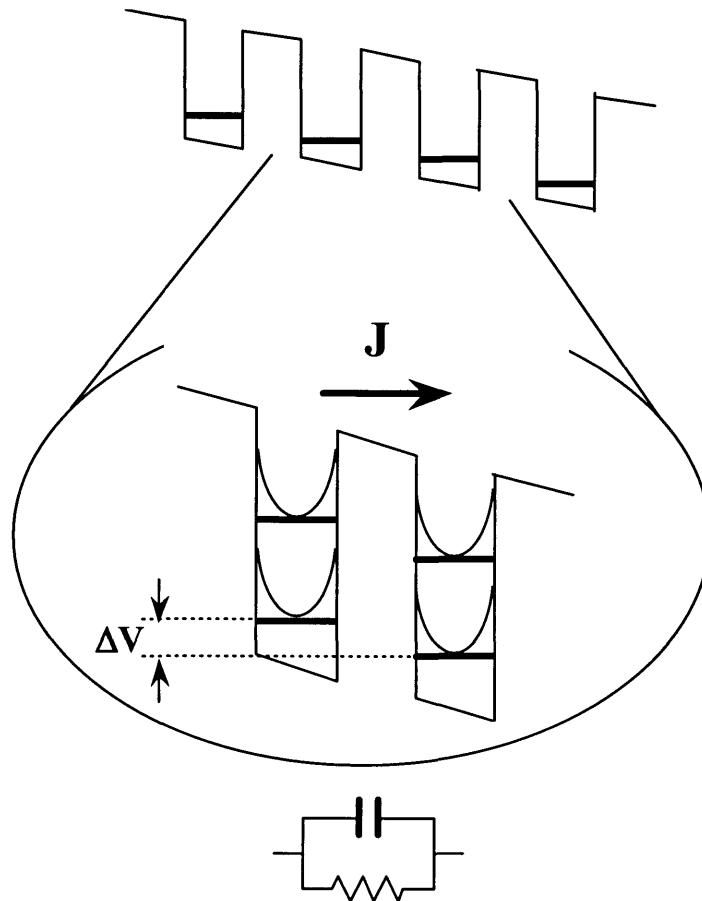
Fig. 2.7   Equivalent circuit of 1 segment of MQW consist of 2D-2D tunnel junction is composed by a tunnel resistance and barrier capacitance.
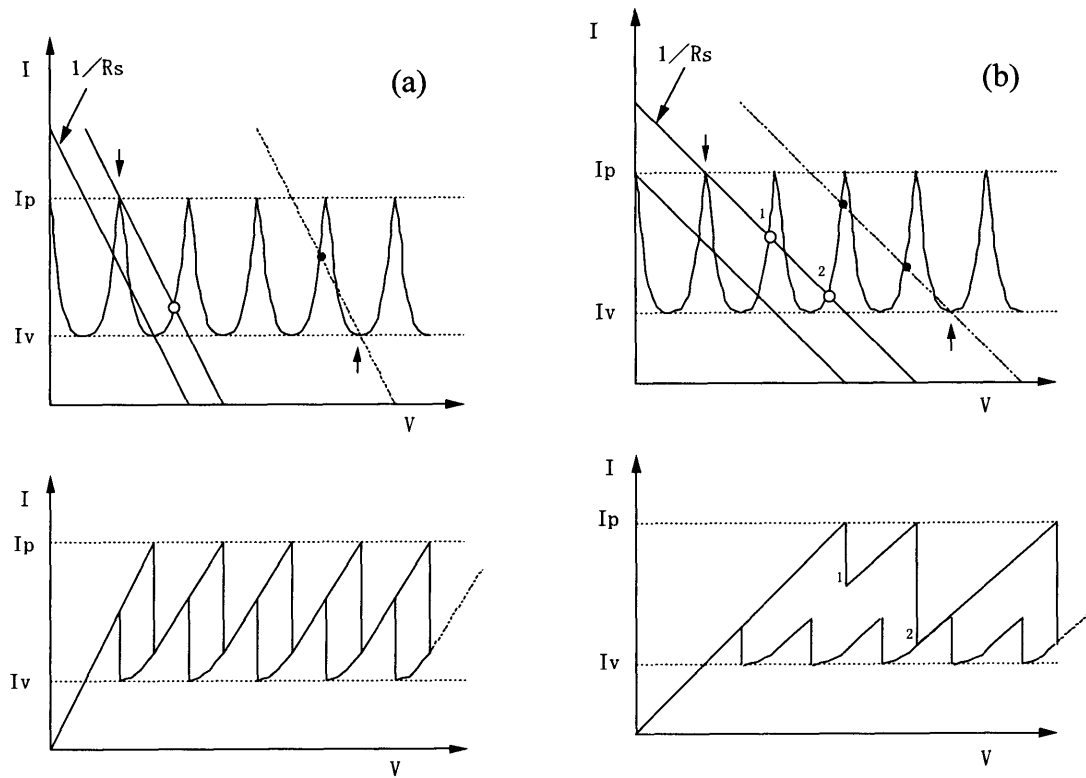
Fig. 2.8 Ideal current-voltage characteristics of 2D-2D tunneling and series tunneling resistance Rs (upper panel), and observed current-voltage characteristics (lower panel) for (a) 1st and (b) 2nd plateaus. Rs of 1st plateau is smaller than that of 2nd plateau.

Fig. 2.6 (a) – (c) that the sample can exhibit mulitistability in the specific voltage range, where the two current branches partially coincide. This multistability occurs because for each current branch the domain boundary is located in a different well. Thus having two separated current branches at a given bias voltage means that depending on the sweep history the domain boundary can be found in one of two adjacent wells [22].

2.3 Supply-function dependent current-voltage characteristics

2.3.1 Introduction

It is well known that the I-V characteristics due to sequential resonant tunneling through active regions of doped MQW diodes show plateau-like regions, each of which exhibits periodic NDRs with rather constant peak and valley current. Such a behavior has been explained by the formation of high field domains and sequential resonant tunneling through them [12-18]. However, full understanding of the transport mechanism in MQW structures has not yet been achieved.

In this section, we investigate tunneling I-V characteristics of $Al_{0.3}Ga_{0.7}As$/GaAs MQW diodes with various electron densities, N_s, and scattering rates, Γ. Although we observed clear periodic NDRs due to the formation of high-field domains for the samples with low N_s and Γ, no NDRs were observed in the *first* plateau region of the I-V characteristics of the samples with high N_s and Γ. By using a theoretical model for sequential tunneling process, we show here that the formation of high-field domains in doped MQW diodes is *not trivial* and that it depends on the shape of the electron supply-function and the tunneling rate between adjacent coupled quantum wells (QWs).

2.3.2 Sample structure

All the MQW diodes investigated in this section were grown by molecular beam

epitaxially (MBE) on n^+-GaAs substrates and consist of 20 periods of 25 nm-wide GaAs quantum wells and 10 nm-thick $Al_{0.3}Ga_{0.7}As$ barriers. In the following, we will discuss primarily the I-V characteristics of two samples; one of the sample (MQW1) was uniformly doped with Si up to 5×10^{15} cm^{-3} in the entire active region, while the other sample (MQW2) was δ-doped at the center of the $Al_{0.3}Ga_{0.7}As$ barriers with Si up to 2.8×10^{11} cm^{-2} per layer. The substrate temperature during MBE growth of the active regions of the samples was kept at 530 °C to suppress the dopant segregation. The MQW active regions were sandwiched between 0.5 μm-thick n^+-GaAs capping and buffer layers. The samples were etched into mesa shapes defined by standard photolithography. All experiments were performed at liquid He temperatures.

2.3.3 Current-voltage characteristics of highly-doped structure

Figure 2.9(a) and (b) show the measured I-V characteristics of the MQW1 and MQW2 diodes, respectively. As shown in Fig. 2.9(a), the I-V characteristics of the MQW1 consist of plateau-like regions, in each of which clear periodic NDRs with rather constant peak and valley current are observed, as expected from a conventional picture [12-18]. The electron transport mechanism through such a uniform-doped MQW structure has been attributed to the resonant tunneling process between two-dimensional (2D) subbands in the neighboring quantum wells. The plateaus in the I-V characteristics are formed as the high field domains grow with an external bias. The voltage differences between the successive NDRs in each plateau are expected to be approximately equal with the energy differences between 2D subbands in the quantum well [12-18]. As long as the 2nd plateau are concerned, the I-V curves of the MQW2 shown in Fig. 2.9(b) exhibit characteristics similar to those observed for the MQW1. However, NDRs are completely absent in the first plateau region of MQW2 (Fig. 2.9(b)). Such a contrast in the I-V characteristics was observed *only for the first plateau region*; clear NDRs are observed for higher plateaus in all the MQW samples.
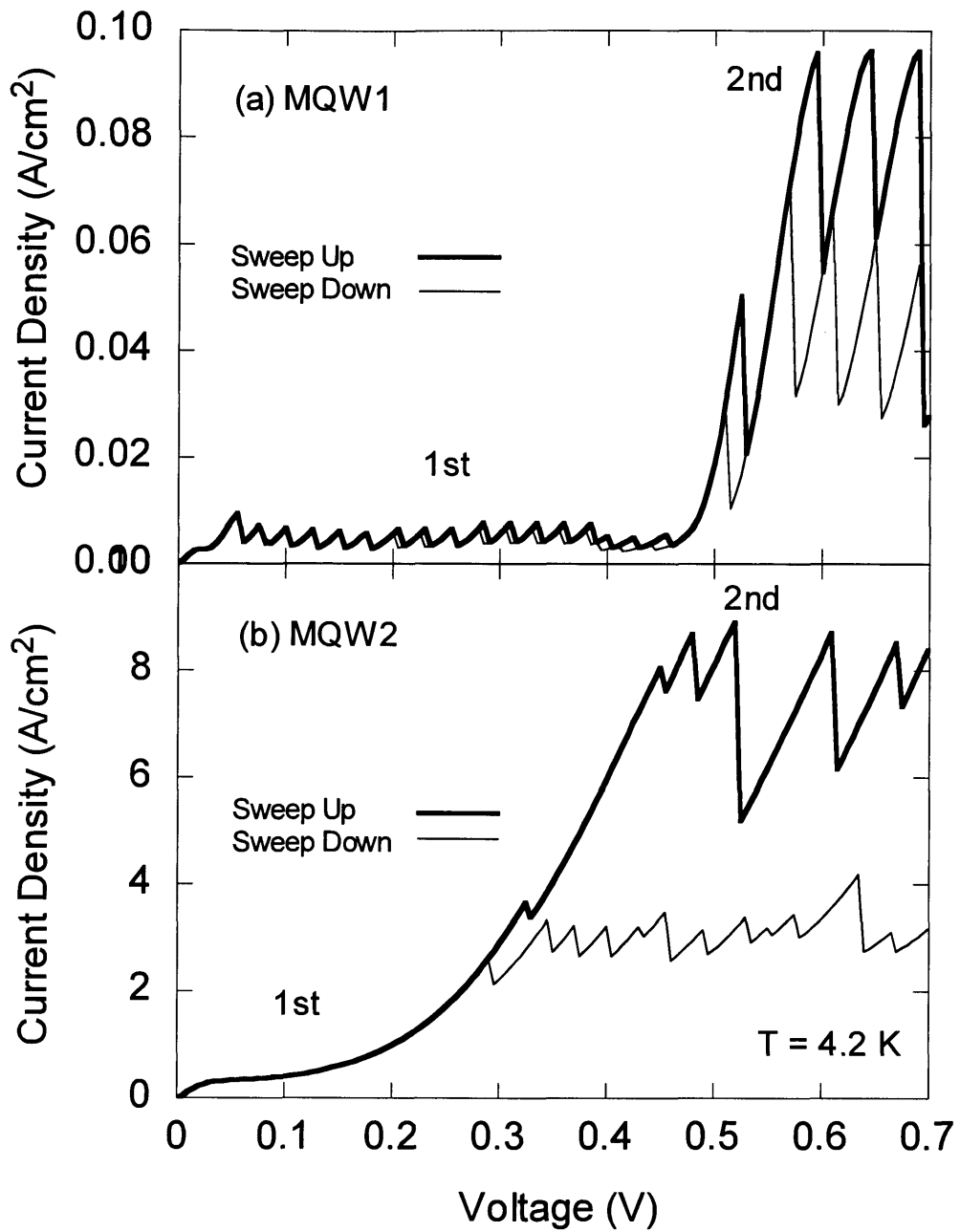
Fig. 2.9 The first- and second-plateau regions of the *I-V* characteristics of MQW1 (a) and MQW2 (b) measured at 4.2 K.

2.3.4 Condition for high-field domain formation

It is well known that the electron transport mechanism through a MQW structure has been attributed to the resonant tunneling process between the 2D subbands in the neighboring quantum well. In this MQW structure, 2D-2D resonant tunneling occurs only when the adjacent 2D-subbands in the QWs coincide with each other. Therefore, transmission probability for ideal 2D-2D resonant tunneling is given by the δ-function when the potential difference (ΔV) becomes equal to the energy differences between the excited subbands. In the actual systems, the transmission probability, however, has a Lorentzian shape with level broadening Γ due to scattering. Thus, the total transmission probability is produced by adding the 1st peak Lorentzian (the transmission probability between the adjacent 2D ground sabbands, $T_{0\to0}$ (ΔV)) and 2nd peak Lorentzian (the transmission probability between the ground and first excited subbands, $T_{0\to1}$ (ΔV)) and other higher case. The peak values of the transmission probabilities are proportional to the square of Δ_{SAS} which is the energy differences between symmetric and asymmetric eigen energies.

In particular, the tunneling current in the first plateau region involves the tunneling between the adjacent two-dimensional ground subbands ($0\to0$) in low-field domain and the tunneling between the ground and the first excited subbands ($0\to1$) in the high-field domain. These two tunneling currents must be balanced because of the current continuity throughout the MQW structure. Here, *a frustration occurs in the low-field domain*; the tunneling rate between the adjacent 2D ground subbands, $T_{0\to0}(\Delta V)$, becomes maximum when the potential difference ΔV between the adjacent two QWs is zero. However, the number of available states for tunneling, *i. e.*, the electron supply-function $S(\Delta V)$, is zero when $\Delta V = 0$ and increases with increasing ΔV. We will show such a frustrated electron conduction in the low-field domain can give rise to a disappearance of the periodic NDRs.

2.3.5 Theoretical model for tunneling current

In order to examine such a possibility quantitatively, we have considered the *I-V* characteristics of the samples studied here by using a simple theoretical model for *sequential* resonant tunneling. "*Sequential tunneling*" is justified by the fact that the coherent oscillatory tunneling time between the neighboring QWs, τ_t ($\equiv 1/\Omega_n$; $\hbar\Omega_n$ is the symmetric-antisymmetric gap of the resonantly coupled ground and *n*-th subbands), is of the order of 100 ps for the present samples, which is much longer than the typical scattering times in each QW. Then, the entire MQW structure can be decomposed into a series connection of coupled double QW segments. Consequently, the overall *I-V* characteristics of the MQW diode is governed by the "*I-V* characteristics of the coupled double QW segment", although such segmental *I-V* characteristics are not measurable. In the following, we simulate the segmental *I-V* characteristics by calculating the tunneling rate and the electron supply-functions.

The tunneling currents between the coupled double QWs (Fig. 2.11) have been calculated using the following four assumptions; (1) Electrons relax their energies and momentum after elastic tunneling via inelastic scattering process (sequential tunneling). (2) Each quantized subbands are inhomogeneously broadened and are characterized by a simple Lorentzian with an energy broadening Γ ($\equiv \hbar/\tau_s$; τ_s is the single particle scattering time) [23,24]. (3) The amplitude of the transmission probabilities are set to be proportional to the resonant coupling strength of the 2D subbands, which is given by $(\Delta_{SAS})^2$ [23,24]. (4) Inelastic tunneling channels such as phonon assisted tunneling are neglected. In such a case, the tunneling current can be calculated by following the theory developed by Kazarinov and Suris [23,24] as;

$$J = T(\Delta V) \cdot S(\Delta V) \text{ , where} \qquad\qquad (2.1)$$
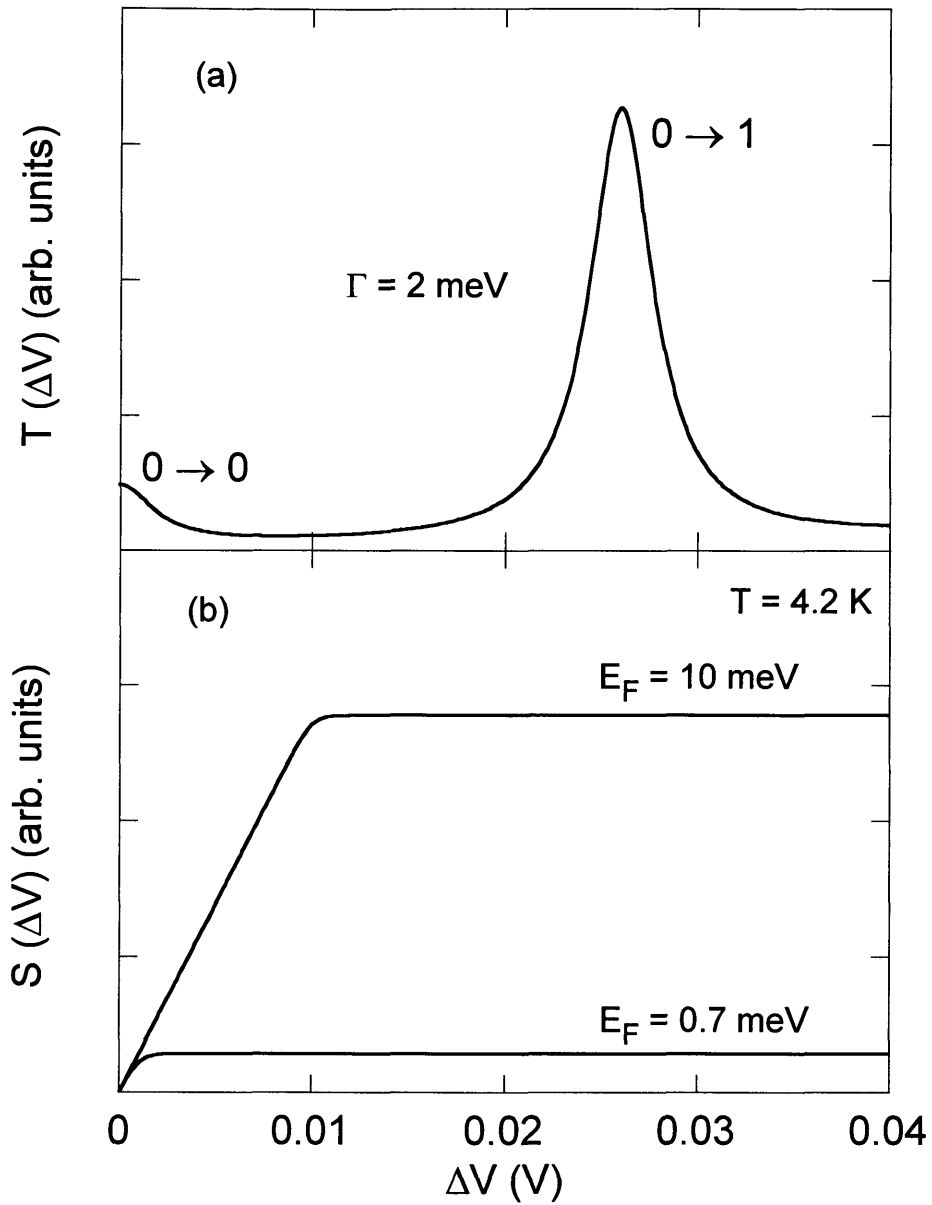
Fig. 2.10 Calculated transmission probability $T(\Delta V)$ (a) and electron supply function $S(\Delta V)$ (b). The parameters used in the calculation are listed in the figure.

$$T(\Delta V) \equiv \sum_{n=0}^{\infty} \frac{2|\Omega_n|^2 \tau_s}{1 + \varepsilon_n^2 \tau_s^2 + 4|\Omega_n|^2 \tau_s \tau_e} \text{, and} \qquad (2.2)$$

$$S(\Delta V) \equiv \frac{em^*}{\pi \hbar^2} \int_{-\infty}^{\infty} [f(E) - f(E + e\Delta V)] \, dE. \qquad (2.3)$$

Here, E_n is the energy difference between the n-th and ground subbands, $\hbar \varepsilon_n$ ($= e\Delta V - E_n$) the energy detuning from the resonance and τ_e the energy relaxation time. Figure 2.10(a) shows the calculated tunneling rate $T(\Delta V)$ for an $Al_{0.3}Ga_{0.7}As$ (10 nm)/GaAs (25 nm) coupled QW structure with $\Gamma = 2$ meV, which is a typical value in our samples. The number of available states for the tunneling process is expressed by the electron supply-function. For the case of 2D-2D tunneling, $S(\Delta V)$ is given by the product of the density of states for electrons in two-dimensions and

$\int_{-\infty}^{\infty} [f(E) - f(E + e\Delta V)] \, dE$, where $f(E)$ is the Fermi-Dirac distribution function. $S(\Delta V)$'s

calculated for $E_F = 0.7$ meV and 10 meV at $T = 4.2$ K, which correspond to the cases of MQW1 and MQW2, respectively, are shown in Fig. 2.10(b) [25]. $S(\Delta V)$ increases linearly with ΔV until $e\Delta V$ reaches E_F and, then, saturates.

The I-V characteristics of coupled double QW segments are, then, given by the product of $T(\Delta V)$ and $S(\Delta V)$, which are shown in Fig. 2.11(a) and (b) for the cases of $E_F = 0.7$ meV and 10 meV, respectively. For the case of $E_F = 0.7$ meV (Fig. 2.11(a)), since $S(\Delta V)$ saturates at small ΔV, the shape of the I-V characteristics of the coupled QW segment is dominated by $T(\Delta V)$ and shows clear NDRs for tunneling between the adjacent ground subbands ($0 \rightarrow 0$ tunneling) as well as tunneling from the ground subband to the first excited subband ($0 \rightarrow 1$ tunneling). When such segments are connected in series and a bias voltage is applied to the entire MQW structure, two stable field states become possible due to the current continuity condition, leading to a formation of high-field domains and the appearance of periodic NDRs in the overall I-V characteristics. This is actually what is
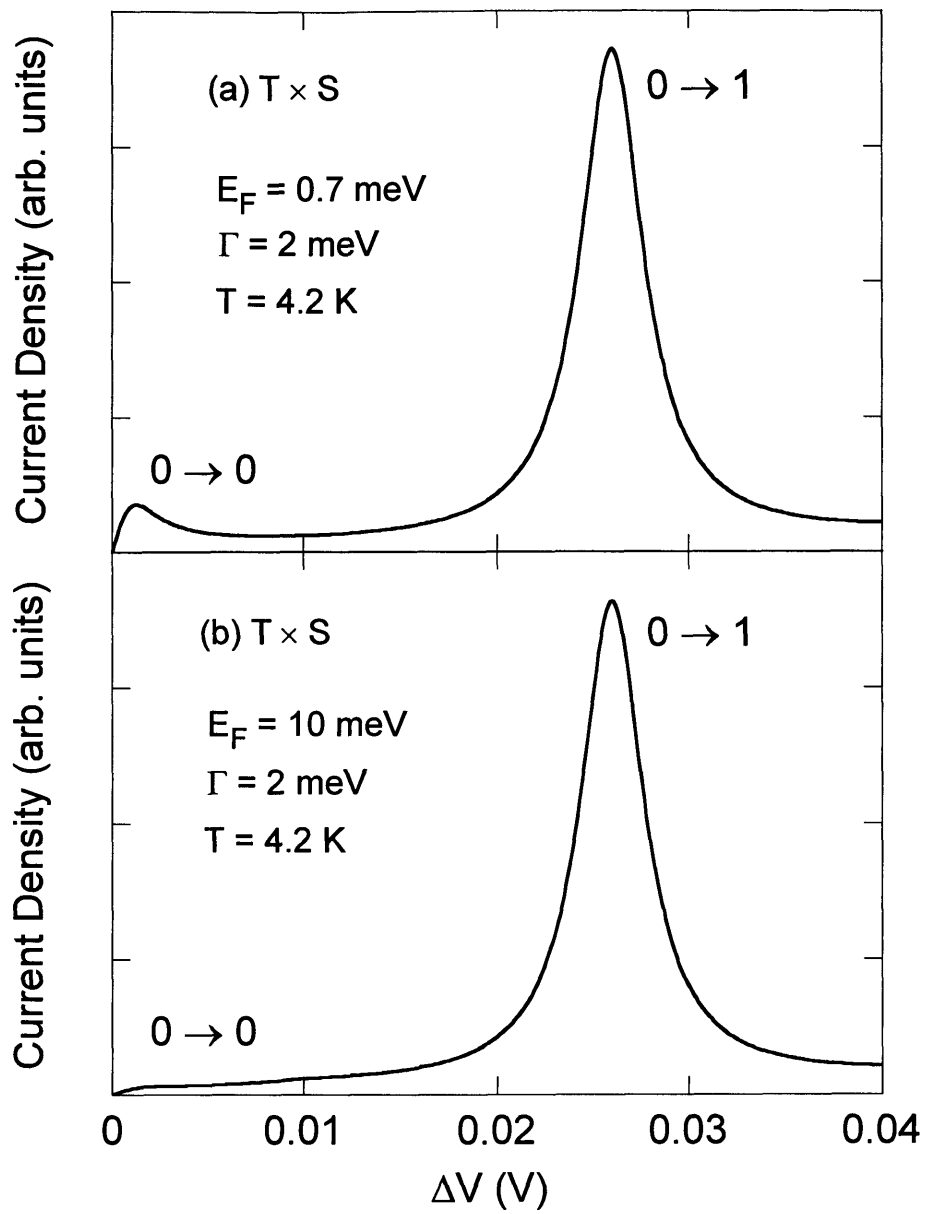
Fig. 2.11 *I-V* characteristics of coupled QW segments calculated for (a) E_F = 0.7 meV and (b) E_F = 10 meV. Γ was assumed to be 2 meV.

observed in the measured I-V characteristics of MQW1 (Fig. 2.9(a)). In contrast, when E_F = 10 meV, the segmental I-V characteristics (Fig. 2.11(b)) do not show a NDR for the $0 \rightarrow 0$ tunneling process, since the increase in $S(\Delta V)$ with ΔV overwhelms the decrease in $T(\Delta V)$. In such a case, when a bias voltage is applied to the MQW structure, only one stable field is established in the entire structure and the overall macroscopic I-V characteristics do not exhibit periodic NDRs. In spite of the simplicity of the present theoretical model, the shape of the $0 \rightarrow 0$ part of the segmental I-V (Fig. 2.11(b)) well reproduces the behavior of the measured first plateau of the I-V characteristics of MQW2 shown in Fig. 2.9(b). The appearance/disappearance of periodic NDRs is, thus, controlled by the interplay of the reduction of $T(\Delta V)$ and the increase of $S(\Delta V)$ with increasing ΔV. It should be emphasized that the disappearance of periodic NDRs due to a frustrated transport in the low-field domains occurs only in the first plateau region, since $S(\Delta V)$ is always finite for the tunneling process from the higher subbands.

2.3.6 Phase diagram of boundary for formation of high-field domain

As discussed previously, the sequential I-V characteristics between the adjacent two QWs are given by the product between the transmission probabilities and the supply functions. When the segmental I-V characteristics have negative resistance region, the clear periodic NDRs appear in the overall I-V characteristics. On the other hand, if there is no negative resistance region in the segmental I-V characteristics between the adjacent QWs, NDRs disappear in the overall I-V characteristics. By using the present theoretical model, we can draw a phase diagram which shows the boundary for the formation of high-field domains as a function of the subband broadening Γ and the electron Fermi energy E_F, as shown in Fig. 2.12 [26]. In the figure, the experimental data points for MQW1 and MQW2 are plotted together with the data points for two other samples. Full circles denote the samples which show clear NDRs, while no NDRs are observed for the samples denoted by open circles. Generally speaking, high-field domains are formed when Γ and
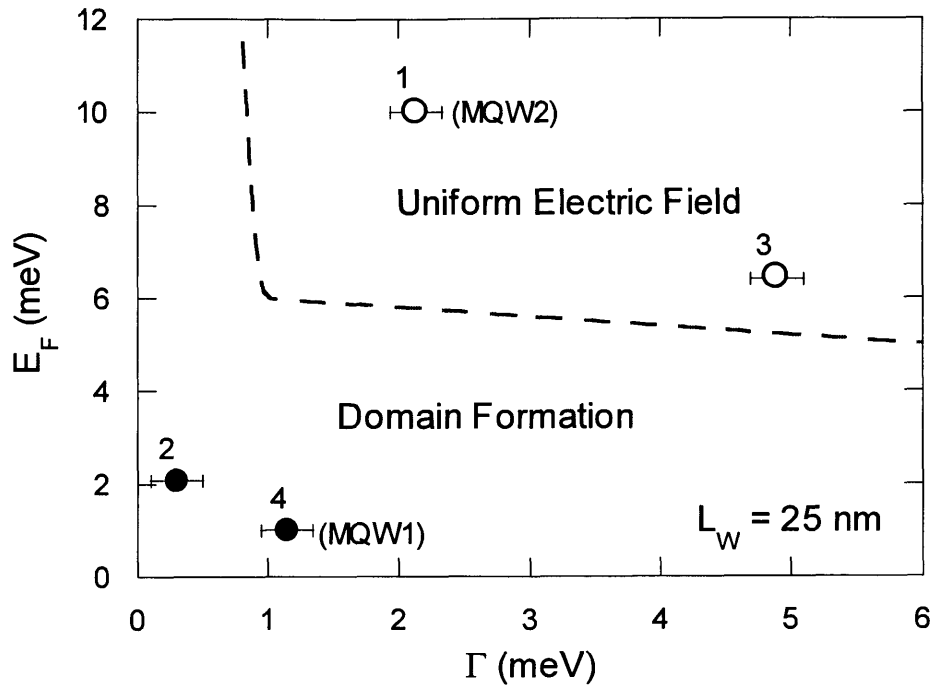
Fig. 2.12 Calculated boundary for the formation of high-field domains is shown by a dashed line as a function of electron Fermi energy and level broadening due to scattering. Experimental data points which do not show periodic NDRs in the first plateau of the *I-V* characteristics are plotted by open circles, while the samples denoted by full circles exhibit clear NDRs.

E_F are small, while uniform electric fields are developed in the MQW structures with large Γ and E_F. The agreement between theory and experiment indicates that the mechanism which governs the formation of high-field domains is well understood by the present simple theoretical model.

2.3.7 Summary

In this section, we have investigated the tunneling *I-V* characteristics of $Al_{0.3}Ga_{0.7}As/GaAs$ MQW diodes with various electron densities, N_s, and scattering rates, Γ. Clear periodic NDRs are observed for the samples with low N_s and Γ, while no NDRs are observed in the *first* plateau region of the *I-V* characteristics of the samples with high N_S and Γ. We have shown that such formation/destruction of the high-field domains in MQW diodes is controlled by the interplay of the tunneling rate and the electron supply-functions between the adjacent coupled QWs. The technological implication of the present result is that by carefully designing the structure and the doping level of MQW diodes it is possible to apply uniform electric field throughout the MQW structure, which would be suitable for realizing novel THz emission/detection devices [27-36].

2.4 Sequential resonant magneto-tunneling through Landau Levels

2.4.1 Introduction

It is known that the current-voltage (*I-V*) characteristics due to sequential resonant tunneling through active regions of doped MQWs show plateau-like regions, each of which exhibits periodic negative differential resistances (NDRs) with rather constant peak and valley current. Such a behavior has been well explained by the formation of high field domains and sequential resonant tunneling through them [12-18]. However, full understanding of the transport mechanism in MQW structures has not been achieved yet.

In this section, we investigate the tunneling *I-V* characteristics of modulation-doped (MD) GaAs/Al$_{0.3}$Ga$_{0.7}$As MQW structures. It is found that the first plateau of the tunneling *I-V* characteristics of the MD-MQWs exhibits a couple of remarkable features; in particular, a strong dependence on a magnetic field, *B*, applied normal to the layer plane is observed. The observed NDRs are identified to be the scattering-assisted sequential resonant tunneling through successive Landau levels. Furthermore, it is found that the observed voltage spacings of the NDRs are systematically smaller than the cyclotron energy. We will show that the observed new *B*-dependent magneto-tunneling phenomena are well explained by the interplay between the scattering-assisted inter Landau-level tunneling and the *B* dependence of the two-dimensional electron supply function.

2.4.2 Sample structure of MQWs

The GaAs/Al$_{0.3}$Ga$_{0.7}$As MQW structures investigated in this section were grown by molecular beam epitaxy (MBE) on n$^+$-GaAs substrates and consisted of 20 periods of 25 nm-wide GaAs quantum wells (QWs) and 10 nm-thick Al$_{0.3}$Ga$_{0.7}$As barriers. For the MD-MQW samples Si was δ-doped at the center of the Al$_{0.3}$Ga$_{0.7}$As barriers. The doping density was set to be 2.8 × 10^{11} cm^{-2}. The substrate temperature during MBE growth of the active region of the MD-MQW samples was kept at 530 °C to suppress the dopant segregation. The MQW active region was sandwiched between 0.5 μm-thick n$^+$-GaAs capping and buffer layers. In a similar manner, a conventional UD-MQW structure was grown for a reference purpose. The active region of the UD-MQW sample was doped with Si up to 5 × 10^{15} cm^{-3}. The samples were etched into mesa shapes with an area of 200 × 200 μm^2 defined by standard photolithography. Alloyed AuGe and In contacts served as the top and bottom electrodes, respectively. All the experiments were performed at liquid He temperatures. For the present MQW structures, the quantized energy levels of the first four subbands calculated by using simple Kronig-Penny model are

E_0= 8.7 meV, E_1 = 35 meV, E_2 = 78 meV, and E_3 = 139 meV, respectively, above the bottom of the conduction band in the GaAs QWs.

2.4.3 I-V characteristics under strong magnetic field

Fig. 2.13(a) and (b) show the *I-V* characteristics of the UD- and MD-MQW structures measured at various magnetic fields applied normal to the interface, respectively. As shown in Fig. 2.13(a), the *I-V* characteristics of the UD-MQW structure consist of several plateau-like regions, in each of which periodic NDRs with rather constant peak and valley current are observed. The electron transport mechanism through such a UD-MQW structure has been attributed to the resonant tunneling process between the two-dimensional (2D) subbands in the neighboring quantum wells [12-18]. The plateau in the *I-V* characteristics are formed as the high field domain grows with an external bias. The voltage differences between the successive NDRs in each plateau is expected to be approximately equal with the energy differences between the 2D subbands in the quantum well [12-18]. In fact, the voltage differences between the NDRs are ΔV = 23.9 ± 4.7 mV for the 1st plateau and ΔV = 40.3 ± 7.4 mV for the 2nd plateau, whereas the calculated energy differences between the quantized levels in the present sample are E_{01} = E_1 − E_0= 26 meV and E_{12} = E_2 − E_1 = 43.3 meV. The good agreement between the experimental and theoretical results supports the transport mechanism mentioned above. It is noted in the Fig. 2.13(a) that the effect of magnetic field, B, applied normal to the heterointerfaces on the *I-V* characteristics is small [14,15].

Fig. 2.13(b) shows the tunneling *I-V* curves of the MD-MQW structure measured at various B. As long as the 2nd, 3rd, and 4th plateaus are concerned, the *I-V* curves of the MD-MQW structure exhibit characteristics similar to those observed for the UD-MQW structure and show weak dependence on B. However, when we pay more attention to the features in the 1st plateau, a couple of remarkable differences are noticed in the *I-V* curves for the MD-MQW structure.
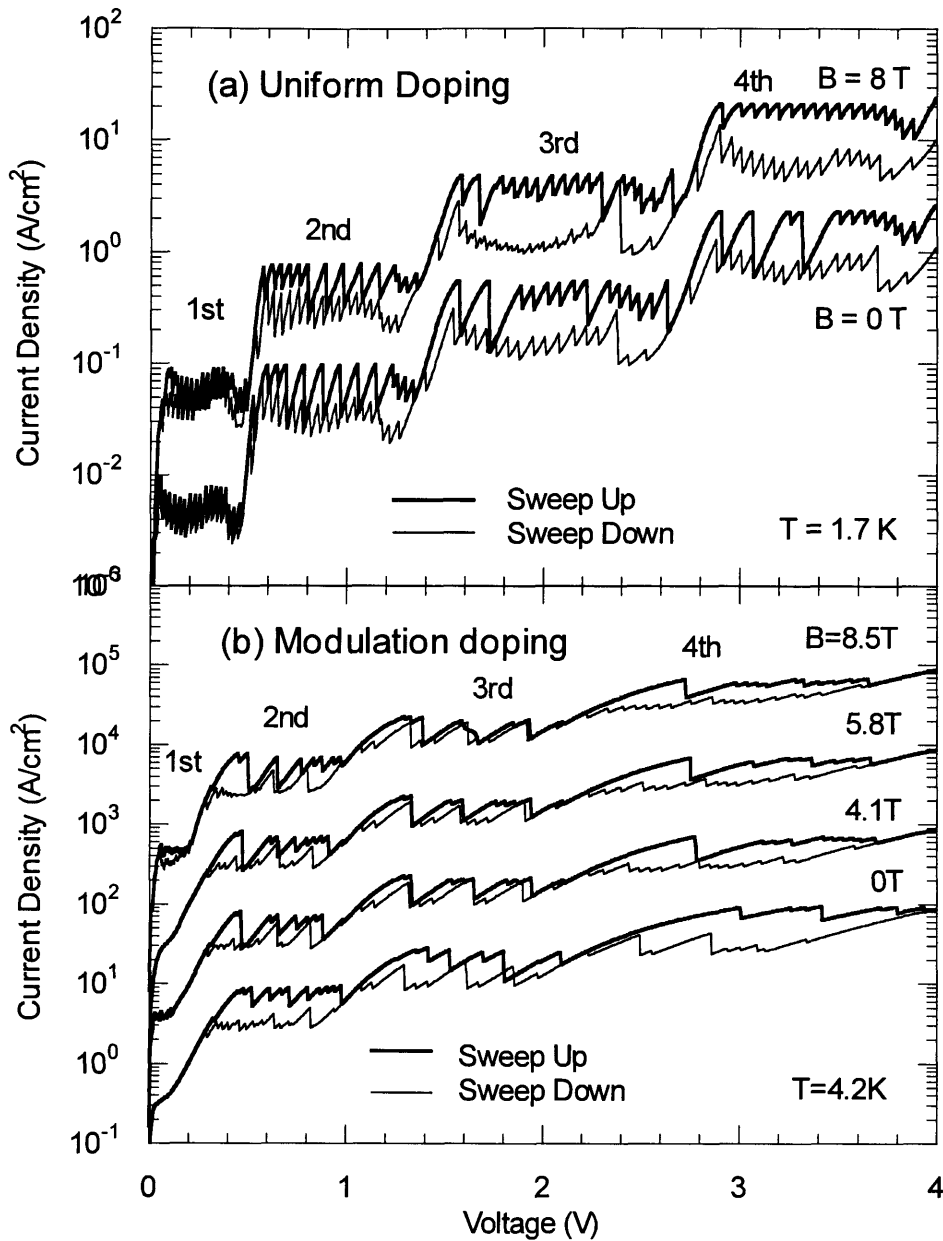
Fig. 2.13 Current versus voltage (I-V) curves of (a) a uniformly-doped and (b) a modulation-doped $Al_{0.3}Ga_{0.7}As/GaAs$ MQW structures. Each I-V curve is shifted by an order of magnitude for clarity. The magnetic field was applied normal to the interface.

Fig. 2.14 shows the blowups of the 1st plateaus in the I-V curves of the MD-MQW structure. There are three remarkable differences noticed between the I-V curves for the MD- and UD- structures; (1) At $B = 0$ the periodic NDRs are completely absent in the 1st plateau; the MD-MQW diode shows an ohmic behavior when $V \leq 20$ mV. This ohmic behavior is due to momentum-nonconserving tunneling process through 20 periods of QWs [37], in each of which the 2D electron mobility μ in parallel with the layer plane is $\sim$ 2×10^4 cm^2/Vs (the equivalent energy broadening is $\sim$ 0.8 meV), as shown later. However, even with further increase of the bias voltage, the diode does not exhibit NDRs. Instead, it supports a rather constant current up to $\sim$ 0.2 V. The origin of the absence of periodic NDRs at $B = 0$ is the interplay between the tunneling probability and supply function of two-dimensional electron system [38]. (2) The appearance/disappearance of the NDRs in the 1st plateau is strongly dependent on the applied magnetic field; at $B = 4.1$ and 8.5 T, clear NDRs are observed, while they are completely absent at $B = 5.8$ T. (3) The voltage differences, ΔV's, between the successive NDRs observed in the 1st plateau are smaller than the energy difference between the first and the second quantized subbands in the MQW, $i.$ $e.$, E_{01} ($\sim$ 26 meV). Furthermore, ΔV also shows a dependence on the applied magnetic fields; ΔV at $B = 8.5$ T is approximately two times larger than that at $B = 4.1$ T. Such peculiar behaviors are characteristics only to the first plateau in the I-V curves. Similar B-field dependent I-V characteristics were observed for a MD-MQW structures with well width of 350 Å.

2.4.4 Sequential resonant magneto-tunneling

In order to understand the behavior of the tunneling current at finite magnetic fields for the MD-MQW structure, we studied the magnetotransport properties of the 2D electrons in parallel with the layer plane. For this purpose, we grew a MD-MQW sample on a semi-insulating substrate under the same growth condition. The sample structure is identical with that for the tunneling measurements, except for the n$^+$-GaAs buffer and
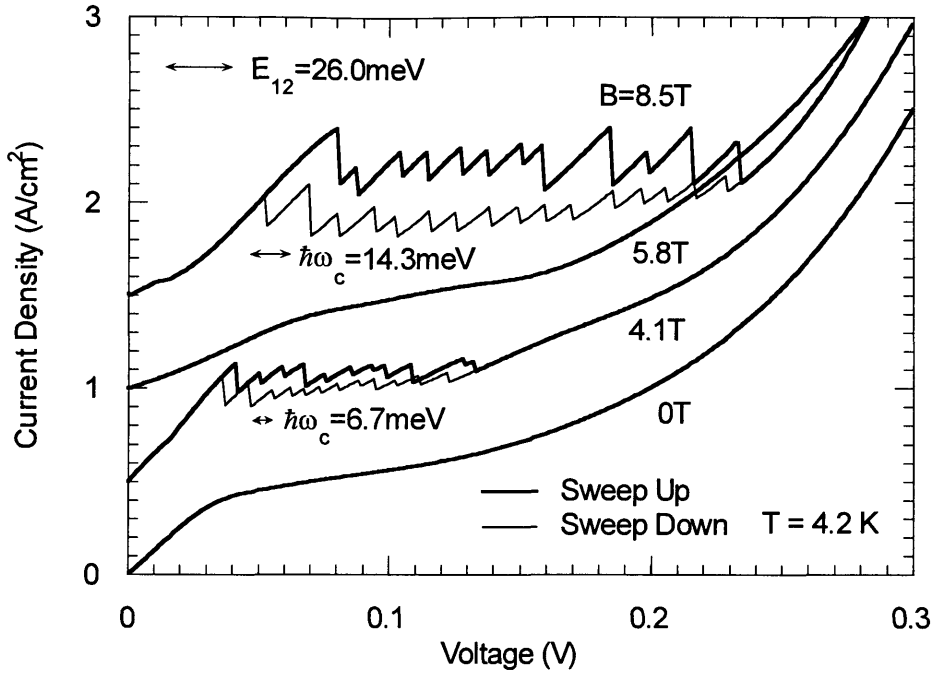
Fig. 2.14 Blowups of the first plateaus in the *I-V* curves of the modulation-doped $Al_{0.3}Ga_{0.7}As/GaAs$ MQW structure measured at various magnetic fields. Each curve is shifted by 0.5 A/cm^2 for clarity.
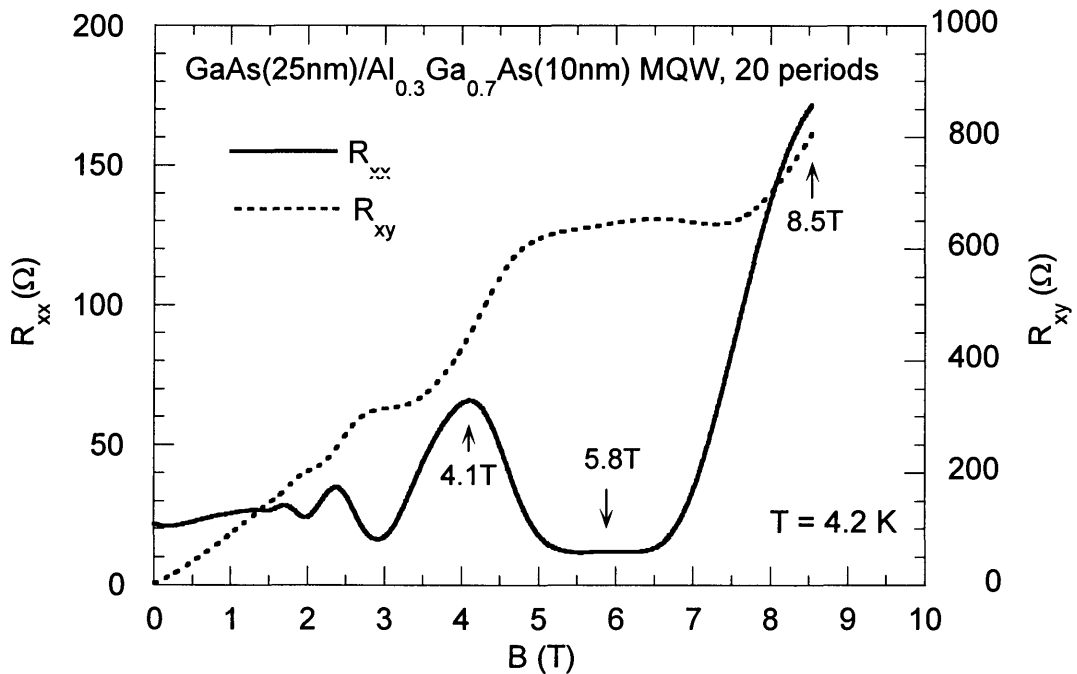
Fig. 2.15 The diagonal (Rxx) and the Hall (Rxy) resistances of the modulation-doped $Al_{0.3}Ga_{0.7}As/GaAs$ MQW structure grown on a semi-insulating substrate.

capping layers. The 2D electron density in each QW, N_s, is 2.8×10^{11} cm^{-2} and μ in the channel is 2×10^4 cm^2/Vs. Fig. 2.15 shows the diagonal (R_{xx}) and the Hall (R_{xy}) resistances of the MD-MQW sample measured at 4.2 K. A comparison between the results of Figs. 2 and 3 indicates that the periodic NDRs in the 1st plateau appear when the topmost occupied Landau level is half filled ($B = 4.1$ ($\nu = 2.8$) and 8.5 T ($\nu = 1.4$), where $\nu = \hbar N_s/eB$ is the Landau level filling factor, $\hbar$ the reduced Planck constant, and e the elementary charge) and that the system shows somewhat insulating behavior when the Fermi level lies in the gap between the Landau levels ($B = 5.8$ T ($\nu = 2.0$)). These facts strongly suggest that the appearance of the B-field dependent NDRs is due to the sequential resonant tunneling through successive Landau levels in the neighboring quantum wells; i. e., tunneling from the i-th Landau level in the n-th QW to the ($i+1$)-th Landau level in the ($n+1$)-th QW in the high field domain. In fact, the voltage differences between the successive NDRs observed at $B = 4.1$ T and 8.5 T are close to the cyclotron energies, $\hbar\omega_c$ at respective B-fields, rather than to E_{12}. This fact further supports the above interpretation. It should be noted here that such inter-Landau level tunneling is usually forbidden due to the parity conservation and becomes allowed only by scattering-assisted processes. The reason why the sequential resonant tunneling via the quantized electric subbands is completely overridden by the inter-Landau level tunneling is not clear at present. It is also noted that for the 2nd and 3rd regions, on the contrary, clear periodic NDR features with voltage spacings approximately equal to the quantized subband spacings are observed.

Next, let us take a closer look at the dependence of the period of NDRs in the 1st plateau on the applied magnetic field. In Fig. 2.16(a), the average voltage spacing, ΔV, between the successive NDRs are plotted as a function of B. ΔV was obtained by dividing the voltage difference between the first and the last peaks of the observed successive NDRs by (N-1), where N is the total number of quantum wells. The error bars indicate typical fluctuations in ΔV. The dotted line in the figure is the cyclotron energy, $\hbar\omega_c$. As seen in the figure, although ΔV roughly follows $\hbar\omega_c$, it shows a rather strong

B-field dependence and is systematically smaller; when the topmost occupied Landau level is half-filled, ΔV becomes close to $\hbar \omega_c / e$, whereas ΔV becomes smaller and eventually whole NDRs disappear as the filling factor ν approaches even integers (note that spin splitting is not resolved).

2.4.5 Broadening of Landau levels

In order to explain the discrepancy between ΔV and $\hbar \omega_c / e$, it is necessary to take into account the broadening of the Landau levels in the sequential resonant tunneling process. When a high field domain structure is formed, current must be conserved throughout the whole diode structure, including both the lower- and higher-field domains, because of the current continuity relationship. However, since the higher-field domain has a capability of flowing a much larger resonant tunneling current at the exact resonance, the higher-field domain must be detuned from the exact resonance by an order of the Landau level broadening, Γ, in order to match the resonance current in the lower-field domain and fulfill the current continuity throughout the device. Consequently, ΔV is, in general, given approximately by $(\hbar \omega_c - \Gamma)/e$ and the discrepancy between $e\Delta V$ and $\hbar \omega_c$ can be regarded as the Landau level broadening, Γ. Therefore, the measurement of ΔV allows us a unique opportunity of spectroscopic determination of the Landau level widths.

In Fig. 2.16(b), $\Gamma (\equiv \hbar \omega_c - e\Delta V)$ is replotted as a function of *B*. As seen in the figure, Γ shows a rather strong dependence on ν; this result indicates that the Landau level is sharp ($\Gamma \sim 0.5$ meV) when the topmost Landau level is half-filled ($\nu = 3$, spin-unresolved), whereas it broadens as the Fermi level moves toward the gap of the Landau levels. This strong dependence of Γ on ν can be explained by the screening effect: The strength of screening is, in general, proportional to the density of states at the Fermi level, E_F. When the Fermi level lies in the middle of the Landau level, the screening is strong due to high density of delocalized electronic states at E_F, resulting in sharp Landau levels. However, as the Fermi level moves towards the gap of the Landau levels, the screening becomes
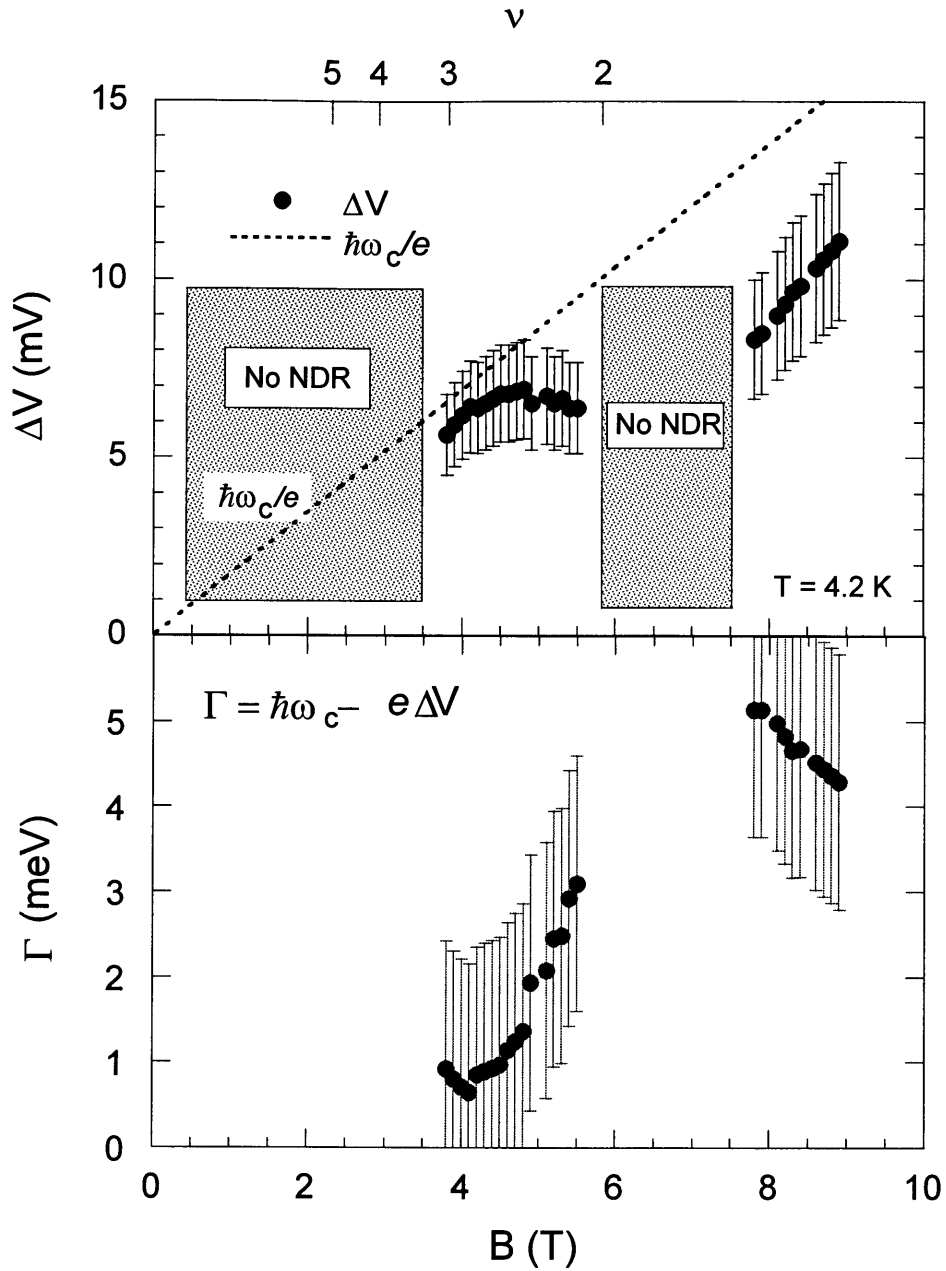
Fig. 2.16 (a) The average voltage spacing between the successive NDRs in the first plateau of I-V curves of the modulation-doped MQW diode is plotted as a function of applied magnetic field, B. The dotted line denotes the cyclotron energy, $\hbar\omega_c$. (b) The deduced Landau level broadening, $\Gamma (= \hbar\omega_c - e\Delta V)$, is plotted as a function of B.

weaker due to lower density of states as well as localization effect, leading to larger Γ. This is a clear experimental demonstration of the fact that the Landau level width strongly depends on the Landau level filling factor through the screening effect. This result is in qualitative agreement with previous theoretical predictions [39,40] and experimental results [41-45].

The advantage of the present tunneling I-V measurement is that it can determine Γ at arbitrary ν except in the vicinity of even-integer filling. It should be noted here that the Γ determined from the present tunneling experiment is not the full width of the thermodynamic density of states because localized states which are located in adjacent QWs but at in-plane distances larger than the localization length do not contribute to tunneling current. Therefore, the present Γ is considered to be intermediate between the width of the delocalized states and the thermodynamic full width of Landau levels.

2.4.6 B-field dependent supply function

Next, in order to examine above B-field dependence, we consider the I-V characteristics using a simple theoretical model for sequential resonant tunneling. Since the tunneling process is sequential, entire MQW structure can be decomposed into a series connection of coupled double QW segments. Consequently, the over all I-V characteristics of the MQW diode are governed by the "I-V characteristics of the coupled double QW segment". The theoretical tunneling current $J(\Delta V)$ between the coupled double QW segment is calculated by the product of the tunneling rate $T(\Delta V)$ and the electron supply function $S(\Delta V)$ (see for 2.3.5).

The B-field dependent $T(\Delta V)$ and $S(\Delta V)$ calculated for $B = 4.1$ T ($\nu = 3.0$) and $B = 5.8$ T ($\nu = 2.0$) are shown in Fig. 2.17. We assumed in the calculation that the level broadening $\Gamma = 0.8$ meV and the Fermi energy $E_F = 10$ meV. The peak in the tunneling rate $T(\Delta V)$ at $\Delta V = 0$ is the momentum-conserving resonant peak, while the peak at $\hbar \omega_c / e$ is due to scattering-assisted inter-Landau level tunneling. As shown in Fig. 2.17, middle
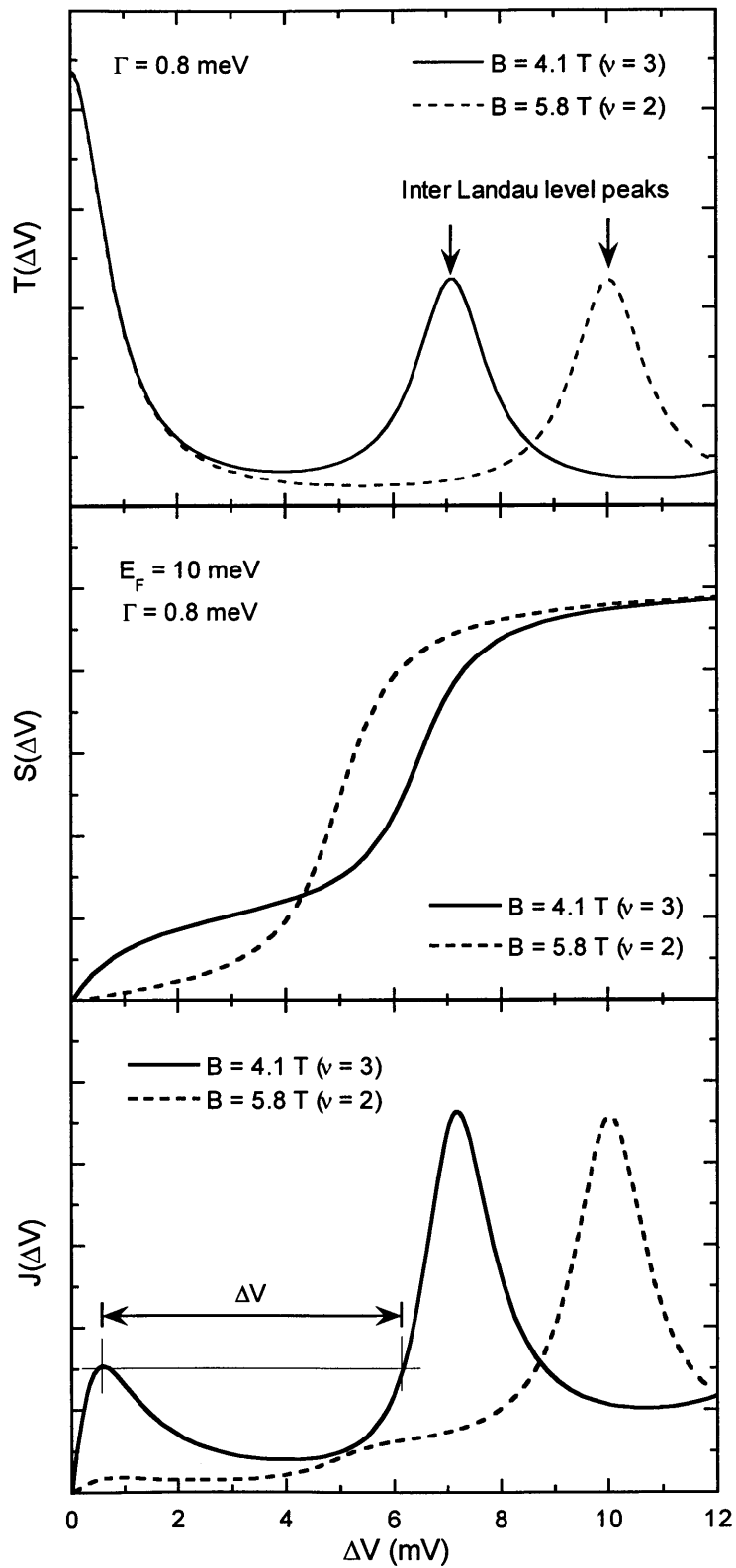
Fig. 2.17 The theoretical B-field dependent tunneling rate $T(\Delta V)$, electron supply function $S(\Delta V)$, and tunneling current $J(\Delta V)$.

part, the electron supply function $S(\Delta V)$ is strongly dependent on the Landau level filling factor v. The calculated segmental current $J(\Delta V)$ ($\equiv T(\Delta V) \cdot S(\Delta V)$) for $B = 4.1$ T has an NDR region for $B = 4.1$ T, which gives rise to periodic NDRs in the over all I-V characteristics. On the contrary, no NDR region exists in $J(\Delta V)$ for $B = 5.8$ T. In this case, it is expected that the electric field develops uniformly over the entire structure and no NDRs appear. These predictions are in good agreement with the experimentally observed I-V characteristics shown in Fig. 2.14. Furthermore, from the calculated B field dependent $J(\Delta V)$, we can predict the voltage spacings of the periodic NDRs, as shown in Fig. 2.17, bottom part. In Fig. 2.16(a), the predicted voltage spacings ΔV is plotted as a function of B. As seen in the figure, the theory explains the B-field dependence of ΔV very well.

2.4.7 Summary

In this section, we have investigated the tunneling I-V characteristics of modulation-doped GaAs/Al$_{0.3}$Ga$_{0.7}$As MQW structures under high magnetic fields B. It is found that the first plateau of the tunneling I-V characteristics of the MD-MQWs exhibits a couple of remarkable features; in particular, a strong dependence on a magnetic field, B, applied normal to the layer plane is observed. The observed NDRs are identified to be due to the scattering-assisted sequential resonant tunneling through successive Landau levels. Furthermore, the observed voltage spacings of NDRs are systematically smaller than the cyclotron energy. We have extended the theory developed by Kazarinov and Suris to a finite magnetic field case and found that all the observed features are well explained by the interplay between the scattering-assisted inter Landau-level tunneling and the B dependence of the two-dimensional electron supply function. We have also shown that the present tunneling spectroscopy allows us a unique opportunity to determine the Landau level width, Γ. The determined Γ is found to be strongly dependent on the Landau level filling factor through the screening effect.

2.5 Dynamics of high-field domain formation

2.5.1 Introduction

It is well known that the I-V characteristics due to sequential resonant tunneling through the active regions of such MQWs show plateau-like regions, each of which exhibits periodic negative differential resistances with rather constant peak and valley current. Such a behavior has been explained by the formation of high-field domain and sequential resonant tunneling through them [12-18]. Recently, the importance of the dynamics of the domain formation has been recognized and the investigation along this line has been started [46,47].

In this section, we investigate the frequency dependence of the tunneling I-V characteristics of GaAs/Al$_{0.3}$Ga$_{0.7}$As MQW sequential resonant tunneling diodes. Although clear periodic NDRs are observed in the dc measurement, such NDRs are found to disappear at high frequencies, indicating a finite time constant necessary for the formation of stable high-field domains. The observed time constant has been well explained by the product of the capacitance of a single tunneling barrier and the intrinsic tunneling resistance in the low-field domain.

2.5.2 Temporal response of I-V characteristics

The GaAs/Al$_{0.3}$Ga$_{0.7}$As MQW structure investigated in this work was grown on an n^{+}-GaAs substrate by molecular beam epitaxy (MBE). The active region of the sample consisted of 20 periods of 250 Å-wide GaAs quantum wells and 100 Å-thick Al$_{0.3}$Ga$_{0.7}$As barriers and was uniformly doped with Si up to 5×10^{15} cm^{-3}. However, the actual electron density is lower due to the compensation effect, as will be discussed later. The MQW active region was sandwiched between 0.5 μm-thick n^{+}-GaAs capping and buffer layers. The samples were etched into mesa shapes of 200×200 μm^{2} defined by standard photolithography. Tunneling I-V characteristics were measured between the top and

bottom ohmic electrodes at 4.2 K. The dc I-V characteristics were measured by using a semiconductor parameter analyzer. The time dependent tunneling current was measured by using a digital oscilloscope and an output of a function generator.

Figure 2.18 shows the dc I-V characteristics of the MQW structure and the blowup of the first plateau region. As shown in Fig. 2.18(a), the I-V characteristics consist of plateau-like regions, in each of which periodic NDRs with rather constant peak and valley current are observed. The electron transport through such a MQW structure has been attributed to the sequential resonant tunneling process between the two-dimensional (2D) subbands in the neighboring quantum wells [12-18]. The plateaus in the I-V characteristics are formed as the high-field domains grow with an external bias. The voltage differences between the successive NDRs in each plateau are approximately equal with the energy differences between the 2D subbands in the quantum well (QW). Furthermore, the I-V characteristics show large hysteresis with respect to the sweep directions. It is known that the hysteresis of the I-V characteristics is caused by the series resistance.

Figure 2.19 shows the I-V characteristics of the MQW diodes measured by using triangular voltage sweeps at various repetition frequencies f. As shown in Fig. 2.19, clear periodic NDRs due to high-field domain formation were observed up to 1 kHz. However, the amplitude of the NDRs became smaller as f was further increased, and eventually they disappeared at about $f = 50$ kHz. This fact clearly indicates that a finite time constant is necessary for the high-field domain formation. In order for static domains to be formed, non-equilibrium charge accumulation at the domain boundary is necessary to support the difference in the electric fields between in the high- and low-field domains. Such charges must be supplied through a series resistance of the structure to the tunnel barrier capacitance at the domain boundary.
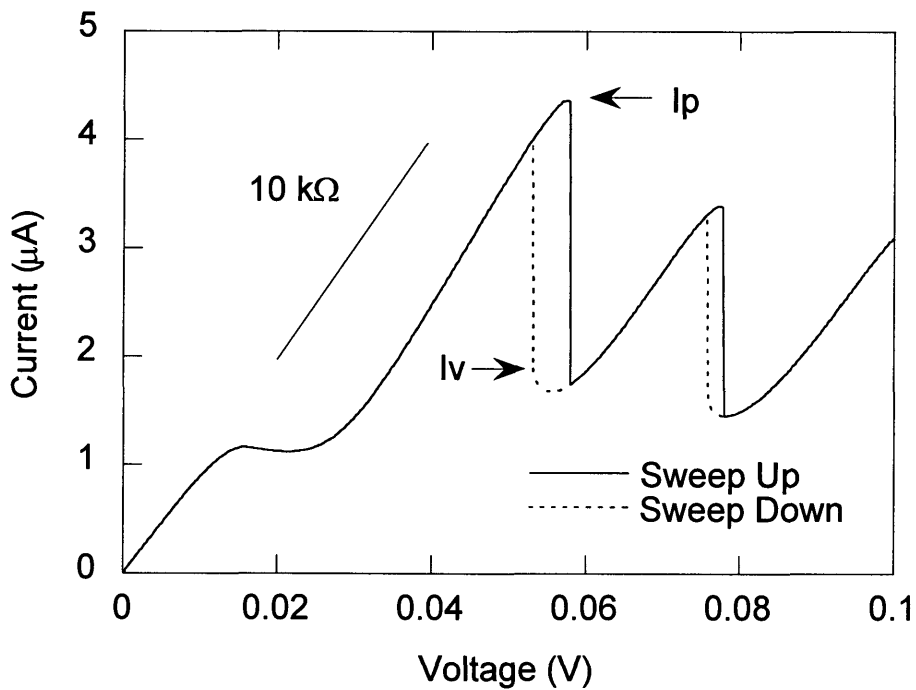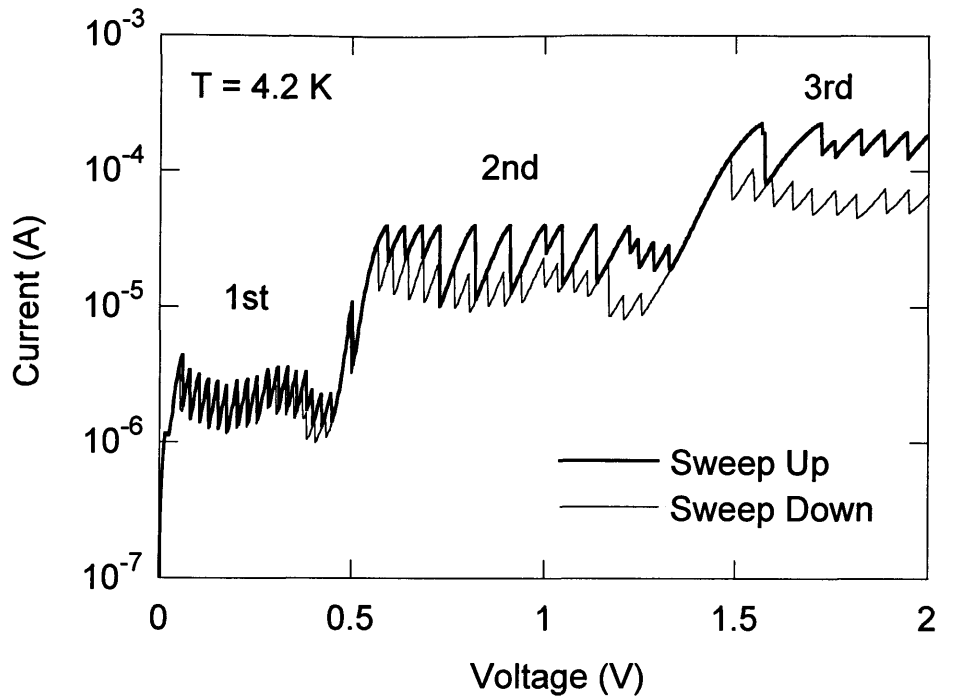
Fig. 2.18 (a) The dc I-V characteristics of a uniformly-doped GaAs/Al$_{0.3}$Ga$_{0.7}$As MQW diodes, and (b) the blowup of the I-V characteristics in the first plateau.
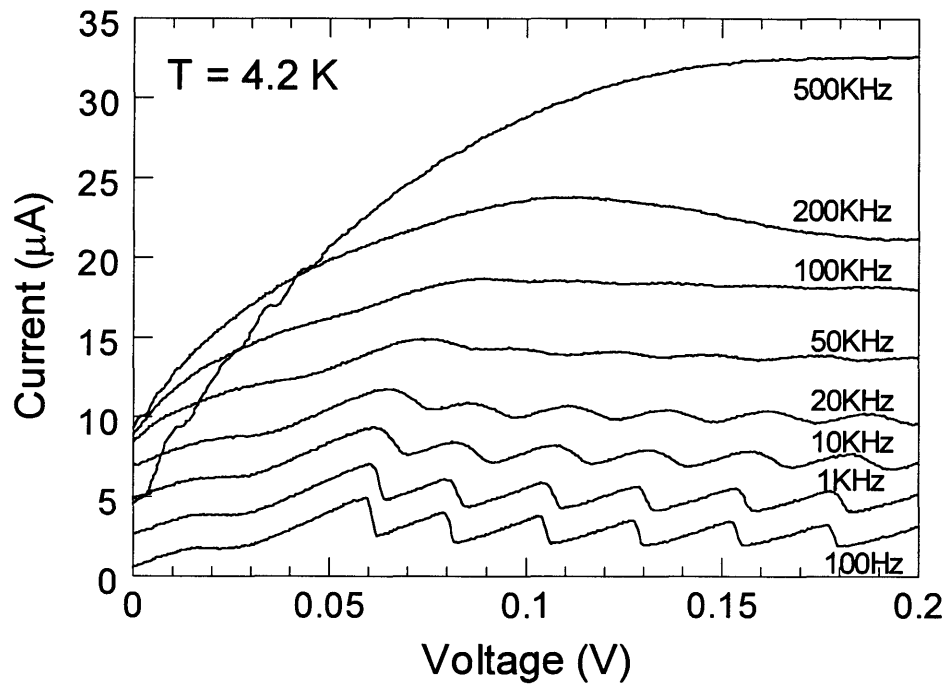
Fig. 2.19 The *I-V* characteristics of the MQW diodes measured by using triangular voltage sweeps at various frequencies.

2.5.3 Step response of I-V characteristics

In order to observe the dynamical effect more directly, we have investigated the temporal response of the *I-V* characteristics to stepped applied voltages as shown in Fig. 2.20. The stepped voltage of about 60 mV was applied to the diode so as to set the steady state *I-V* curve at the first valley in the first plateau region (see in Fig. 2.18(b)). The very initial current spike is a displacement current through the tunneling capacitance. It is found that the first, rather constant current in the range denoted as region I in Fig. 2.20(a) is equal to the resonant peak current I_P, while the steady state current in region III is equal to the nonresonant valley current I_V (see Fig. 2.18(b)). Between the regions I and III, a clear transient from the resonant state to the nonresonant state is observed (region II). We have attributed the observed 5 µs-long transient to the time necessary for accumulating charges at the domain boundary.

Similar measurements were done on the temporal responses of the *I-V* characteristics in the 2nd and 3rd plateaus. The amplitude of the applied stepped voltages were chosen to be about 0.6 V and 1.6 V for the 2nd and 3rd plateaus, respectively, so as to set the voltages at the first valley in each plateau. As seen in Fig. 2.20(b) and (c), the behavior of temporal current response for the higher plateaus is different from that for the 1st plateau; for the case of higher plateaus, a somewhat depressed current regions with small spikes (region I) appear immediately after the displacement current. The spike current in region I has been attributed to the well-to-well charge hopping for the formation of the low-field domain [46]. Then, the current is stabilized to the valley current (region III). For the 2nd plateau, the 2D-2D resonant tunneling in the low-field domain occurs from the ground subband (E_0) to the first excited subband (E_1), while the tunneling in the high-field domain occurs between the ground subband and the second excited subband (E_2). The behavior shown in Fig. 2.20(b) suggests that the high-field domain ($E_0 \rightarrow E_2$) is formed after the formation of the low-field domain ($E_0 \rightarrow E_1$) is finished. The length of the current transient (approximately 1 µs) denoted as region II in Fig. 2.19(b) is considered
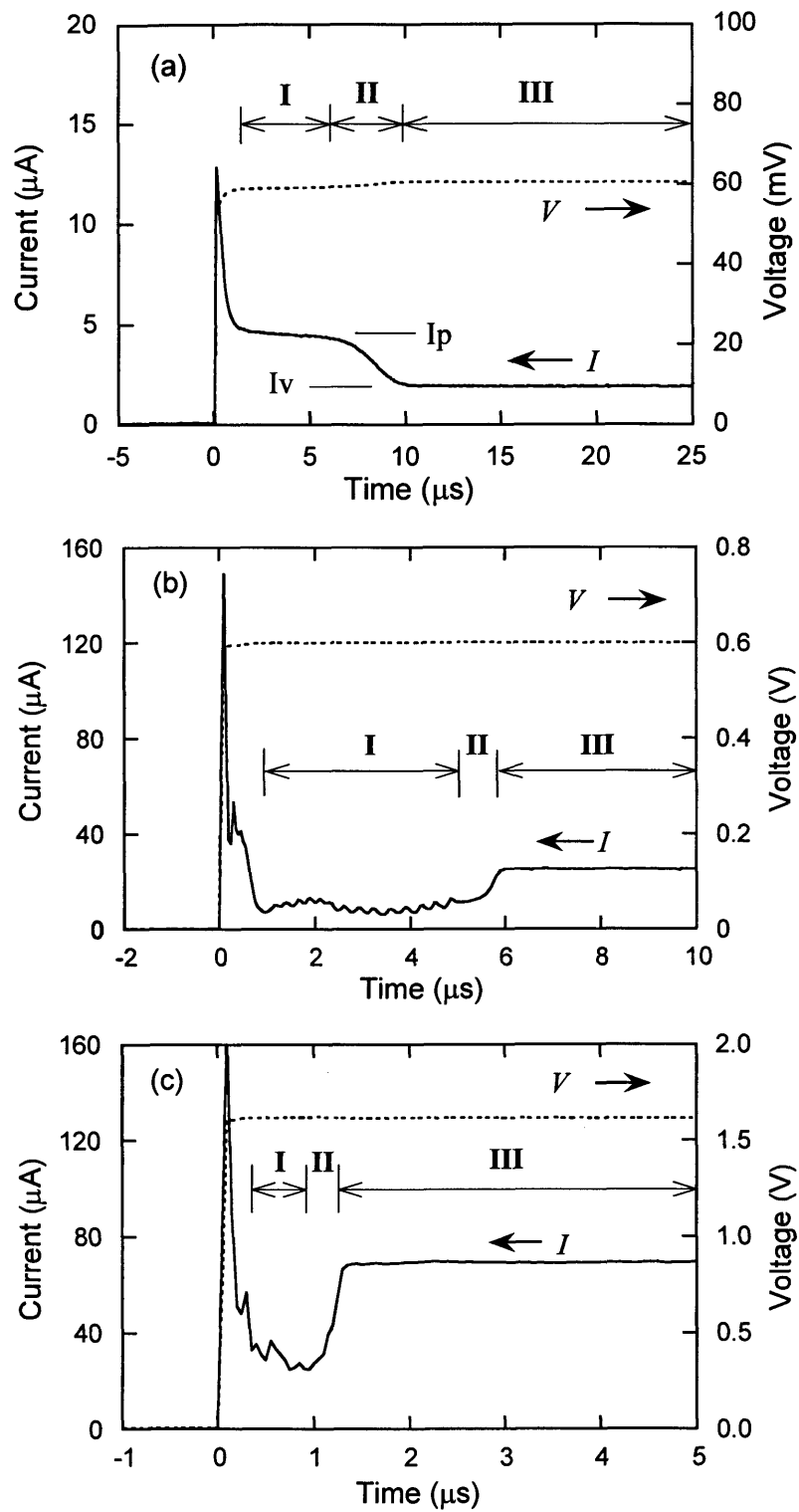
Fig. 2.20   The temporal response of the tunneling current (solid line) to a stepped applied voltage (dotted line) for the 1st (a), 2nd (b) and 3rd plateaus (c).

to be the time constant for the high-field domain formation in the 2nd plateau. A similar behavior is observed also for the 3rd plateau, as shown in Fig. 2.20(c). The time constant for the domain formation in the 3rd plateau is estimated to be about 0.3 μs.

2.5.4 Time constant for high-field domain formation

First, let us consider the time constants for the domain formation phenomenologically. The charges necessary to support the difference in electric fields between in the low- and high-field domains are accumulated through a series resistance R_S to the tunneling capacitance C_T at the domain boundary. The R_S in the 1st plateau was determined to be about 10 kΩ from the differential conductance of the measured dc I-V characteristics shown in Fig. 2.18(b). The R_S's for the 2nd and 3rd plateaus were also determined to be about 1.8 kΩ and 0.7 kΩ, respectively. The capacitance of a single tunneling barrier C_T was calculated to be about 500 pF from the barrier thickness and the device size. By multiplying R_S's and C_T, the time constants τ_{CR} were estimated to be about 5 μs, 0.9 μs, and 0.35 μs for the 1st, 2nd, and 3rd plateaus, respectively, which are in good agreement with the experimental results shown in Fig. 2.20.

Then, the next question is what is the origin of the series resistance R_S. Since R_S changes by more than one order of magnitude for different current plateaus, R_S is considered to originate from the MQW structure itself. In order to estimate R_S quantitatively, we have calculated the tunneling current based on a density matrix approach [23,24]. Since electrons tunnel from one QW to the next sequentially, the entire MQW structure can be decomposed into a series connection of coupled double QW segments. Consequently, the overall I-V characteristics of the MQW diode is governed by the I-V characteristics of the coupled double QW segment, although such segmental I-V characteristics are not measurable. We have calculated the segmental I-V characteristics by Eqs. (2.1) – (2.3) developed by Kazarinov and Suris as [23,24]. Figure 2.21(a) shows the calculated segmental I-V characteristics , J, for the present QW structure. In the
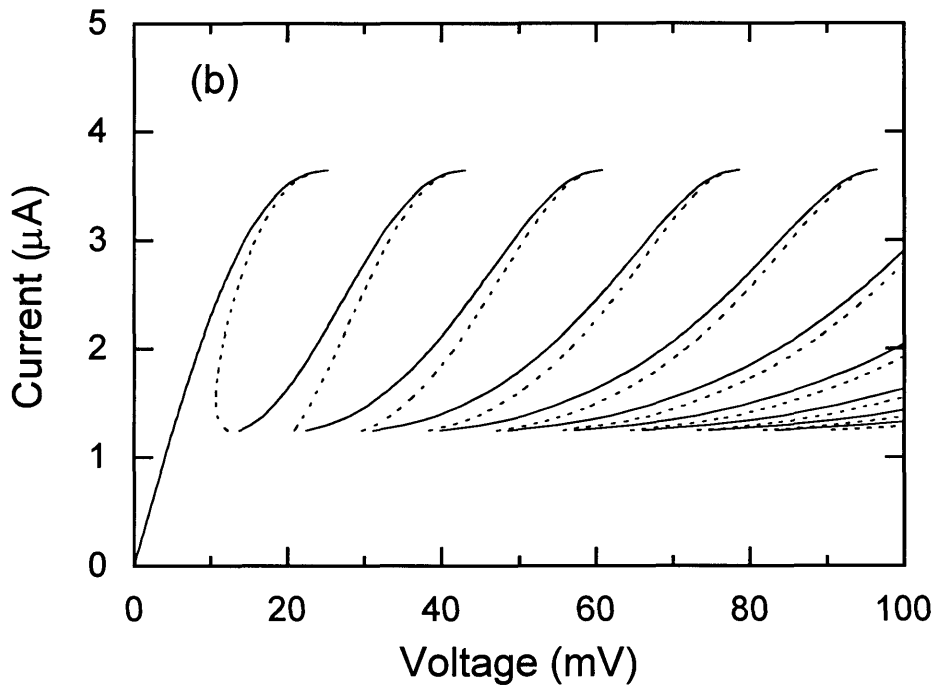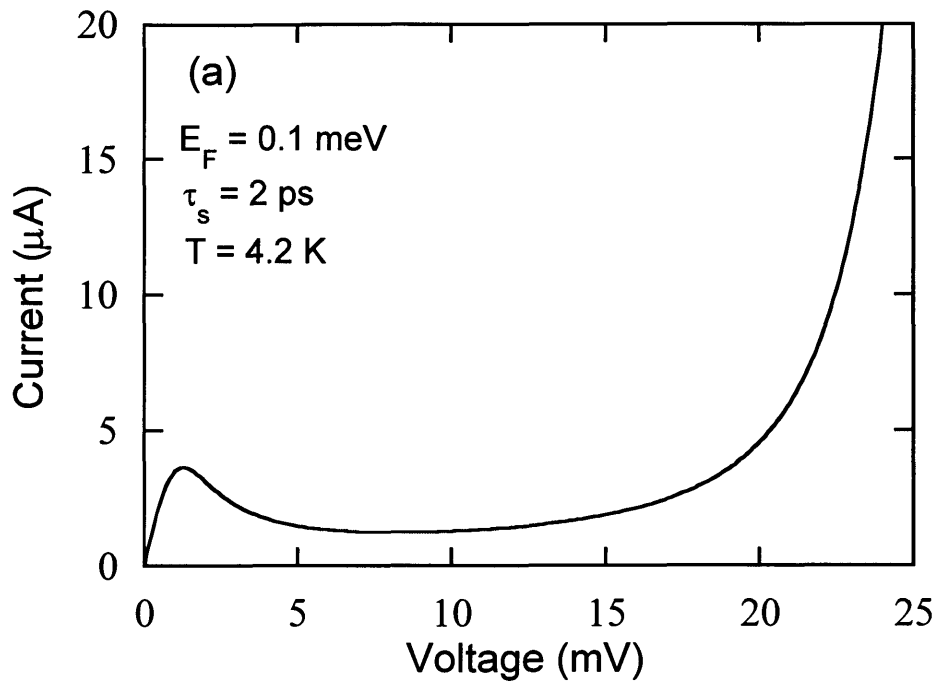
Fig. 2.21 (a) The calculated segmental *I-V* characteristics, and (b) the result of simulated overall *I-V* characteristics in the 1st plateau. The unstable negative-differential-resistance regions are shown by dashed curves.

calculation, the electron Fermi energy E_F and the scattering time τ_s were used as fitting parameter. The detail of the calculation was discussed in the section 2.3 [48]. As seen in Fig. 2.21(a), the segmental I-V characteristics show a clear NDR. When such segments are connected in series and a bias voltage is applied to the entire MQW structure, two stable field states become possible due to the current continuity condition, leading to a formation of high-field domains and the appearance of periodic NDRs in the overall I-V characteristics. The result of such simulation of I-V characteristics in the 1st plateau are shown in Fig. 2.21(b). The tunneling resistances in the low-field domain determined from the theoretical I-V curves are about 5 kΩ, 1.7 kΩ, and 0.3 kΩ for the 1st, 2nd, and 3rd plateau, respectively. These values are in good agreement with the series resistances determined from the experimental I-V curves. The theory well reproduces not only the magnitude of R_S but also the dependence of R_S in each plateau. This fact clearly indicates that the dominant series resistance in the MQW structure is not due to an extrinsic factor such as contact resistances but due to the intrinsic tunneling resistance in the low-field domain.

2.5.5 Summary

In this section, we have investigated the frequency and temporal dependence of the tunneling I-V characteristics of GaAs/Al$_{0.3}$Ga$_{0.7}$As MQW sequential resonant tunneling diodes. The I-V characteristics show remarkable frequency dependences; i.e., the formation of high-field domains is not able to follow the high frequency applied electric fields. Furthermore, the temporal response of the tunneling current to a stepped voltage clearly exhibits a finite transient from the peak to valley current. It is found that such a finite time constant necessary to form high-field domains is well explained by the product of the capacitance of a tunneling barrier and the intrinsic tunneling resistance in the low-field domain.

2.6 Summary of Chapter II

In this chapter, we discussed our work in the area of perpendicular transport in MQW. In the second section, we discussed the sequential resonant tunneling with high-field domain formation leading to a hysteresis in the I-V characteristics, which is connected with a multistability of the current.

In the third section, we have investigated the tunneling I-V characteristics of $Al_{0.3}Ga_{0.7}As/GaAs$ MQW diodes with various electron densities, N_s, and scattering rates, Γ. Clear periodic NDRs are observed for the samples with low N_s and Γ, while no NDRs are observed in the *first* plateau region of the I-V characteristics of the samples with high N_S and Γ. We have shown that such formation/destruction of the high-field domains in MQW diodes is controlled by the interplay of the tunneling rate and the electron supply-functions between the adjacent coupled QWs. The technological implication of the present result is that by carefully designing the structure and the doping level of MQW diodes it is possible to apply uniform electric field throughout the MQW structure, which would be suitable for realizing novel THz emission/detection devices.

In the fourth section, we have investigated the tunneling I-V characteristics of modulation-doped $GaAs/Al_{0.3}Ga_{0.7}As$ MQW structures under high magnetic fields B. It is found that the first plateau of the tunneling I-V characteristics of the MD-MQWs exhibits a couple of remarkable features; in particular, a strong dependence on a magnetic field, B, applied normal to the layer plane is observed. The observed NDRs are identified to be due to the scattering-assisted sequential resonant tunneling through successive Landau levels. Furthermore, the observed voltage spacings of NDRs are systematically smaller than the cyclotron energy. We have extended the theory developed by Kazarinov and Suris to a finite magnetic field case and found that all the observed features are well explained by the interplay between the scattering-assisted inter Landau-level tunneling and the B dependence of the two-dimensional electron supply function. We have also shown that the present tunneling spectroscopy allows us a unique opportunity to determine the

Landau level width, Γ. The determined Γ is found to be strongly dependent on the Landau level filling factor through the screening effect.

In the fifth section, we have investigated the frequency and temporal dependence of the tunneling I-V characteristics of GaAs/Al$_{0.3}$Ga$_{0.7}$As MQW sequential resonant tunneling diodes. The I-V characteristics show remarkable frequency dependences; i.e., the formation of high-field domains is not able to follow the high frequency applied electric fields. Furthermore, the temporal response of the tunneling current to a stepped voltage clearly exhibits a finite transient from the peak to valley current. It is found that such a finite time constant necessary to form high-field domains is well explained by the product of the capacitance of a tunneling barrier and the intrinsic tunneling resistance in the low-field domain.

Bibliography

[1] L. Esaki and R. Tsu, IBM J. Res. Dev. **14**, 61 (1970).

[2] R. F. Kazarinov and R. A. Suris, Sov. Phys. Semicond. **5**, 707 (1971).

[3] R. Tsu and L. Esaki, Appl. Phys. Lett. **22**, 562 (1973).

[4] L. Esaki and L. L. Chang, Phys. Rev. Lett. **33**, 495 (1974).

[5] G. H. Dohler, R. Tsu, and L. Esaki, Solid State Commun. **17**, 317 (1975).

[6] R. Tsu and G Dohler, Phys. Rev. B **12**, 680 (1975).

[7] R. Tsu, L. L. Chang, G. A. Sai-Halasz, and L. Esaki, Phys. Rev. Lett. **34**, 1509 (1975).

[8] E. A. Rezek, N. Holonyak, B. A. Vojak, and H. Shichijo, Appl. Phys. Lett. **31**, 703 (1977).

[9] B. A. Vojak, N. Holonyak, R. Chin, E. A. Rezek, R. D. Dupuis, and P. D. Dapkus, J. Appl. Phys. **50**, 5835 (1979).

[10] S. Luryi, Appl. Phys. Lett. **47**, 490 (1985).

[11] A. D. Stone and P. A. Lee, Phys. Rev. Lett. **54**, 1196 (1985).

[12] L. Esaki and L. L. Chang, Phys. Rev. Lett. **33**, 495 (1974).

[13] K. K. Choi, B. F. Levine, R. J. Malik, J. Walker, and C. G. Bethea, Phys. Rev. B**35**, 4172 (1987).

[14] K. K. Choi, B. F. Levine, N. Jarosik, J. Walker, and R. Malik, Phys. Rev. B**38**, 12362 (1988).

[15] T. H. H. Vuong, D. C. Tsui, and W. T. Tsang, J. Appl. Phys. **66**, 3688 (1989).

[16] Y. Kawamura, H. Asahi, and K. Wakita, Jpn. J. Appl. Phys. **28**, L1104 (1989).

[17] H. T. Grahn, H. Schneider, and K. von Klitzing, Phys. Rev. B**41**, 2890 (1990).

[18] H. T. Grahn, R. J. Haug, W. Müller, and K. Ploog, Phys. Rev. Lett. **67**, 1618 (1991).

[19] V. J. Goldman, D. C. Tui, and J. E. Cunningham, Phys. Rev. Lett. **58**, 1256 (1987).

[20] Y. Kawamura, K. Wakita, K. Oe, Jpn. J. Appl. Phys. **26**, L1603 (1987).

[21] B. Laikhtman, Phys. Rev. B **44**, 11260 (1991).

[22] J. Kastrup, H. T. Grhan, K. Ploog, F. Prengel, A. Wacker, and E. Schöll, Appl. Phys.

Lett. **65**, 1808 (1994).

[23] R. F. Kazarinov and R. A. Suris: Sov. Phys. -Semicond. **6** (1972) 120.

[24] F. Capasso, K. Mohammed, and A. Y. Cho, IEEE J. Quantum Electron. **QE-22**, 1853 (1986).

[25] Since the exact values of N_S in each QW were not known, we simply assumed in the calculation that all the doped Si donors were activated in the samples and estimated N_S. Small errors in the estimation of N_S are not critical to the overall conclusions.

[26] Γ was determined by measuring the Shubnikov-de Haas-like oscillatory magnetotunneling resistances of the samples at zero bias voltage; E. E. Mendez, H. Ohno, L. Esaki, and W. I. Wang, Phys. Rev. B**43**, 5196 (1991).

[27] C. Waschke, H. G. Roskos, R. Schwedler, K. Leo, and H. Kurz., Phys. Rev. Lett. **70**, 3319 (1993).

[28] R. Bratschitsch, R. Kersting, T. Müller, G. Strasser, K. Unterrainer, W. Fischler, and R. A. Höpfel, Physca B. **272**, 375 (1999).

[29] G. Brozak, M. Helm, F. DeRosa, C. H. Perry, M. Koza, R. Bhat, and S. J. Allen, Phys. Rev. Lett. **64**, 3163 (1990).

[30] T. Dekorsy, R. Ott, H. Kurz and K. Köhler 1995 Phys. Rev. B. **51**, 17275 (1995).

[31] B. F. Levine, J. Appl. Phys. **74**, R1 (1993).

[32] J. Faist, F. Capasso, D. L. Sivco, C. Sirtori, A. L. Hutchinson, and A. Y. Cho, Science **264**, 553 (1994).

[33] J. Faist, F. Capasso, C. Sirtori, D. Sivco, A. L. Hutchinson, S. N. G. Chu, and A. Y. Cho, Appl. Phys. Lett. **64**, 1144 (1994).

[34] P. S. S. Guimaraes, B. Keay, J. P. Kaminski, S. J. Allen, Jr., P. F. Hopkins, A. C. Gossard, L. T. Flores, and J. P. Harbison, Phys. Rev. Lett. **70**, 3792 (1993).

[35] B. F. Levine, K. K. Choi, C. G. Bethea, J. Walker, and R. J. Malik, Appl. Phys. Lett. **50**, 1092 (1987).

[36] M. Helm, P. England, E. Colas, F. DeRosa, and S. J. Allen Jr., Phys. Rev. Lett. **63**, 74 (1989).

[37] H. T. Grahn (private communication); recently, Grahn et al. have investigated *I-V* characteristics of a lightly doped MQW diode structure and observed current instability when clear NDRs are not observed in plateau-like regions of *I-V* characteristics. They have attributed it to the formation of *dc* unstable high-field domains. However, we did not observe such current instability in our highly doped MD-MQW diodes.

[38] Y. Shimada and K. Hirakawa, Jpn. J. Appl. Phys. **36**, 1012 (1997).

[39] T. Ando and Y. Murayama, J. Phys. Soc. Jpn. **54**, 1519 (1985).

[40] S. Das Sarma and X. C. Xie, Phys. Rev. Lett. **61**, 738 (1988).

[41] E. Gornik, R. Lassnig, G. Strasser, H. L. Stormer, A. C. Gossard, and W. Wiegmann, Phys. Rev. Lett. **54**, 1820 (1985).

[42] J. P. Eisenstein, H. L. Stormer, V. Narayanamurti, A. Y. Cho, A. C. Gossard, and C. W. Tu, Phys. Rev. Lett. **55**, 875 (1985)

[43] D. Weiss, E. Stahl, G. Weimann, K. Ploog, and K. von Klitzing, Surf. Sci. **170**, 285 (1986).

[44] Th. Englert, J. C. Maan, Ch. Uihelein, D. C. Tsui, and A. C. Gossard, Solid State Commun. **46**, 545 (1983).

[45] M. Helm: Semicond. Sci. Technol. **10** (1995) 557.

[46] J. Kastrup, F. Prengel, H. T. Grahn, K. Ploog, and E. Scholl: Phys. Rev. **B53** (1996) 1502.

[47] D. Bertram, R. Klann, H. T. Grahn, K. von Klitzing, and K. Eberl: Appl. Phys. Lett. **68** (1996) 2921.

[48] Y. Shimada and K. Hirakawa: Jpn. J. Appl. Phys. **36**, 1944 (1997).

Chapter III
Terahertz carrier dynamics and Bloch gain in superlattices

3.1 Introduction

Bloch oscillation (BO) in semiconductor superlattices is attractive as a source of coherent THz electromagnetic waves, because the frequency of the radiation can be tuned in the THz range by *dc* bias fields. Since the first proposal of high frequency Bloch oscillators by Esaki and Tsu [1], considerable effort from both experiments [2-10] and theories [11-15] has been made to search for BOs and obtain terahertz (THz) device. Even after three decades from the proposal, however, THz devices using BOs have not been realized yet. It is, therefore, of prime importance to establish an understanding of the dynamical electron motion in the THz regime.

In recent years, a new technique that measures the THz electromagnetic wave emitted by ultrafast transient electron motions has been established (time-resolved THz emission spectroscopy) [16-18]. Ultrafast time-domain experiments on high quality samples unambiguously demonstrate that electrons in superlattice minibands perform at least a few cycle Bloch oscillations [8,9]. However, the idea of Bloch oscillator was challenged in a more fundamental way by asking whether BO is useful in generating/amplifying electromagnetic (EM) waves. When an electric field is applied to an ideal SL, the miniband is split into equally spaced Wannier-Stark (WS) ladder states with an energy separation of $\hbar\omega_B$ (ω_B the Bloch frequency and $\hbar$ the reduced Planck constant). Since the emission and absorption of EM waves take place between the adjacent two WS levels, they occur at the same frequency and, hence, cancel each other. Consequently, an ideal SL has no net gain or loss for EM waves. However, when scattering exists in the system, new transition channels, i.e., scattering-assisted transitions,

become available. The direct experimental proof of such THz gain is to show that the real part of the carrier conductivity, becomes negative in the THz range.

In this chapter, we present a strong experimental support for the THz gain due to Bloch oscillating electrons in wide miniband GaAs/Al$_{0.3}$Ga$_{0.7}$As SLs. For determining the high-frequency electron conductivity in SL minibands, we took a totally different approach; we used undoped SL samples in order to avoid large current density and high-field domain formation, and took all the necessary information within a few ps, by noting that the time-domain THz spectroscopy inherently measures the step-response of the electron system to the applied bias electric field and that the Fourier spectra of the THz emission is closely related with the carrier conductivity. Quasi-autocorrelation measurements were performed on the emitted THz electromagnetic wave. It is also found that Zener tunneling into the second miniband sets the high-frequency limit of the THz gain for the samples studied here.

In the second section, a background of Bloch oscillations in semiconductor SLs is given. Then, the sample structure of SLs investigated in this study, their optical properties, and an experimental setup of time-resolved THz emission spectroscopy are shown in the third section. An observation of THz emission due to Bloch oscillation at room temperature by using the THz emission spectroscopy is described in fourth section. Furthermore, THz conductivity and possible Bloch gain are discussed in the fifth section. Finally, an inter-miniband resonant Zener tunneling in the SLs is investigated in the sixth section.

3.2 Bloch oscillation in semiconductor superlattice

3.2.1 Bloch oscillation and Wannier-Stark ladder

The standard picture of electronic transport in solids under a static field is drift transport as first considered in detail by Drude [21]; carriers move ballistically until they

change their momentum by a scattering process. The drift velocity of the carriers is determined by a balance between the momentum and energy gain from the field during ballistic motion and by the momentum and energy changes due to elastic and inelastic scattering processes. The overall current due to the moving carriers is then characterized by Ohm's law

$$j = \sigma E \tag{3.1}$$

The conductivity σ in the Drude picture is given by

$$\sigma = \frac{e^2 n \tau}{m} \tag{3.2}$$

where τ is the momentum relaxation time , n the carrier density and m the carrier mass.

One of the central assumptions of the Drude picture is that the carrier move ballistically between scattering events. A description as free carriers is justified if the carriers stay close to the lower band edge. However, if the fields are high enough that the carriers reach higher parts of the bands before they are scattered, the electrons do not behave like free carriers anymore; if the scattering rate is low enough, they start to oscillate. This fact follows directly from the properties of the electronic band structure of a crystalline solid under the influence of a static electric field; Bloch has shown [22] in 1928 that an electron in a periodic potential subject to an external electric field F changes its k-vector according to

$$\hbar \frac{dk}{dt} = eF \tag{3.3}$$

Since the band structure is periodic in k, it is immediately obvious (as pointed out by Zener [23]) that an electron which is not subject to scattering processes will perform an oscillatory motion in energy. This oscillatory motion in energy is accompanied by a periodic motion in real space, the so-called Bloch oscillations (BOs). The time period of the motion is given by

$$\tau_B = \frac{2\pi\hbar}{eFd} \tag{3.4}$$

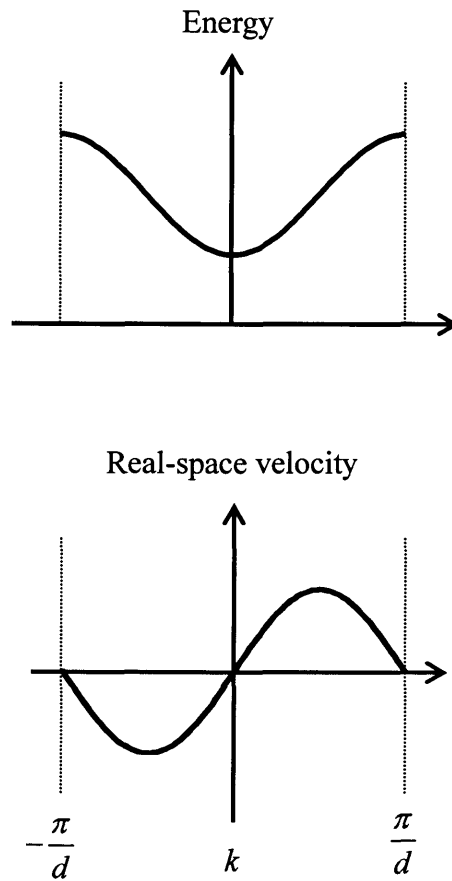Fig. 3.1 Bloch oscillations in the semi-classical picture. An electron at k = 0 starts to move with constant velocity in k-space once the field is turned on. Until the edge of the first Brillouin zone, it gains energy. When it leaves the first Brillouin zone, the energy starts to decrease and the velocity becomes negative. When it reaches the center of the second Brillouin zone, it has returned to its original spatial position.

(with d as the period of the lattice) and the total spatial extension (from left to right maximum of the oscillation displacement) by

$$L = \frac{W}{eF}$$
(3.5)

where W is the width of the band. Figure 3.1 shows a scheme of the first Brillouin zone of a crystalline solid with the energy of electron E (upper panel) and its real space velocity v_R (lower panel) given by

$$v_R = \frac{1}{\hbar}\frac{\partial E}{\partial k}$$
(3.6)

In the first half of its cycle, the electron moves with the field and gains energy from the field; in the second half, it moves against the field and loses energy to it. The periodic motion can also be understood as a Bragg reflection of the accelerated electron once its wavelength reaches the lattice period. It is interesting to note that the phenomenon of Bloch oscillations is rather independent of the details of the band structure: the equation given for amplitude and period are generally valid.

The criterion which divides Drude drift transport from Bloch oscillations is the ratio of the scattering time τ to the BO period τ_B: only if τ is large compared to τ_B will the oscillations occur. The observation of BOs thus requires high field and/or long scattering times.

The effect of a static field on a periodic band structure can as well be discussed in a real space picture: the eigenstates of the lattice without field are the well known Bloch functions which are infinitely extended. Once a field is applied, the wave functions become localized with a localization length L which is identical to that given in (3.5). The energy spectrum of the lattice subject to an electric field is no longer a continuous band, but consists [24] of the so-called Wannier-Stark ladder (WSL) with energies

$$E = E_0 + n\Delta E$$
(3.7)

where ΔE is the ladder spacing given by

$$\Delta E = eFd$$
(3.8)

n is an integer and E_0 is the energy of a particular reference state.

Similar to their time domain counterpart, the observation of the Wannier-Stark ladder requires certain conditions. The wave functions at a zero field are in a real system not completely delocalized, but have a certain coherence length which depends on the scattering processes the electronic states are subject to. The Wannier-Stark localization can occur if the field localization length L is smaller than the scattering localization length. It is obvious that this criterion is equivalent to the condition that the scattering time is longer than the BO period.

3.2.2 Experimental observation of Bloch oscillation

For many years, it has been controversially debated whether Bloch oscillations and the Wannier-Stark ladder exist. In the center of a theoretical debate about the existence of the Wannier-Stark ladder was the question whether field localization and the observation of the ladder would be prevented by coupling to higher bands and continuum: the ladder states are not stationary, since scattering to higher bands and continuum can take place. The debate whether coupling to higher states prevents the existence of the WSL has seemingly been settled with the result that the coupling to other states in under certain conditions weak enough to preserve the ladder structure. The experimental observations of the WSL and BO as discussed in this section have naturally confirmed this result.

Similarly, the experimental observability of BOs has been debated for many years. The main obstacle to the observation of BOs in bulk solids is that the electron has to gain a large amount of energy (a few eV in most solids) to be reflected. At such high energies, the relaxation by scattering processes is very fast, making the completion of a full oscillation period unlikely. If the electron is scattered long before it reaches the edge of Brillouin zone, it stays at small k-vectors and moves always into the field direction, *i.e.* it is subject to standard drift transport.

A dramatic improvement for the observation of BO came with the invention of the

semiconductor superlattice by Esaki and Tsu in the early 1970s [1]. By the alternating growth of semiconductor layers with larger and smaller band gap, a superlattice is created in the growth (z-) direction. If the barrier layers are sufficiently thin, the coupling between the electronic states in the wells leads to the formation of a so-called miniband in the z-direction. Typical band widths are of the order of 20-200 meV. The much smaller band widths compared with those in bulk semiconductors allow to perform experiments at much lower fields. Related is the fact that the electrons need to reach much lower energies than in conventional solids to get to the upper part of the band, thus reducing the scattering probability with, *e.g.* optical phonons. The experimental realization of semiconductor superlattices enabled immediately a number of experiments which demonstrated the influence of the novel electronic states on transport or optical properties [25-27]. However, in all of the transport experiments, the observed experimental parameters were determined for the ensemble average, and the oscillation of individual electrons was averaged out. For a direct observation of the oscillations, it is necessary to create a carrier ensemble with defined phase relations.

The recent advantages in ultrafast laser technology have made it possible to create electronic excitation in atoms, molecules and solids with well defined phase. By excitation with short laser pulses, wave packet states with defined relative phase can be created. First experiments which showed wave packet dynamics were using superpositions of electronic states without particular spatial dynamics, like quantum beats between light-hole and heavy-hole excitations in quantum wells.

The first experiments which demonstrated spatial dynamics of wave packets in solids were observing coherent oscillations of electrons in double quantum wells [28]. In these experiments, a localized wave function is created in one of the wells by superposition of the symmetric and antisymmetric wave function. This wave packet oscillates between the wells with a frequency given by the energy difference between the two states. It was shown by Roskos *et al.* [17] that the oscillation of the wave packet leads to emission of THz radiation.

Recently, Bloch oscillations were directly observed by ultrafast optical techniques. In these experiments, a localized wave packet is created in a biased semiconductor superlattice. This wave packet performs spatial oscillations with the period given by (3.4). For the detection of Bloch wave packet motion, a number of experimental techniques have been used: the first experiments [3,4] and time-resolved transmission spectroscopy [29] were employed. The purpose of this study is to discuss THz emission due to Bloch oscillation and their physics.

3.3 Experimental setup of terahertz emission spectroscopy

3.3.1 Sample structures

The samples used in this section are $GaAs/Al_{0.3}Ga_{0.7}As$ superlattice m-i-n (metal-intrinsic-n^+-type) diode structures. The samples were prepared by growing 500 nm-thick undoped $GaAs/Al_{0.3}Ga_{0.7}As$ superlattice layers on n^+-GaAs substrates by molecular beam epitaxy. We designed the GaAs wells (6.4 nm) and $Al_{0.3}Ga_{0.7}As$ barriers (0.56 nm) so as to set the first miniband width Δ_1 to be 100 meV. The second miniband is separated by a 40 meV-wide minigap. The top contact was formed by depositing a semi-transparent 4 nm-thick NiCr Schottky film and the bottom ohmic contact was formed by alloying AuGeNi/Au. When a femtosecond laser pulse excites the sample, electron-hole pairs are optically created in the miniband. Due to an applied electric field, F, the carriers start drifting and THz electromagnetic wave that is proportional to the carrier acceleration is emitted into free space. Since the miniband width for heavy holes is 2.5 meV, which is much narrower than that for electrons, heavy holes are considered to be almost localized. Furthermore, absorption due to light holes is 1/3 of that due to heavy holes. Consequently, the motion of electrons dominates the emitted THz signal.
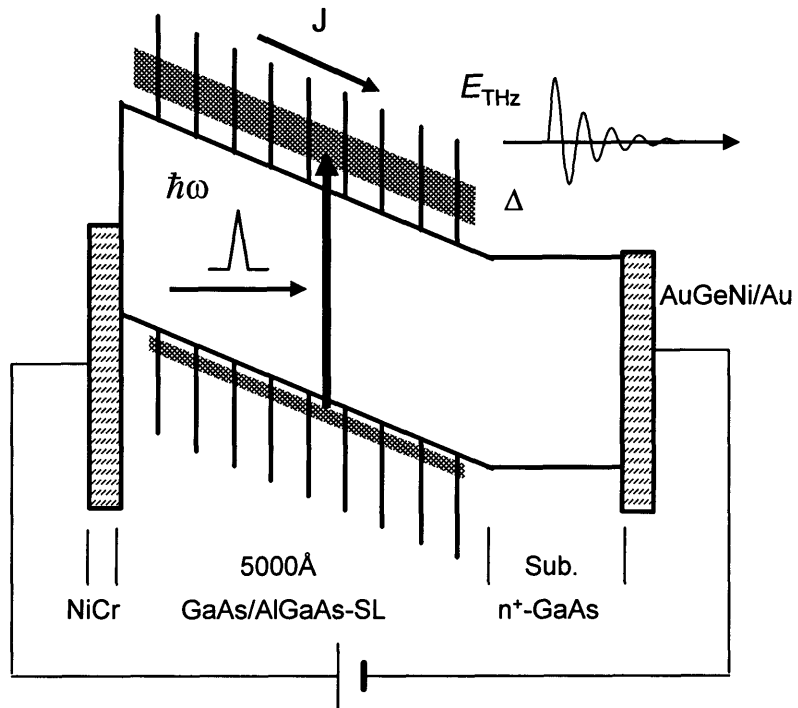
Fig. 3.2 Schematic illustration of the band diagram of a GaAs/Al$_{0.3}$Ga$_{0.7}$As m-i-n superlattice diode.

3.3.2 Photocurrent spectra of SLs

To verify the formation of miniband and the WS ladder in our sample, we have taken low-excitation photocurrent spectra at $T = 10$ K shown as Fig. 3.3. The photocurrent spectra have been differentiated with respect to the energy in order to improve the visibility of weak transitions. The spectra show rich structures at $T = 10$ K, which originate from a formation of the WS ladder. For low applied bias voltage, the spectra are weakly structured. At higher electric fields, each line fans out into a series of discrete transitions as expected for a WS ladder. Six ladder levels are clearly seen in the figure, indicating a good quality of the sample. It is also found that the miniband is formed in an energy range from 1.53 eV (810 nm) to 1.63 eV (760 nm) at $T = 10$ K.

3.3.3 Time-resolved THz emission spectroscopy

For time-resolved THz spectroscopy, we used a quasi-autocorrelation geometry [17], *i. e.*, the power of THz radiation generated by a pair of time-correlated femtosecond (fs) laser pulses was measured as a function of the time interval, τ, between the two laser pulses imposed by a Michelson interferometer. Experiments were performed by using 100 fs laser pulses delivered from a mode-locked Ti:Sapphire laser operated at a repetition rate of 76 MHz. The laser pulses were loosely focused ($\phi = 1$ mm) onto the sample surface at a polar angle of 70° in reflection geometry by a gold-coated off-axis parabolic mirror with a 60 cm effective focal length. In a loosely focused condition, the mechanism of the THz emission is dominated by acceleration/deceleration of photoexcited carriers in the superlattice miniband. A typical pump power used in the experiment was 10 mW. In this way, the carrier densities excited in the active region can be kept as low as 2×10^{14} cm^{-3} to avoid field screening and the average current density was about 0.1 A/cm^2. The generated THz emission was collimated by off-axis parabolic mirrors and focused onto a Si bolometer operated at 4.2 K. The optics and the sample were kept in an enclosure purged with nitrogen to minimize the absorption by atmospheric moisture. In our
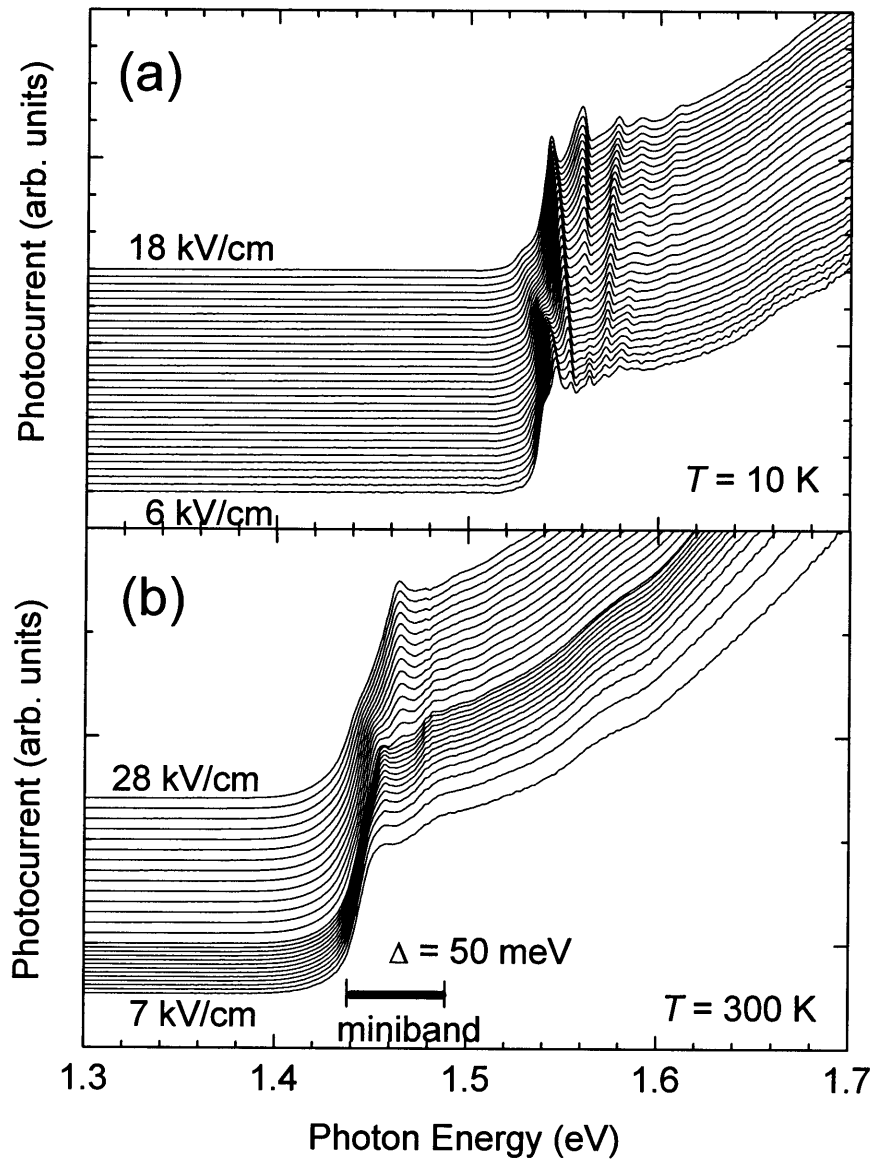
Fig. 3.3　Photocurrent spectra measured for various applied voltages at (a) T = 10 K and (b) T = 300 K.

quasi-autocorrelation measurements the detected signal intensity is a time-integrated power of the THz electric fields consecutively emitted from the sample. The signal was recorded by using a standard lock-in technique at a modulation frequency of about 400 Hz.

3.4 Terahertz emission due to electron transport in superlattices

3.4.1 Introduction

In this section, we investigate a direct observation of THz emission due to miniband transport of electrons in wide miniband GaAs/Al$_{0.3}$Ga$_{0.7}$As superlattice m-i-n (metal-intrinsic-n-type) diodes by time-resolved THz spectroscopy. Quasi-autocorrelation measurements are performed on the emitted THz electromagnetic wave by using a bolometer as a wideband detector. We have found that the THz emission due to miniband transport is strongly dependent on the photon energy of the pump laser pulses. Clear oscillations in the THz autocorrelation signal has been observed by exciting the sample at a photon energy which is close to the center of the Wannier-Stark ladder. Furthermore, transient velocities of electrons in the miniband have been estimated by fitting the measured THz autocorrelation signal. The bias-field dependence of the emitted THz radiation intensity clearly showed a crossover from the miniband transport to the formation of Wannier-Stark ladder (WSL). In the Wannier-Stark regime, a few cycle BO were observed even at 300 K in a superlattice whose miniband width is greater than the Longitudinal Optical (LO) phonon energy.

3.4.2 THz emission due to Bloch oscillations at room temperature

Figure 3.5(a) shows the pump photon energy ($\hbar\omega$) dependence of the quasi-autocorrelation signals of the THz emission from the superlattices at an applied voltage V_B = -0.3 V (the internal electric field is estimated to be about 18 kV/cm).
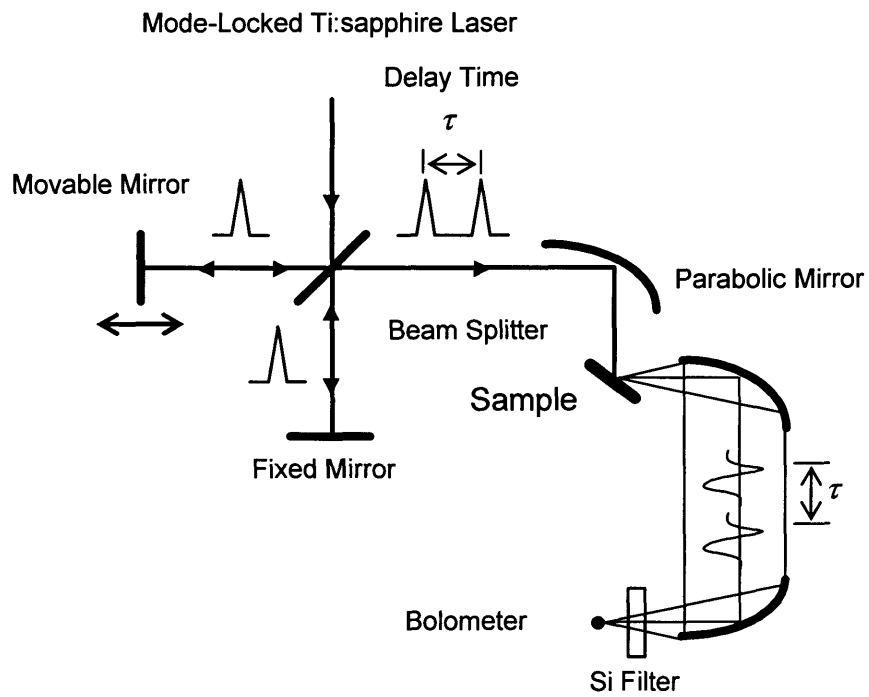
Fig. 3.4 Schematic illustration of the experimental setup of the time-resolved THz quasi-autocorrelation spectroscopy.

Autocorrelation signals with a large central peak accompanied by dips on both sides are clearly observed. Noisy feature around $\tau = 0$ is due to interference fringes of the pump pulses. The autocorrelation signals become stabilized at around 1.5 ps, suggesting acceleration/deceleration of electrons in the miniband takes place in this time scale. The intensity of the central peak of the autocorrelation signals becomes larger as $\hbar\omega$ is reduced from 1.50 eV to 1.46 eV. It is also noted that a few cycle clear oscillations appear around $\hbar\omega = 1.46$ eV, which is around the center of the Wannier-Stark ladder. In general, when a drift velocity of electrons has overshoot characteristics, the time derivative of the drift velocity has both positive and negative regions; the positive and negative regions correspond to acceleration and deceleration of electrons, respectively. Since the autocorrelation of such positive and negative signals forms a dip, the observed dips are the indication that electrons experience a velocity overshoot in the miniband.

To visualize the transient velocity of electrons in the miniband transport, we have fitted the autocorrelation signals by numerical simulation. Results of the calculations are shown by dotted lines in Fig. 3.5(a). Figure 3.5(b) shows the estimated transient velocities of electrons. It is noted that oscillatory transient velocity is expected even at $T = 300$ K.

3.4.3 Bias dependence of THz emission from SLs

The emitted THz radiation intensity is plotted as a function of bias electric field F (open circle) in Fig. 3.6(a). At low field, the emitted THz intensity increases with increasing F, which is consistent with ordinary band transport picture. However, when F exceeds 12 kV/cm, the THz intensity starts to decrease with increasing F, indicating that the dipole moment of oscillating electrons decreases with F. This is a clear evidence of the formation of WSL above a critical electric field. Figure 3.6(b) shows the time-domain autocorrelation traces of the THz emission measured at various bias electric fields F. Clear dips due to velocity overshoot are observed on both sides of the central peak.
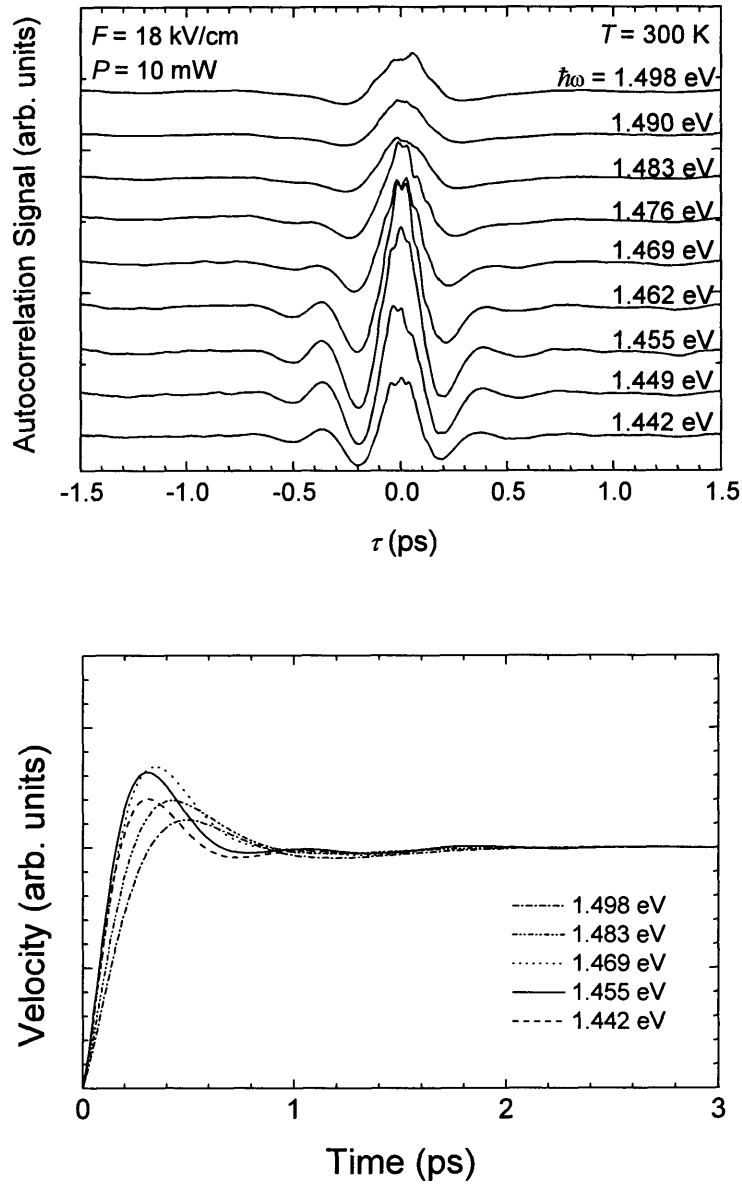
Fig. 3.5 (a) Pump photon energy dependence of the quasi-autocorrelation signals of the THz emission from the superlattices measured at an applied voltage V_B = -0.3 V (F = 18 kV/cm). Dotted lines show results of numerical fitting. (b) Transient velocities of electrons in the miniband estimated from the measured THz autocorrelation signals.
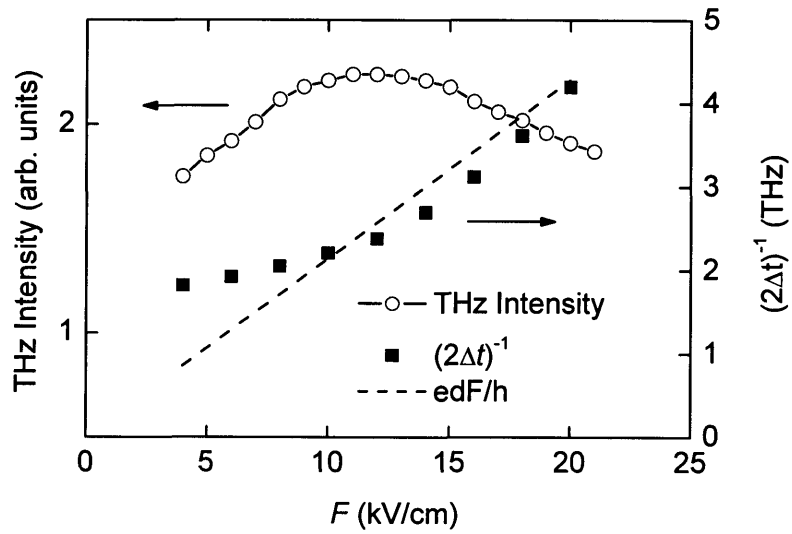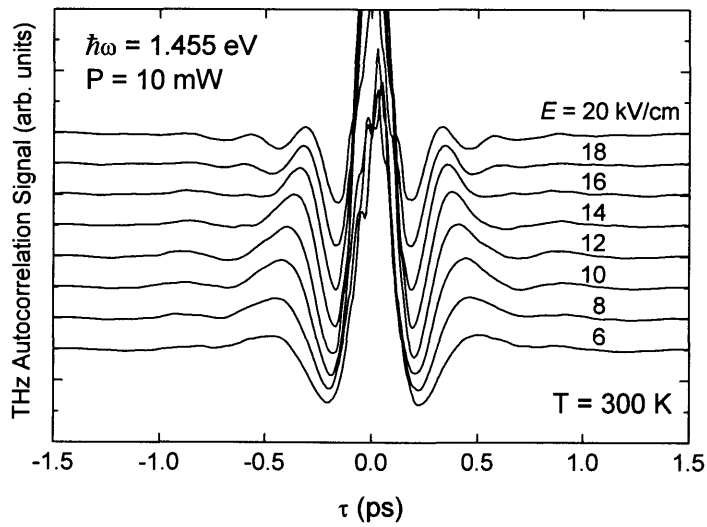
Fig. 3.6 (a) The THz intensity (open circles) and $(2\Delta t)^{-1}$ (full squares) as a function of F for $\hbar\omega = 1.455$ eV. The dashed line denotes the expected Bloch Frequency. (b) The autocorrelation traces of the THz emission measured for various F.

However, when $F > 14$ kV/cm, weak oscillations start to show up in the trailing part of the traces. Furthermore, the oscillation periods become shorter with increasing F. In Fig. 3.6(a), the inverse of the time intervals between the dip and the second peak (square) is plotted as a function of F. As seen in the figure, it approaches the expected Bloch frequency (dashed line) for $F > 14$ kV/cm. This time domain data also strongly support the formation of the WSL and the onset BO. It is also noted that a few cycle BO is observed even when the miniband width is larger than the LO phonon energy.

3.4.4 Pump photon energy dependence of THz emission

Figure 3.7 shows the THz autocorrelation traces measured at $F \sim 18$ kV/cm for various pump photon energies, $\hbar\omega$. The photoexcitation in the first miniband occurs in the photon energy range from 1.44 eV (bottom) to 1.49 eV (top) as determined from the photocurrent measurements shown in Fig. 3.3(b). The pump photon energy, $\hbar\omega$, was varied from 1.442 to 1.498 eV so as to cover the whole miniband. It is noted from Fig. 3.7 that clear oscillations are observed only when the electronic states close to the bottom of the miniband is photoexcited. On the contrary, the oscillations are washed out for $\hbar\omega > 1.462$ eV. Furthermore, the intensity of central peak of the autocorrelation signals becomes smaller as $\hbar\omega$ is increased. This behavior can be understood in the following way; when the SL is pumped at the bottom of the miniband, the photoexcited electrons occupy the initial momentum states with $k_z \sim k_{xy} \sim 0$. In this case, when electrons are accelerated by F, they move almost in phase from $k_z \sim 0$. However, when the top of the miniband is photoexcited, not only electrons with $k_z \sim \pi/d$ and $k_{xy} \sim 0$ but also those with small k_z and large k_{xy} are photoexcited. Hence, the initial momentum of electrons in the acceleration direction, k_z, is not uniquely determined. Consequently, the phase of BOs is not well defined and clear oscillations are not visible.
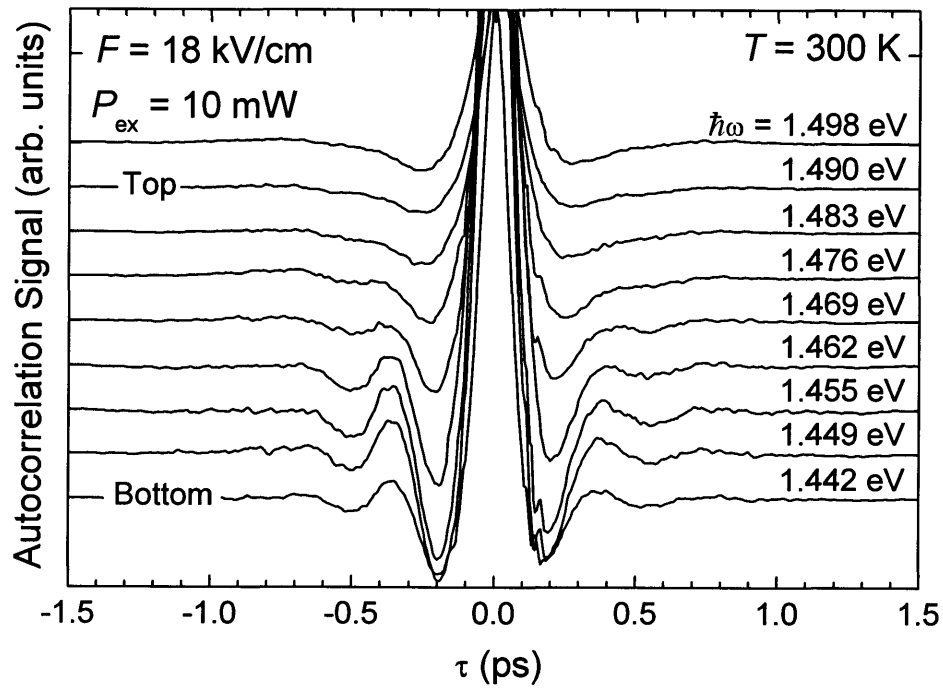
Fig. 3.7 The autocorrelation traces of the THz emission from the superlattices measured at $F = 18$ kV/cm for various pump photon energy.

3.4.5 Summary

In this section, we have investigated a direct observation of THz emission due to BO in wide miniband GaAs/AlGaAs superlattice m-i-n diodes by time-resolved THz spectroscopy. Quasi-autocorrelation measurements were performed on the emitted THz electromagnetic wave by using a bolometer as a wideband detector. We have found that the THz radiation is strongly dependent on the miniband width. Furthermore, we have found that the THz emission due to miniband transport is strongly dependent on the photon energy of the pump laser pulses. We would like to emphasize that the visibility of BOs is strongly dependent on the preparation of the initial wave packets by femtosecond laser pulses. The bias-field dependence of the emitted THz radiation intensity clearly showed a crossover from the miniband transport to the formation of WSL. In the WS regime, a few cycle BO were observed even at 300 K in a superlattice whose miniband width is greater than the LO phonon energy.

3.5 Terahertz conductivity and possible Bloch gain

3.5.1 Introduction

Owing to the progress in fine epitaxy techniques and femtosecond laser spectroscopy, experiments have emerged that lend credibility to the early proposal by Esaki and Tsu. Ultrafast time-domain experiments on high quality samples unambiguously demonstrate that electrons in superlattice minibands perform at least a few cycle Bloch oscillations [10]. However, the idea of Bloch oscillator was challenged in a more fundamental way by asking whether BO is useful in generating/amplifying electromagnetic (EM) waves [37]. When an electric field is applied to an ideal SL, the miniband is split into equally spaced Wannier-Stark (WS) ladder states with an energy separation of $\hbar\omega_B$ (ω_B the Bloch frequency and $\hbar$ the reduced Planck constant). Since the emission and absorption of EM

waves take place between the adjacent two WS levels, they occur at the same frequency and, hence, cancel each other. Consequently, an ideal SL has no net gain or loss for EM waves. However, when scattering exists in the system, the situation changes; in the presence of scatterers, new transition channels, i. e., scattering-assisted transitions, become available. Since the scattering-assisted emission (absorption) occurs at frequencies slightly lower (higher) than ω_B, gain (loss) for EM waves is expected below (above) ω_B.

The direct experimental proof of such THz gain is to show that the real part of the carrier conductivity, $Re[\sigma(\omega)]$, becomes negative in the THz range. The conventional method for determining $Re[\sigma(\omega)]$ in the THz range is the measurement of free carrier absorption in doped SLs under bias electric fields by using, for example, Fourier transform spectrometers. Here, fundamental problems arise; 1) For such measurements, a large sample size, typically a few mm^2, is necessary. Then, an extremely large current flows through the sample under biased conditions. 2) The profile of internal electric field in doped SLs becomes very non-uniform due to the formation of high-field domains. These two inevitable problems have made the conventional measurements practically impossible so far.

In this section, we show a strong experimental support for the THz gain due to Bloch oscillating electrons in wide miniband GaAs/Al$_{0.3}$Ga$_{0.7}$As SLs. For determining the high-frequency electron conductivity in SL minibands, we took a totally different approach; we used undoped SL samples in order to avoid large current density and high-field domain formation, and took all the necessary information within a few ps, by noting that the time-domain THz spectroscopy inherently measures the step-response of the electron system to the applied bias electric field and that the Fourier spectra of the THz emission is closely related with $\sigma(\omega)$. Quasi-autocorrelation measurements were performed on the emitted THz electromagnetic wave and the obtained spectra were compared with $|\sigma(\omega)|^2$ predicted by Ktitrov et al. [11]. Although we do not directly show a negative $Re[\sigma(\omega)]$, excellent agreement between theory and experiment on $|\sigma(\omega)|^2$-spectra strongly suggests that the THz gain due to Bloch oscillating electrons

persists at least up to 1.7 THz. It is also found that Zener tunneling into the second miniband sets the high-frequency limit of the THz gain for the samples studied here.

3.5.2 Device structure and experimental setup

The samples used in this work were $GaAs/Al_{0.3}Ga_{0.7}As$ SL m-i-n (metal-intrinsic-n^+-type) diode structures. Two different wide miniband SL samples were prepared by growing undoped $GaAs/Al_{0.3}Ga_{0.7}As$ SL layers (sample #1: 8.2 nm/0.8 nm and sample #2: 6.4 nm/0.56 nm) on n^+-GaAs substrates by molecular beam epitaxy. The first miniband widths, Δ, of the two samples were designed to be 50 and 100 meV, respectively. For both samples, the second miniband is separated by a 40 meV-wide minigap. The thickness of the undoped SL layers was 500 nm. The top contacts were formed by depositing semi-transparent 4 nm-thick NiCr Schottky films and the bottom ohmic contacts were formed by annealing AuGeNi alloy. By applying a bias voltage, V_b, between the top and the bottom electrodes, we can tune an internal electric field, F, in the undoped SL region. When a femtosecond laser pulse excites the sample, electron-hole pairs are optically injected into the miniband. Due to an applied electric field, F, the carriers start drifting and THz radiation that is proportional to the carrier acceleration is emitted into free space. Since the miniband width for heavy holes is only a few meV, which is much narrower than that for electrons, heavy holes are almost localized. Furthermore, absorption due to light holes is 1/3 of that due to heavy holes. Consequently, electron motion dominates the emitted THz signal.

To verify the formation of the miniband and the WS ladder in our samples, we first took weak-excitation interband photocurrent spectra, I_{ph}. Figure 3.8(a) shows the contour plot of the derivative of the interband photocurrent spectrum, $dI_{ph}/dh\nu$, measured on sample #1 (Δ = 50 meV), where $h\nu$ is the incident photon energy. For +0.8 V > V_b > +0.5 V, only an excitonic absorption at the bottom of the miniband is observed. However, when V_b is reduced below +0.5 V, the spectrum starts showing rich structures which

originate from the formation of WS ladder.   Six ladder levels are clearly seen in the figure, indicating a good quality of the sample.

For time-domain THz emission spectroscopy, we used a quasi-autocorrelation geometry [20], i. e., the power of the THz radiation generated by a pair of time-correlated femtosecond laser pulses was measured as a function of the time interval, τ, between the two laser pulses imposed by a Michelson interferometer.   When the two laser pulses excite the sample, two almost identical THz EM waves are consecutively emitted. Experiments were performed by using 100 fs laser pulses delivered from a mode-locked Al_2O_3:Ti laser.   The laser pulses were loosely focused onto the sample surface at a polar angle of 70°.   The typical pump power, P, used in the experiment was 10 mW.   In this way, the carrier densities excited in the active region was kept as low as 2×10^{14} cm^{-3} to avoid field screening.   The generated THz emission was detected by a wideband Si bolometer operated at 4.2 K.   The detail of the experiment can be found elsewhere [30]. The samples were cooled at $T = 10$ K in a continuous flow He cryostat.   The pump photon energy was set to be 1.55 eV, which is close to the bottom of the miniband, as indicated by a horizontal arrow in Fig. 3.7(a) [30].

3.5.3 Fourier spectra of THz emission from SL

Figure 3.8(b) shows the integrated intensity of the emitted THz radiation as a function of V_b measured for sample #1.   The THz intensity starts rising at around V_b = +0.65 V, indicating that this voltage is the flatband voltage, V_{b0}, in this particular sample. With decreasing V_b (i. e., increasing reverse bias), the THz intensity increases first. However, when the reverse bias exceeds -0.1 V, the THz intensity starts to roll off due to the field-induced Stark localization [30].

Figure 3.9(a) plots the autocorrelation traces of the emitted THz radiation measured at various F for sample #1.   The internal electric field F was estimated from V_{b0} and the total thickness of the undoped SL layer.   At very low fields, a hump is seen at around $\tau =$
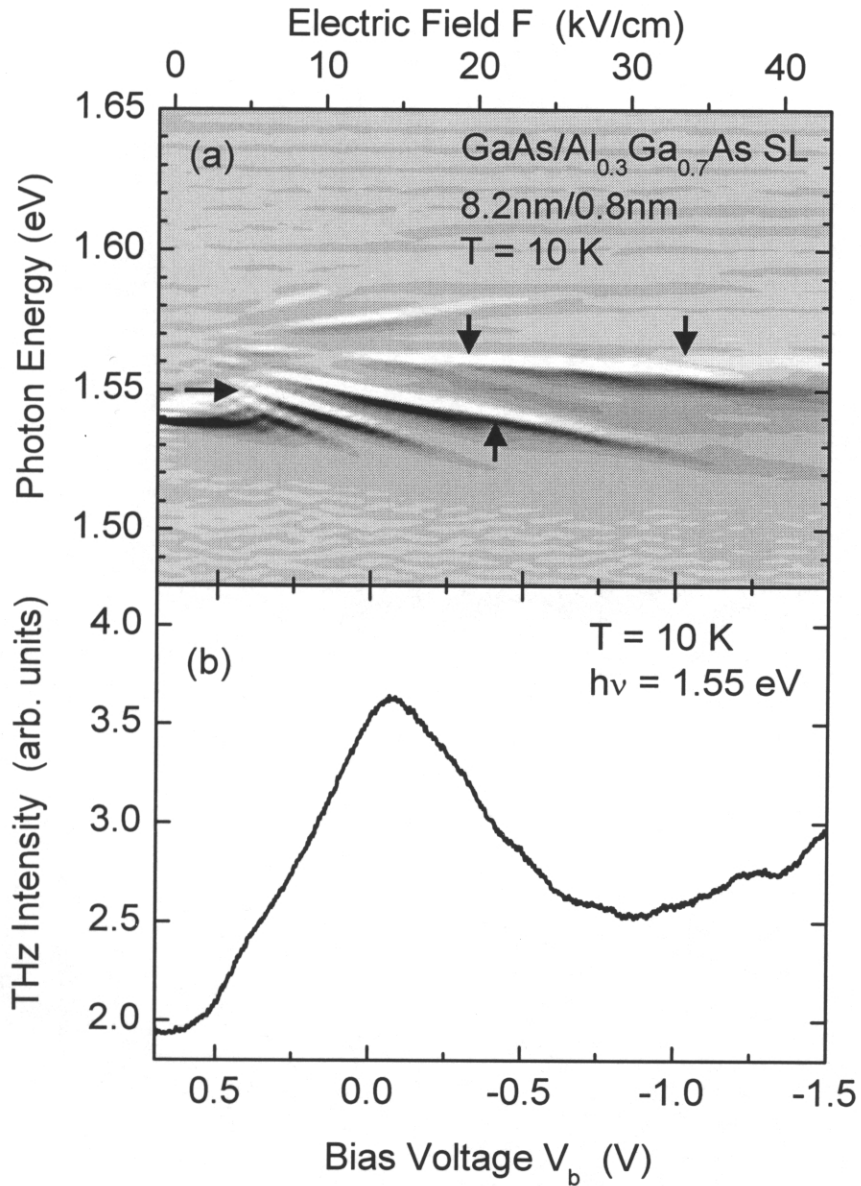
Fig. 3.8 (a) The contour plot of the derivative spectra of the weak excitation interband photocurrent, $dI_{ph}/dh\nu$, measured on sample #1 as a function of the applied bias voltage. The horizontal arrow denotes the photon energy of the femtosecond laser pulses used for the time-domain THz measurements. The vertical arrows indicate the anti-crossing points due to Zener tunneling into the second miniband. (b) The integrated intensity of the THz emission is plotted as a function of the bias voltage.

Fig. 3.9 (a) The autocorrelation traces of the THz emission and (b) their Fourier spectra measured on sample #1 for various bias electric fields from 1 kV/cm to 29 kV/cm with 2 kV/cm-step. The traces are shifted for clarity.
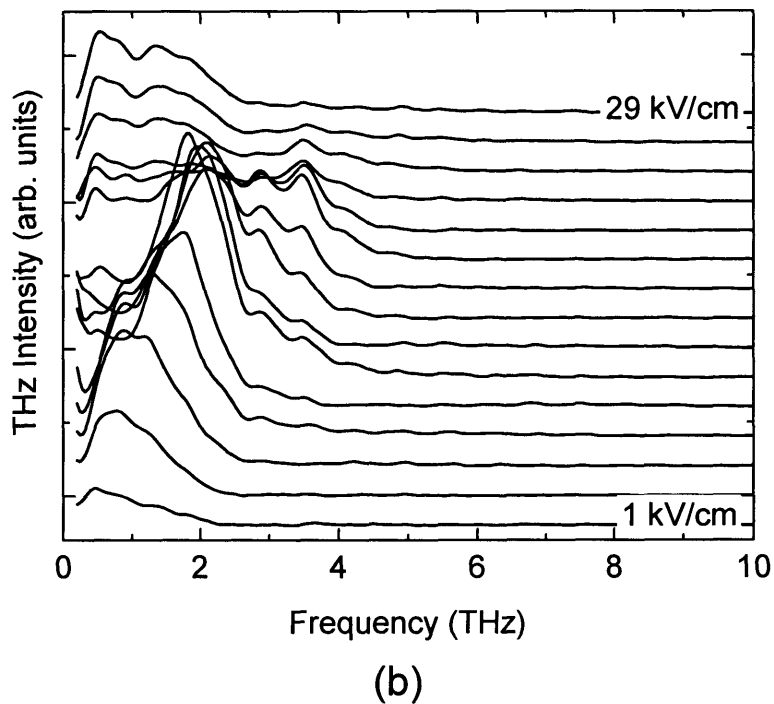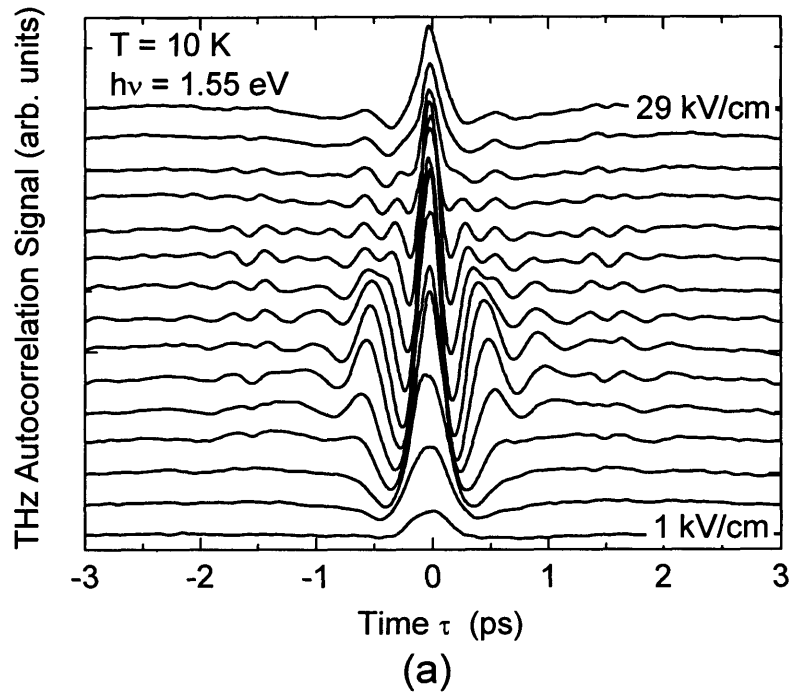
0. However, as we increase F, a few cycle oscillations start to show up. From the F-dependence of the oscillation frequency, the observed oscillations were identified as Bloch oscillations. The Fourier spectra of the time-domain traces are plotted in Fig. 3.9(b). As seen in the figure, the peak position of the Bloch oscillation shifts to higher frequency as F is increased. However, for $F > 17$ kV/cm, the spectral shape drastically changes and becomes very broad. The behavior in the large reverse bias region will be discussed later.

3.5.4 THz gain due to Bloch oscillating electrons

At this stage, we would like to discuss what the THz emission spectra represent. In the THz emission experiment, we first set a dc electric field F in the SL and, then, shoot a fs-laser pulse to the sample at $t = 0$ to create a step-function-like carrier density, $n_0 \Theta(t)$, in the sample. Subsequently, THz radiation is emitted from the accelerated photoexcited electrons. Now, by using our imagination, we will view the experiment in a different way. Let us perform the following thought experiment; we first set electrons in the conduction miniband under a flatband condition and, at $t = 0$, suddenly apply a step-function-like bias electric field, $F\Theta(t)$. We notice that electrons in the thought experiment emit the same THz radiation as in the actual experiment [38]. This fact implies that the time-domain THz experiment inherently measures the step-response of the electron system to the applied electric field.

By noting this important conclusion, we formulate the THz emission process as follows; the creation of step-function-like carrier density by fs laser pulses in the actual process is replaced with the application of step-function-like electric field in the thought experiment as,

$$F(t) = F\Theta(t), \quad \widetilde{F}(s) = \frac{F}{s}. \tag{3.9}$$

Here, the variables with $\sim$ denote their Laplace transformation. The transient current by

the photoexcited electrons in the miniband is given by,

$$\tilde{J}(s) = \tilde{\sigma}(s)\tilde{F}(s).$$

(3.10)

Then, the emitted THz electric field, E_{THz}, can be obtained as,

$$E_{THz} \propto \frac{\partial J(t)}{\partial t} = \frac{F}{2\pi i}\int_{c-i\infty}^{c+i\infty} ds\, e^{ts}\tilde{\sigma}(s) = \sigma(t)F,$$

(3.11)

where $\sigma(t)$ is the electron conductivity in the time-domain. Eq. (3.11) tells us that, since the spectra shown in Fig. 3.9(b) are the Fourier spectra of the THz autocorrelation traces, they are proportional to $|\sigma(\omega)|^2 F^2$.

In the following, we will compare the observed THz spectra with the conductivity theoretically predicted for the Bloch oscillating electrons by Ktitrov, et al. by solving the semi-classical Boltzmann transport equation [11];

$$\sigma(\omega) = \sigma_0 \frac{1 - \omega_B^2 \tau_m \tau_e - i\omega\tau_e}{(\omega_B^2 - \omega^2)\tau_m\tau_e + 1 - i\omega(\tau_m + \tau_e)} \quad \text{with} \quad \sigma_0 = \frac{\sigma_{00}}{1 + \omega_B^2\tau_m\tau_e}$$

(3.12)

, where τ_m and τ_e are the momentum and energy relaxation times of electrons, respectively, and σ_{00} a constant. The top and the middle panels of Fig. 3.10 show the calculated real- and imaginary-part of the miniband conductivity, and the bottom panels show the measured THz spectra and calculated $|\sigma(\omega)|^2$ for two representative bias conditions. τ_m and τ_e in the calculation were determined to be 0.15 ps and 1.5 ps, respectively, from numerical fitting. ω_B at $F = 1.0$ kV/cm was simply set to be $edF/\hbar$. However, we found that the peak position of the THz spectrum at 11.1 kV/cm is slightly lower than the value simply expected from $edF/\hbar$ (2.41 THz), which is due to anti-crossing with the WS ladder states of the second miniband, as will be discussed later. We set ω_B at $F = 11.1$ kV/cm to be 1.96 THz, which gives the best fit to the experimental data.

At very low field ($F = 1.0$ kV/cm, $\omega_B(\tau_m\tau_e)^{0.5} = 0.66$), the conductivity spectra and the THz emission show more or less a Drude-like behavior (See Fig. 3.10(a)). However, as F is increased (Fig. 3.10(b)), the THz emission peak, which is mainly caused by a dip structure in $\text{Im}[\sigma(\omega)]$ at ω_B, shifts to the higher frequency. At the same time, the negative $\text{Re}[\sigma(\omega)]$ below ω_B spreads. Consequently, the expected $|\sigma(\omega)|^2$-spectra becomes

98
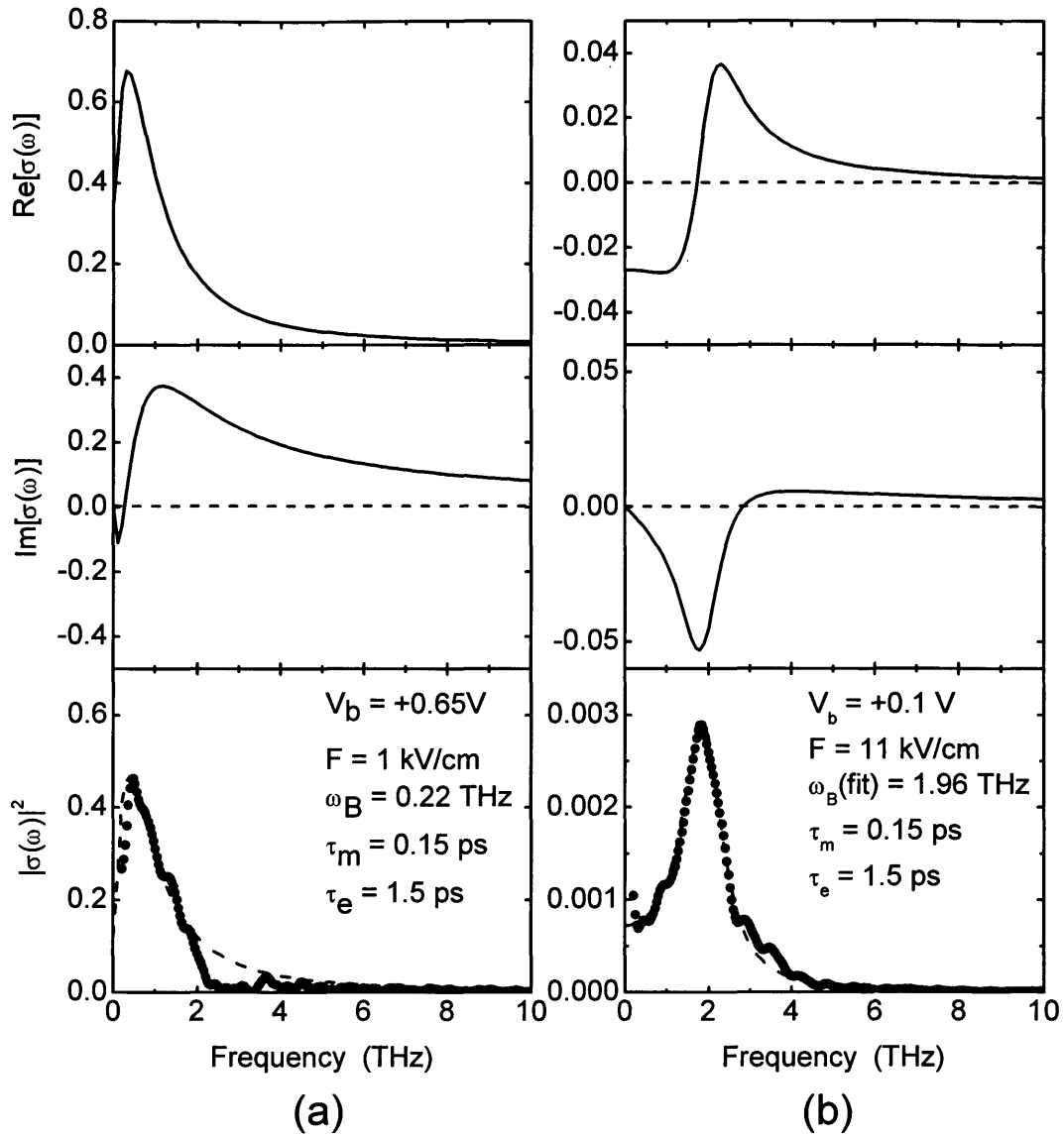
Fig. 3.10 The top and middle panels respectively show the calculated real and imaginary parts of the high-frequency electron conductivity in the superlattice miniband, $\sigma(\omega)$. The bottom panels show the calculated $|\sigma(\omega)|^2$-spectra (dashed line) and the THz emission spectra (dots) measured for sample #1 by the time-domain THz spectroscopy experiments. The scattering times used in the calculation were determined from numerical fitting. (a) $F = 1.0$ kV/cm and (b) $F = 11$ kV/cm.

asymmetric with an enhanced low-frequency spectral component. As seen in Fig. 3.10(b), it is noted that the THz emission at F = 11.1 kV/cm ($\omega_B(\tau_m\tau_e)^{0.5}$ = 5.8) indeed has a characteristic asymmetric spectral shape and that the agreement between the observed THz emission and the calculated $|\sigma(\omega)|^2$ is excellent, indicating that the emitted THz electric field, E_{THz}, is indeed proportional to $\sigma(\omega)$ of Bloch oscillating electrons. Furthermore, the calculated Re[$\sigma(\omega)$] strongly suggests that the THz gain persists at least up to 1.7 THz. Similar experiments were performed for sample #2 (Δ = 100 meV). Figure 3.11 summarizes the THz spectra and the calculated $|\sigma(\omega)|^2$ for various F. The sharp dip at 0.5 THz in the measured data are due to the water vapor absorption and are not relevant to the present discussion. The excellent agreement between experiment and theory further confirms the above conclusion.

Now, we would like to discuss what limits the maximum frequencies of the Bloch gain in SLs. The good agreement between theory and experiment discussed above was obtained only up to 13 kV/cm for the THz data shown in Fig. 3.9(b). As F is further increased, the period of the Bloch oscillation becomes shorter but, at the same time, the amplitude gradually diminishes. Concomitantly, the Fourier spectra become very broad (see Fig. 3.9(b)). We attribute this behavior to the anti-crossing of the WS states of the first miniband with those of the second miniband, i. e., Zener tunneling into the second miniband. Let us take a look at Fig. 3.8(b) again. It is noted that the THz emission becomes brighter with increasing field for V_b > -0.8 V (F > 29 kV/cm). This fact contradicts with what is expected from simple field-induced Stark localization and indicates that electrons in the first miniband find a new conduction channel. This new channel is the Zener tunneling into the second miniband. Further support can be seen in the interband photocurrent spectra shown in Fig. 3.8(a), where anti-crossing feature can be observed in the high bias region, as indicated by vertical arrows [39]. From these data, it is concluded that the Zener tunneling into the higher miniband set the high-frequency limit to the Bloch gain in the sample studied here.
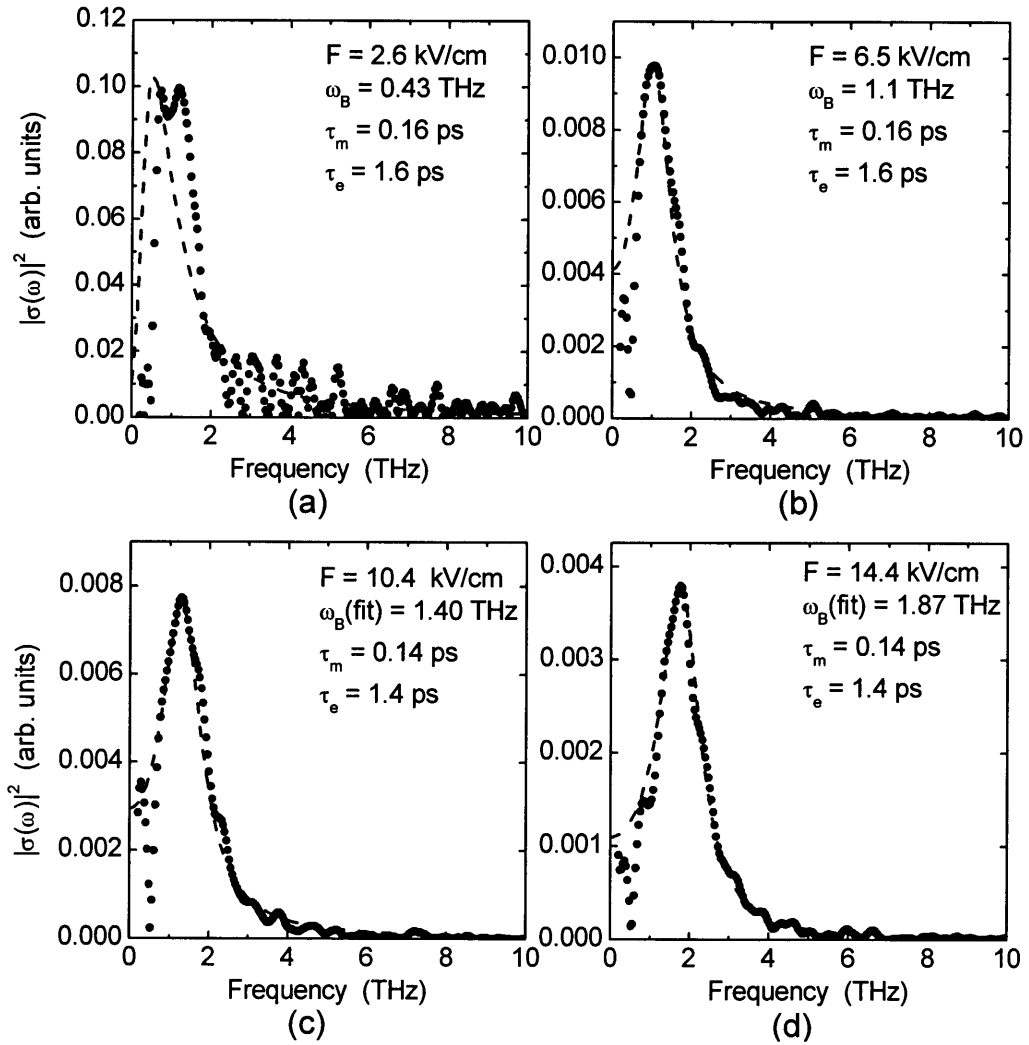
Fig. 3.11 The calculated $|\sigma(\omega)|^2$-spectra (dashed line) and the THz emission spectra (dots) measured for sample #2 are shown for four bias electric fields (a) 2.6 kV/cm, (b) 6.5 kV/cm, (c) 10.4 kV/cm, and (d) 14.4 kV/cm. The sharp dips in the THz emission spectra are due to water vapor absorption. The scattering times used in the calculation were determined from numerical fitting.

3.5.5 Summary

In this section, we have investigated THz emission due to dynamical electron transport in wide miniband GaAs/$Al_{0.3}Ga_{0.7}As$ superlattices by time-domain THz emission spectroscopy. By noting that the time-domain THz spectroscopy inherently measures the step-response of the electron system to the bias electric field, the obtained THz spectra were compared with theoretically predicted high-frequency conductivity. Excellent agreement between theory and experiment strongly supports that the THz gain due to Bloch oscillating electrons in wide-miniband superlattices persists at least up to 1.7 THz. It is also found that Zener tunneling into the second miniband sets the high-frequency limit of the THz gain for the samples studied here.

3.6 Inter-miniband resonant Zener tunneling

3.6.1 Introduction

In recent years, a technique that measures the THz electromagnetic wave emitted by ultrafast transient electron motions has been established (time-resolved THz emission spectroscopy). This technique has made it possible to observed ultrafast motion of electrons in superlattices [30]. Recently, a strong experimental support for the THz gain up to a few THz due to Bloch oscillating electrons has been presented [19]. It was also found that the high-frequency limit to the Bloch gain is set by the Zener breakdown of the intra-miniband transport [19]. Therefore, it is prime importance to clarify the electronic structures of higher-lying minibands/minigaps in a strong bias field range.

In this section, we investigate the THz emission induced by high-field electron transport in biased wide-miniband GaAs/$Al_{0.3}Ga_{0.7}As$ SLs. THz emission spectroscopy was performed on the emitted THz electromagnetic wave due to electron motion in the SLs by using a bolometer as a wideband detector. With increasing bias fields, two distinct

regimes are observed in the bias-field dependence of the emitted THz intensity. These two regimes are attributed to the intra-miniband transport and inter-miniband Zener tunneling regimes, respectively. In a high bias-field region, quasi-periodic structures were observed in the emitted THz intensity-vs-bias field curve and were identified to be due to the resonant Zener tunneling between the Wannier-Stark (WS) ladders associated with the ground and the excited minibands. Resonant Zener tunneling up to the 8th-nearest neighbor quantum wells was clearly resolved.

3.6.2 Experimental setup

The samples used in this work were $GaAs/Al_{0.3}Ga_{0.7}As$ superlattice m-i-n (metal - intrinsic - n^+-type) diode structures. The samples were prepared by growing 500 nm-thick undoped $GaAs/Al_{0.3}Ga_{0.7}As$ superlattice layers on n^+-GaAs substrates by molecular beam epitaxy. We designed the GaAs wells (6.4 nm) and $Al_{0.3}Ga_{0.7}As$ barriers (0.56 nm) so as to set the first miniband width, Δ_1, to be 100 meV for sample 1. The other sample (sample 2) had 8.2 nm-thick GaAs wells and 0.8 nm-thick $Al_{0.3}Ga_{0.7}As$ barriers, and Δ_1 was designed to be 50 meV. In both samples, the second miniband was separated by a 40 meV-wide minigap. The top contact was formed by depositing a semi-transparent 4 nm-thick NiCr Schottky film and the bottom ohmic contact was formed by alloying AuGeNi/Au. When a femtosecond laser pulse excites the sample, electron-hole pairs are optically created in the miniband. Due to an applied electric field, F, the carriers start drifting and THz electromagnetic wave that is proportional to the carrier acceleration is emitted into free space. Since the miniband width for heavy holes is 2.5 meV, which is much narrower than that for electrons, heavy holes are considered to be almost localized. Furthermore, absorption due to light holes is 1/3 of that due to heavy holes. Consequently, the motion of electrons dominates the emitted THz signal.

To verify the formation of miniband and the WS ladder in our samples, we have taken low-excitation photocurrent spectra at $T = 10$ K shown as Fig. 3.12. The

photocurrent spectra have been differentiated with respect to the energy in order to improve the visibility of weak transitions. The spectra show rich structures at $T = 10$ K, which originate from a formation of the WS ladder. For low applied bias voltage, the spectra are weakly structured. At higher electric field, each line fans out into a series of discrete transitions as expected WS ladder. Eight ladder levels are clearly seen in the figure, indicating a good quality of the sample. It is also found that the miniband is formed in an energy range from 1.53 eV (810 nm) to 1.63 eV (760 nm) at $T = 10$ K.

For time-resolved THz spectroscopy, we used a quasi-autocorrelation geometry [20], i. e., the power of THz radiation generated by a pair of time-correlated femtosecond (fs) laser pulses was measured as a function of the time interval, τ, between the two laser pulses imposed by a Michelson interferometer. Experiments were performed by using 100 fs laser pulses delivered from a mode-locked Al_2O_3:Ti laser operated at a repetition rate of 76 MHz. The laser pulses were loosely focused ($\phi = 1$ mm) onto the sample surface at a polar angle of 70° in reflection geometry by a gold-coated off-axis parabolic mirror with a 60 cm effective focal length. In a loosely focused condition, the mechanism of the THz emission is dominated by acceleration/deceleration of photoexcited carriers in the superlattice miniband. A typical pump power used in the experiment was 10 mW. In this way, the carrier densities excited in the active region can be kept as low as 2×10^{14} cm^{-3} to avoid field screening and the average current density was about 0.1 A/cm^2. The generated THz emission was collimated by off-axis parabolic mirrors and focused onto a Si bolometer operated at 4.2 K. The optics and the sample were kept in an enclosure purged with nitrogen to minimize the absorption by atmospheric moisture. In our quasi-autocorrelation measurements the detected signal intensity is a time-integrated power of the THz electric fields consecutively emitted from the sample. The signal was recorded by using a standard lock-in technique at a modulation frequency of about 400 Hz.
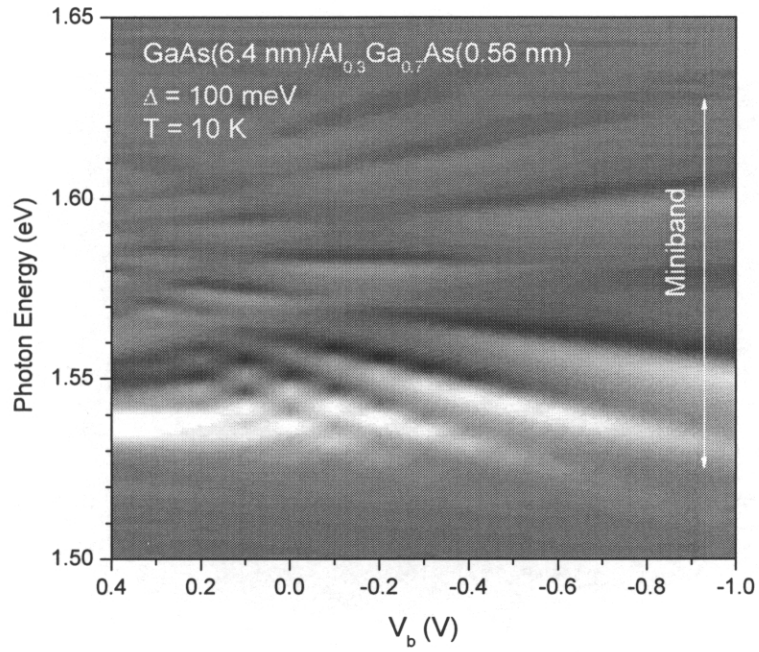
Fig. 3.12 Gray-scale map of the differential interband photocurrent of the superlattice sample as a function of applied bias voltage and photon energy at $T = 10$ K.

3.6.3 THz intensity emitted from superlattices

Figure 3.13(a) shows the bolometer output for the THz radiation emitted from sample 1 as a function of the bias voltage V_b, applied to the SL. The THz intensity starts rising at around V_b = +0.83 V, indicating that this voltage is the flatband voltage, V_{b0}, for this particular sample. The applied electric fields F was estimated by subtracting V_{b0} from V_b and divided by the total thickness of the superlattices region of 500 nm.

Two distinct regions can be seen in the figure; one region (I) is the THz emission for 0 – 30 kV/cm. THz emission in region-I is due to intra-miniband electron transport [30]. In this region (I), the THz intensity increases first with increasing electric fields from F = 0. When F < ~8 kV/cm, strong interwell coupling leads to the formation of energy minibands. Furthermore, the Bloch energy ($\equiv$ eFd; d: the SL period) is less than the scattering broadening of the WS levels. Therefore, electrons drift in a quasi-continuous miniband. From a closer look at Fig. 3.13(a), a weak kink in the THz emission curve is noticed at ~ 8 kV/cm. For F > ~8kV/cm, the miniband splits into equally spaced WS states and the wave functions are gradually localized (WS localization). In this intermediate field region, clear Bloch oscillations are observed in the time-domain THz data [30]. When F exceeds ~18 kV/cm, THz intensity starts rolling off due to stronger WS localization. The other region (II) is the broad THz emission peak observed for 30 – 110 kV/cm. When F exceeds 30 kV/cm, the reduction of THz intensity saturates and the emission becomes brighter again. Furthermore, quasi-periodic structures are observed on top of the broad peak. The dashed curve is a blowup of the THz intensity in the high-field region. Since the THz intensity is proportional to the carrier acceleration, THz emission becomes brighter whenever carriers find transport channels. We attribute the broad feature and the fine structure to the non-resonant and resonant inter-minibad Zener tunneling effect, respectively. In the following, we will focus our attention to the fine structure in the THz emission traces.
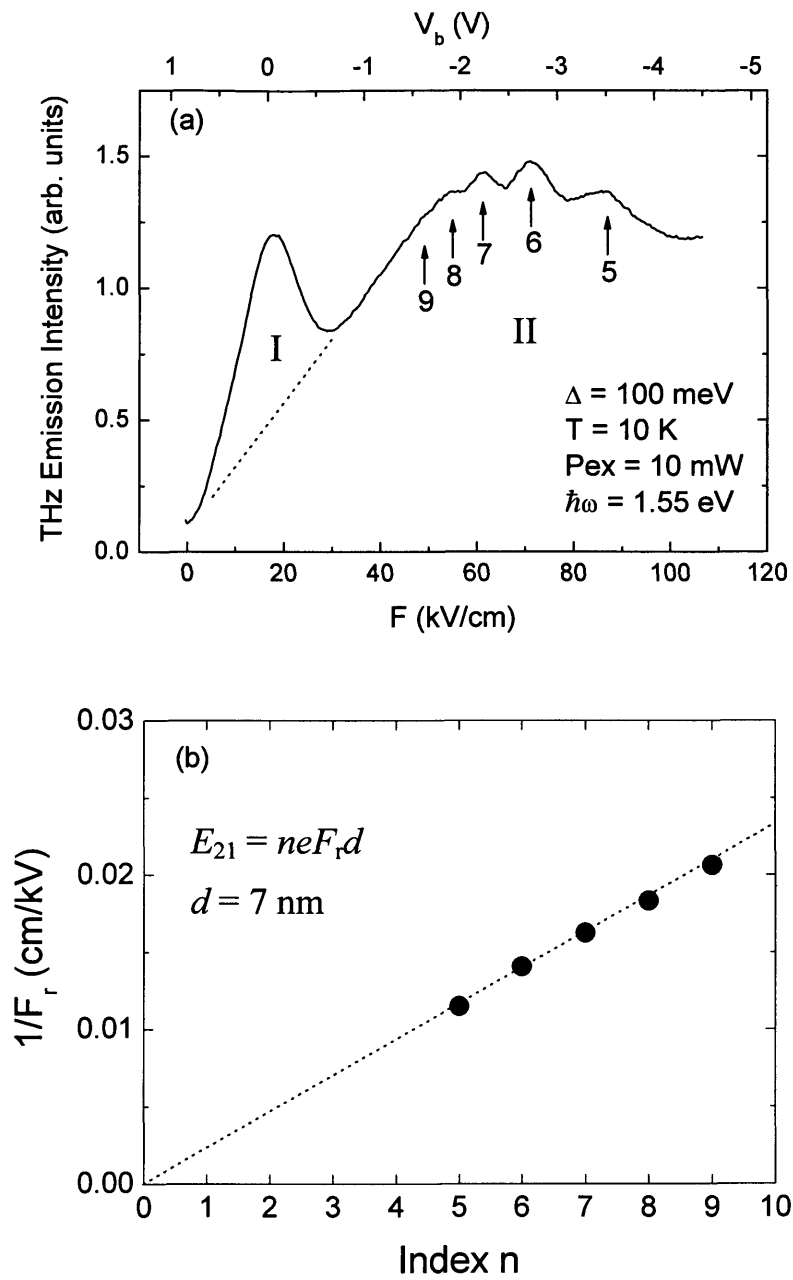
Fig. 3.13 (a) The bias-field dependence of the THz intensity from the superlattices, (b) the inverse of the resonant electric fields as a function of the index number.

3.6.4 Inter-miniband resonant Zener tunneling

Let us consider the band diagram under a strong bias field, where the inter-miniband Zener tunneling takes place. Figure 3.14 shows schematic illustration of the SL band diagram in a high-field condition. Equally spaced WS levels with energy separation of *eFd* are formed for both the first and the second minibands. It is also noted that the energy separation between the first and the second quantized energy levels in each quantum well, $E_{21} = E_2 - E_1$, is almost field-independent, since the quantum confined Stark effect is weak in narrow quantum wells. Consequently, the energy level of the ground state E_1 in the 0-th well is aligned with the excited state E_2 in the n-th well when the electric field F satisfies the condition; $E_{21} = neFd$, where index n denotes the position of the quantum well numbered with respect to the quantum well where the wave function of the ground state is localized (see Fig. 3.14). Under such a condition, electrons in the first miniband can resonantly tunnel into the excited state in the n-th well and the THz emission is enhanced. The resonant state shifts to the neighbor quantum well as increasing electric fields. The THz intensity shows peak structure since the conductivity of electrons becomes large at the resonant conditions. In Fig. 3.13(b), the inverse of the resonance electric field, F_r, indicated by arrows in Fig. 3.13(a) is plotted as a function of the index n. The straight linear dependence between F_r^{-1} and the index n indicates that the quasi-periodic peak structure is indeed due to the inter-miniband resonant Zener tunneling between the WS ladders associated with the first and the second minibands. Inter-miniband resonant Zener tunneling up into the 8th-nearest neighbor quantum well was clearly discernible visible in the wide-miniband SL structure. It is also found that the wave function in the quantum wells extend over ~ 60 nm (8 periods × 7 nm) in the SLs.

Figure 3.15(a) shows the bias field dependence of the integrated THz intensity emitted from sample 2. In Fig. 3.15(b), the inverse of the resonant field indicated by arrows in Fig. 3.15(a) is plotted as a function of the index n, in the same way as in Fig. 3.13(b). A similar straight linear dependence between F_r^{-1} and n is obtained except for
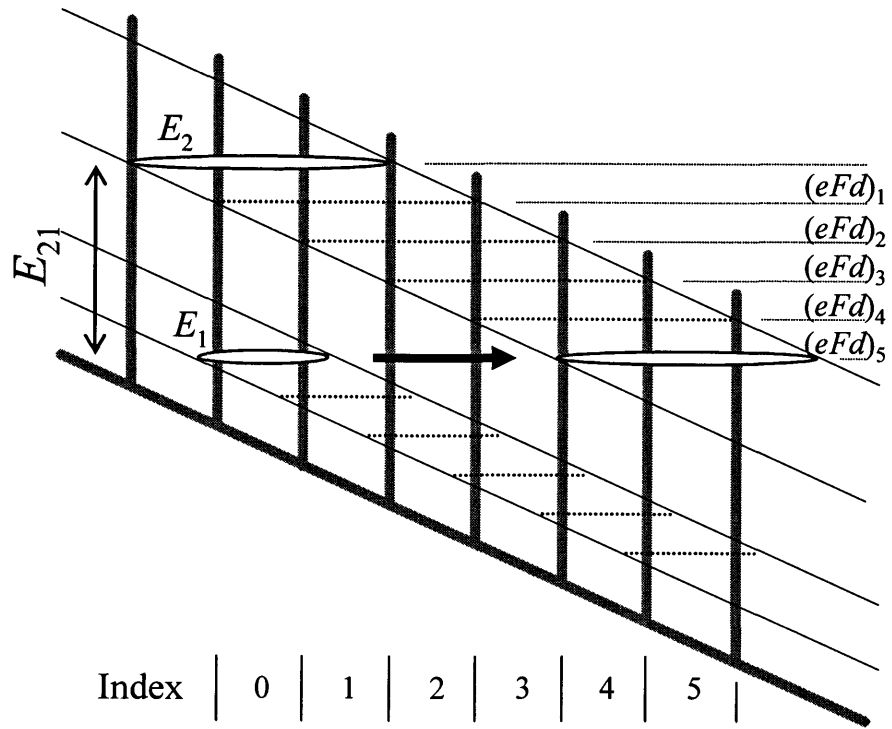
Fig. 3.14 Schematic illustration of a band diagram of the SL structure at high-field condition.

the peaks indexed as (0) and (1). Deviation from a simple linear dependence strongly suggests that multiple minibands participate in the tunneling process.

For more quantitative analysis, we took Fourier transform of the $1/F$-spectra of the quasi-periodic part of the THz data shown in Figs. 3.13(a) and 3.15(a). By doing this, tunneling spectra are obtained as a function of the energy difference measured with respect to E_1, i. e., $E - E_1$. Figures 3.16(a) and 3.16(b) plot the Fourier spectra for sample 1 and 2, respectively. The insets illustrate schematic conduction band profiles of the samples. The gray bars and gaps in the figure denote the positions of the minibands/minigaps in each SL calculated by a simple Kronig-Penny model. The obtained Fourier spectra were positioned in such a way that E_1 is located at the center of the calculated ground minibands. As seen in the figure, a single peak is observed for sample 1, indicating that the resonant Zener tunneling predominantly takes place between the first and the second minibands. On the other hand, two peaks are clearly resolved for sample 2, strongly suggesting that the resonant Zener tunneling takes place even into the WS states associated with the third miniband and that the THz emission peaks numbered (0) and (1) in the Fig. 3.15(a) are due to such processes. It should also be noted that the peaks in the tunneling spectra are located almost at the center of the minibands, which is consistent with the tight binding picture of the miniband formation.

3.6.5 Summary

In this section, we have investigated the THz emission induced by high-field electron transport in biased wide-miniband $GaAs/Al_{0.3}Ga_{0.7}As$ superlattices. THz emission spectroscopy was performed on the emitted THz electromagnetic wave due to electron motion in the SLs by using a bolometer as a wideband detector. With increasing bias fields, two distinct regimes are observed in the bias-field dependence of the emitted THz intensity. These two regimes are attributed to the intra-miniband transport and inter-miniband Zener tunneling regimes, respectively. In the inter-miniband Zener
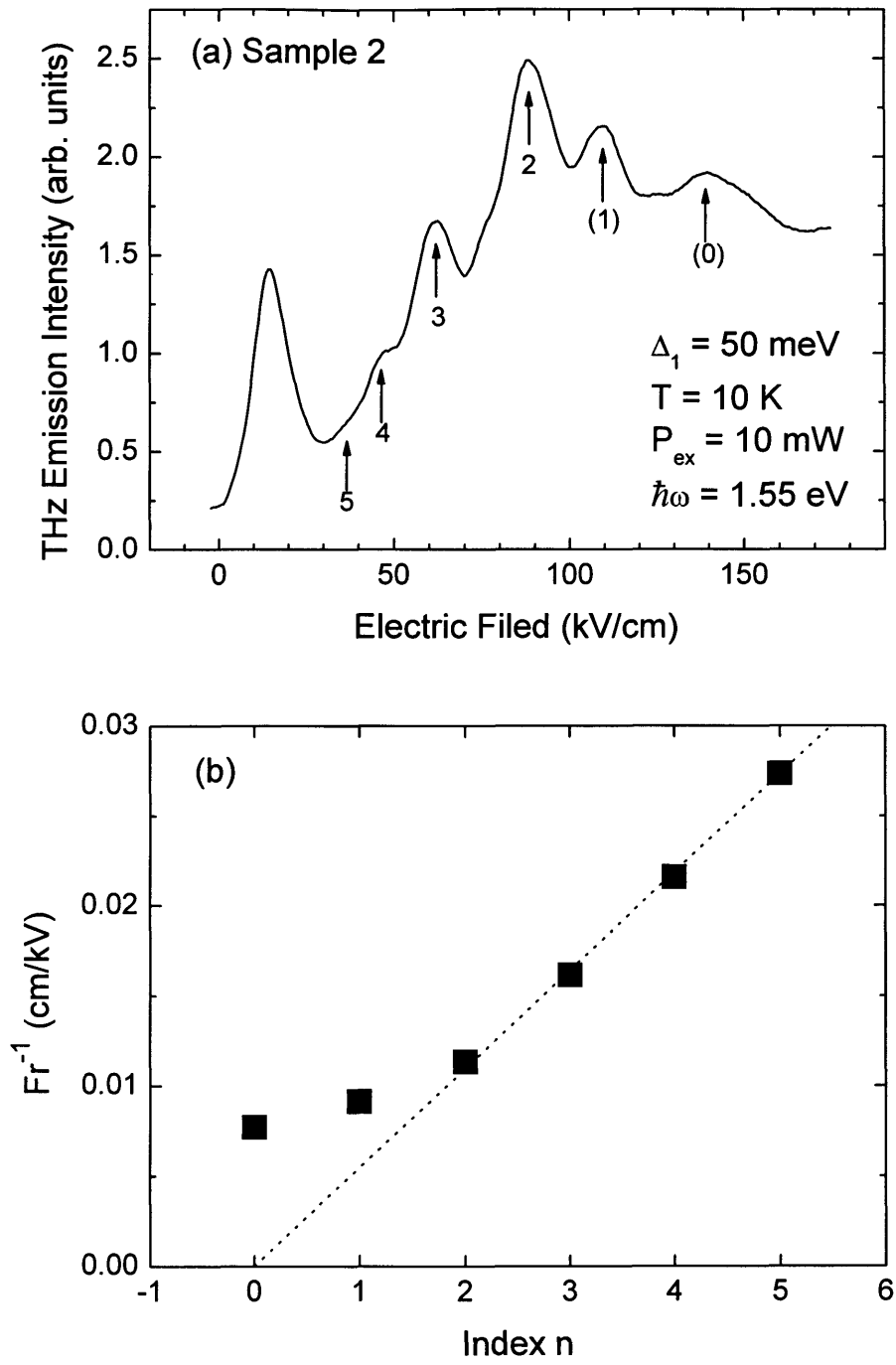
Fig. 3.15 (a) The bias-field dependence of the THz intensity from the sample 2. (b) The inverse of the peak electric fields as a function of the index number.
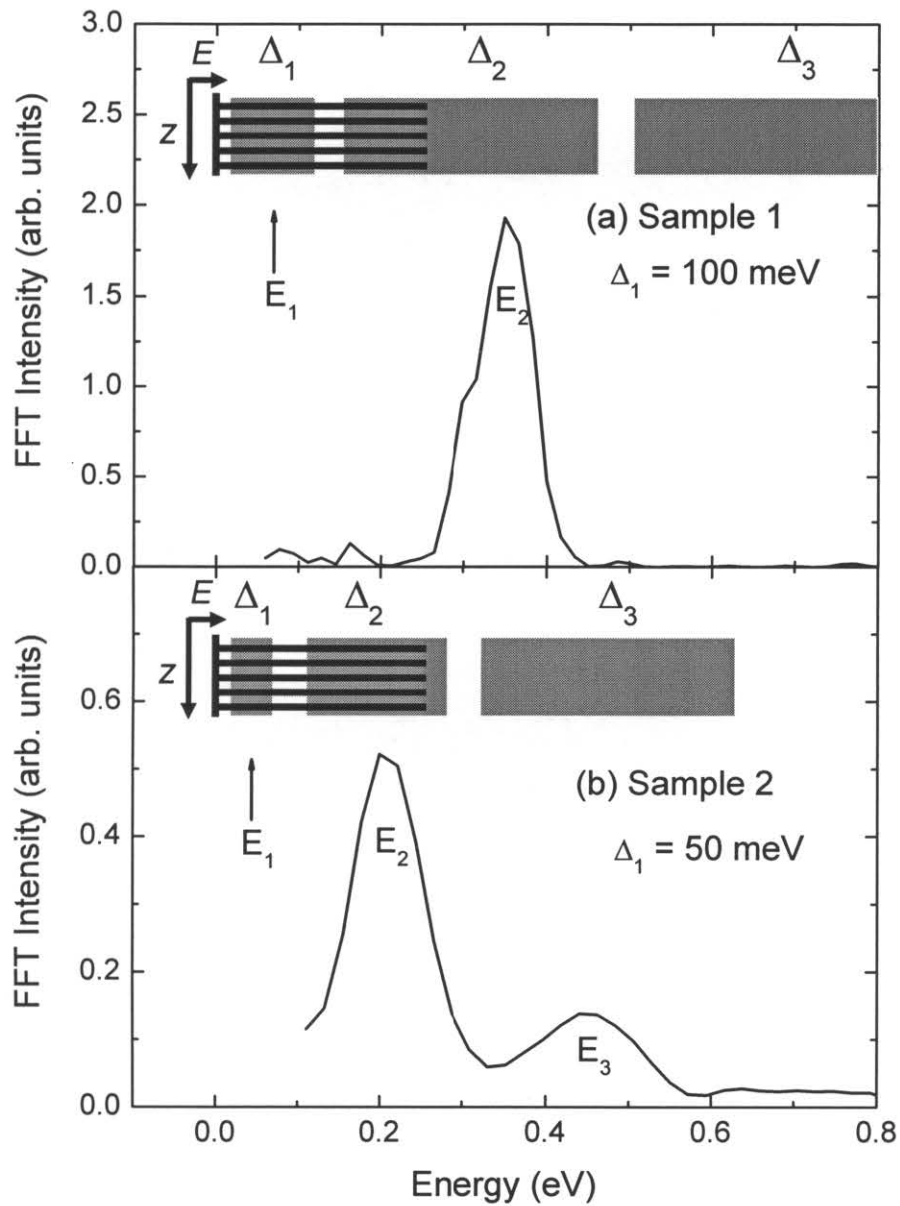
Fig. 3.16 Fast Fourier transform (FFT) spectra of the quasi-periodic part of the THz data for (a) sample 1 and (b) sample 2, respectively. The insets illustrate schematic conduction band profiles of the samples. The gray bars and gaps denote the positions of the minibands and minigaps, respectively, in each SL calculated by the Kronig-Penny model.

tunneling regime, quasi-periodic structures are observed in the bias field dependence of the emitted THz intensity. It is found that the quasi-periodic peak structure was identified to be due to the resonant Zener tunneling between the Wannier-Stark ladders associated with the ground and excited minibands. Resonant Zener tunneling into the first and second excited state was clearly resolved.

3.7 Summary of Chapter III

In this chapter, we have investigated the electron transport in biased GaAs/Al$_{0.3}$Ga$_{0.7}$As SL diodes. We have investigated a direct observation of THz emission due to BO in wide miniband GaAs/AlGaAs superlattice m-i-n diodes by time-resolved THz spectroscopy. Quasi-autocorrelation measurements were performed on the emitted THz electromagnetic wave by using a bolometer as a wideband detector. We have found that the THz radiation is strongly dependent on the miniband width. Furthermore we have found that the THz emission due to miniband transport is strongly dependent on the photon energy of the pump laser pulses. We would like to emphasize that the visibility of BOs is strongly dependent on the preparation of the initial wave packets by femtosecond laser pulses. The bias-field dependence of the emitted THz radiation intensity clearly showed a crossover from the miniband transport to the formation of WSL. In the WS regime, a few cycle BO were observed even at 300 K in a superlattice whose miniband width is greater than the LO phonon energy.

Furthermore, we have investigated terahertz (THz) emission due to dynamical electron transport in wide miniband GaAs/Al$_{0.3}$Ga$_{0.7}$As superlattices by time-domain THz emission spectroscopy. By noting that the time-domain THz spectroscopy inherently measures the step-response of the electron system to the bias electric field, the obtained THz spectra were compared with theoretically predicted high-frequency conductivity. Excellent agreement between theory and experiment strongly supports that the THz gain

due to Bloch oscillating electrons in wide-miniband superlattices persists at least up to 1.7 THz.

Finally, we have investigated the THz emission in a high-field range. With increasing bias fields, two distinct regimes are observed in the bias-field dependence of the emitted THz intensity. These two regimes are attributed to the intra-miniband transport and inter-miniband Zener tunneling regimes, respectively. In the inter-miniband Zener tunneling regime, quasi-periodic structures are observed in the bias field dependence of the emitted THz intensity. It is found that the quasi-periodic peak structure was identified to be due to the resonant Zener tunneling between the Wannier-Stark ladders associated with the ground and excited minibands. Resonant Zener tunneling into the first and second excited state was clearly resolved.

Bibliography

[1]   L. Esaki and R. Tsu, IBM J. Res. Dev. **14**, 61 (1970).

[2]   A. Sibille, J. F. Palmier, C. Minot, and F. Mollot, Appl. Phys. Lett. **54**, 165 (1989).

[3]   J. Feldmann, K. Leo, J.Shah, D. A. B. Miller, J. E. Cunningham, T. Meier, G. von Plessen, A. Schulze, P. Thomas, and S. Schmitt-Rink, Phys. Rev. B **46**, 7252 (1992).

[4]   K. Leo, P. Haring Bolivar, F. Brüggemann, R. Schwedler, and K. Köhler, Solid State Commun. **84**, 943 (1992).

[5]   C. Waschke, H. G. Roskos, R. Schwedler, K. Leo, H. Kurz, and K. Köhler, Phys. Rev. Lett. **70**, 3319 (1993).

[6]   T. Dekorsy, P. Leisching, K. Köhler, and H. Kurz, Phys. Rev. B **50**, 8106 (1994).

[7]   M. Helm, Semicond. Sci. Technol. **10**, 557 (1995).

[8]   K. Unterrainer, B. J. Keay, M. C. Wanke, S. J. Allen, D. Leonard, G. Medeiros-Ribeiro, U. Bhattacharya, and M. J. W. Rodwell, Phys. Rev. Lett. **76**, 2973 (1996).

[9]   E. Schomburg, T. Blomeier, K. Hofbeck, J. Grenzer, S. Brandl, I. Lingott, A. A. Ignatov, K. F. Renk, D. G. Pavel'ev, Yu. Koschurinov, B. Ya. Melzer, V. M. Ustinov, S. V. Ivanov, A. Zhukov, and P. S. Kop'ev, Phys. Rev. B **58**, 4035 (1998).

[10] F. Löser, Yu. A. Kosevich, K. Köhler, and K. Leo, Phys. Rev. B **61**, 13373 (2000).

[11] S. A. Ktitorov, G. S. Simin, and V. Ya. Sindalovskii, Sov. Phys. Solid State **13**, 1872 (1971).

[12] R. F. Kazarinov and R. A. Suris, Sov. Phys. Semicond. **6**, 120 (1972).

[13] X. L. Lei, N. J. M. Horing, and H. L. Cui, Phys. Rev. Lett. **66**, 3277 (1991).

[14] A. A. Ignatov, K. F. Renk, and E. P. Dodin, Phys. Rev. Lett. **70**, 1996 (1993).

[15] A. Wacker, G. Schwarz, F. Prengel, and E. Schöll, Phys. Rev. B **52**, 13788 (1995).

[16] X. -C. Zhang and D. Auston, J. Appl. Phys. **71**, 326 (1992).

[17] H. G. Roskos, M. C. Nuss, J. Shah, K. Leo, D. A. B. Miller, A. M. Fox, S. Schmitt-Rink, and K. Köhler, Phys. Rev. Lett. **68**, 2216 (1992).

[18] A. Leitenstorfer, S. Hunsche, J. Shah, M. C. Nuss, and W. H. Knox, Phys. Rev. Lett.

25, 5140 (1999).

[19] Y. Shimada, K. Hirakawa, M. Odnoblioudov, and K. A. Chao, Phys. Rev. Lett. **90**, 46806 (2003).

[20] R. Kersting, K. Unterrainer, G. Strasser, H. F. Kauffmann, and E. Gornik, Phys. Rev. Lett. **79**, 3038 (1997).

[21] P. Drude, Ann. Phys., Lpz **1**, 566 (1900).

[22] F. Bloch, Z. Phys. **52**, 555 (1928).

[23] C. Zener, Proc. R. Soc. A **145**, 523 (1934).

[24] G. H. Wannier, Phys. Rev. **76**, 1611 (1949).

[25] L. Esaki and L. L. Chang, Phys. Rev. Lett. **33**, 495 (1974).

[26] R. Dingle, A. C. Gossard, and W. Wiegmann, Phys. Rev. Lett. **34**, 1327 (1975).

[27] R. Tsu, L. L. Change, G. A. Sai-Halasz, and L. Esaki, Phys. Rev. Lett. **34**, 1509 (1975).

[28] K. Leo, J. Shah, E. O. Göbel, T. C. Damen, S. Schmitt-Rink, W. Schäfer, and K. Köhler, Phys. Rev. Lett. **66**, 201 (1991).

[29] G. C. Cho, T. Dekorsy, H. J. Bakker, H. Kurz, A. Kohl, and B. Optiz, Phys. Rev. B **54**, 4420 (1996).

[30] Y. Shimada, K. Hirakawa, and S.-W. Lee, Appl. Phys. Lett. **81**, 1642 (2002).

[31] R. Bratschitsch, R. Kersting, T. Müller, G. Strasser, K. Unterrainer, W. Fischler, and R. A. Höpfel, Physca B. **272**, 375 (1999).

[32] G. Brozak, M. Helm, F. DeRosa, C. H. Perry, M. Koza, R. Bhat, and S. J. Allen, Phys. Rev. Lett. **64**, 3163 (1990).

[33] T. Dekorsy, R. Ott, H. Kurz and K. Köhler 1995 Phys. Rev. B. **51**, 17275 (1995).

[34] E. E. Mendez, F. Agullo-Rueda, and M. Hong, Phys. Rev. Lett. **60**, 2426 (1988).

[35] P. Voisin, J. Bleuse, C. Bouche, S. Gaillard, C. Alibert, and A. Regreny, Phys. Rev. Lett. **61**, 1639 (1988).

[36] S. J. Allen, G. Brozak, E. Colas, F. DeRosa, P. England, J. Harbison, M. Helm, L. Florez, and Leadbeater, Semicond. Sci. Technol. **7**, B1 (1992).

116

[37] G. Bastard and R. Ferreira, C. R. Acad. Sci. Paris, t. 312, Serie II, 971 (1991).

[38] Strictly speaking, this statement is not perfectly correct; since, in the actual process, electrons are photoexcited in a biased band, a non-vertical transition process takes place and gives rise to a instantaneous polarization. However, this coherent polarization lasts only for the pulse duration and give a flat background to the THz spectra. Therefore, its effect on overall THz spectral shapes is negligible.

[39] B. Rosam, D. Meinhold, F. Löser, V. G. Lyssenko, S. Glutsch, F. Bechstedt, F. Rossi, K. Köhler, and K. Leo, Phys. Rev. Lett. **86**, 1307 (2001).